Physics Theses & Dissertations   Physics

Summer 8-2016

Forward Light Scattering in an Extended Sample of Cold Atoms

Stetson Roof
Old Dominion University

FORWARD LIGHT SCATTERING IN AN EXTENDED

SAMPLE OF COLD ATOMS

by

Stetson Roof
B.S. May 2010, Murray State University
M.S. May 2012, Old Dominion University

A Dissertation Submitted to the Faculty of
Old Dominion University in Partial Fulfillment of the
Requirements for the Degree of

DOCTOR OF PHILOSOPHY

PHYSICS

OLD DOMINION UNIVERSITY
August 2016

Approved by:

Mark D. Havey (Director)

Peter Bernath (Member)

Charles Hyde (Member)

Charles I. Sukenik (Member)

J. Wallace Van Orden (Member)

ABSTRACT

FORWARD LIGHT SCATTERING IN AN EXTENDED SAMPLE OF COLD ATOMS

Stetson Roof
Old Dominion University, 2016
Director: Dr. Mark D. Havey

We present results on the forward emitted light from a cold atomic sample of ^{87}Rb. Specifically, we study single-photon superradiance which is characterized by a rapid decay faster than the single atom lifetime with the light preferentially emitted in the forward direction. Additionally, we report measurements on its counterpart, the cooperative Lamb shift. The results are interpreted using microscopic light scattering theory as well as techniques from classical optics. The comparison of the two analytical techniques provides a new perspective on what is meant by cooperative and collective scattering effects in cold atomic physics.

ACKNOWLEDGEMENTS

The completion of my studies has been facilitated by a great number of people inside and outside of the physics department. I would like to thank my advisor, Dr. Mark D. Havey, for giving me the opportunity to work in his lab and the freedom in building the experiments. I thank Kasie Kemp, with whom I have worked with for the past five years, for her help with the experiments and I wish her the best in the future. I thank Dr. Sukenik for his endless support and advice. Whenever I had an issue, be it experimental or logistical, he was there to help and I am very grateful for that. I thank Jack Mills for his help in the lab when I needed it, advice on a range of topics, and invitations to Borjo for coffee. I would like to thank the departmental staff, Delicia Malin (Momma), Anette Guzman, and Lisa Okun, for all their support and help through non-physics related topics.

Outside of the physics department I have been fortunate to have an outstanding group of friends. The group has mostly been comprised of the ultimate frisbee crew in the Hampton roads area and we have shared some great memories over the last couple of years. It includes Dave, Kate, Maynard, John, Jay, Travis and many more (I would like to name them all, but there is just not enough space!). From regular pick-up games, to tournaments, to just hanging out, they made life fun and provided a great get away from the stress of work.

Lastly, but not least, I want to thank my family for supporting me and being there when I needed them. Experimental physics is not a field that relies solely on talent and creativity, but also perseverance. My parents instilled in me at a young age the value of hard work and much of my success can be attributed to them. I also want to extend a thank you, and I love you, to the rest of my family: Weston, Tannan, Nanny, Pappy, David, Ally, Ella, Teresa, and Molly. I am lucky to to have you all!

TABLE OF CONTENTS

LIST OF TABLES

LIST OF FIGURES

CHAPTER 1

INTRODUCTION

The study of many body systems has become a hot topic in recent years. One reason for this is that it opens up the door to vast new areas of study and the prospect of creating the next generation of technology. P. W. Anderson summed up the field appropriately with the statement, *More is Different* [3]. N bodies do not just interact with an external force individually but can add their contributions coherently in reaction and, most importantly, interact with one another. These many body interactions are what make the studies interesting and what give the deviation from a single-body response. While the field shows great promise, much work is left to do theoretically, and most importantly experimentally, to realize the potential of the physics. We seek to discuss and show how many body effects may be observed.

To give an example for the general reader as to what a many-body effect could mean we start with a case commonly encountered in classical electrostatics. Consider a region of space occupied by a dielectric medium and with an applied external electric E present within it. Due to the external field, a polarization will be built up in the medium given by

$$P = \epsilon_0 \chi E \tag{1}$$

where χ is the susceptibility which gives a measure of the over all electrical response of the medium and ϵ_0 is the permittivity of free space; we ignore the vector nature for simplicity. A single atom responds according to

$$d = \alpha E \tag{2}$$

where d is the dipole moment of the atom or molecule and α is the polarizability. The susceptibility can be related to the polarizability as the polarization is just the dipole moment per unit volume and so

$$\chi = \frac{\rho_a \alpha}{\epsilon_0} \tag{3}$$

where ρ_a is the sample density. This relation is true for low densities. However, as the density increases the atom/molecule begins to feel a significant contribution from the polarization within the sample such that the *local field* it is subject to is given by [4]

$$E_{loc} = E + \frac{P}{3\epsilon_0} \tag{4}$$

and now

$$d = \alpha E_{loc}. \tag{5}$$

These adjustments lead to a new relation between the polarizability and susceptibility,

$$\chi = \frac{\rho_a \alpha / \epsilon_0}{1 - \rho_a \alpha / 3\epsilon_0}. \tag{6}$$

This is sometimes called the *Clausius-Mossotti* or *Lorenz-Lorentz* relation when written in terms of the dielectric constant. When the material consists of two-level atoms it leads to a shift of the resonance line for the susceptibility. The resonance line refers to the frequency the atoms are most responsive to when radiated with an external light field of frequency ω. While the interpretation of this result has become a subject of heated debate of late [5, 6] the fact that more material causes a fundamental change of how that material responds to an external field is a significant realization.

The above example in fact belongs to an even larger area of study in the realm of light scattering in aggregate media. The field, generically called light scattering, encompasses many ideas such as multiple light scattering [7, 8, 9], random lasing [10], suppressed resonant fluorescence [11], density dependent dipole-dipole shifts [12, 13], coherent back scattering [14], Anderson light localization [15, 16, 17] and many more. The interest has grown partly out of the work to build viable quantum memories using light-matter interactions as the interface [18, 19, 20, 21]. The realization of the above studies are typically referred to as observing *collective* and *cooperative* effects. These terms are sometimes used rather broadly, interchangeably, and even ambiguously as will be the case at first in this text. We hope by the end to add some better defined meaning to their usage.

One rich, many-body, light scattering effect to study is that proposed by Dicke [22] but in the context of enhanced emission rates. In his work, Dicke considered how a group of atoms in close proximity to one another ($V \ll \lambda^3$ of a single atomic transition, where V is the volume of the sample) could interact through their own radiated fields to give cooperative enhancement of the collective emitted radiation. To formulate this, Dicke considered a collection of two-level systems (we will call them atoms) with all possible states arranged in a hierarchy of energy levels. These energy levels were taken to correspond to essentially the sum of atomic excitations present within the system. A diagram of the state structure is given in Fig. 1. Dicke introduced raising and lowering operators, analogous to angular momentum operators, such that the the states could be specified by the quantum number $m = \frac{1}{2}(N_+ - N_-)$ which is the difference in the number of atoms in excited state and in the ground state. Additionally, a second quantum number r, called the *cooperation number*,
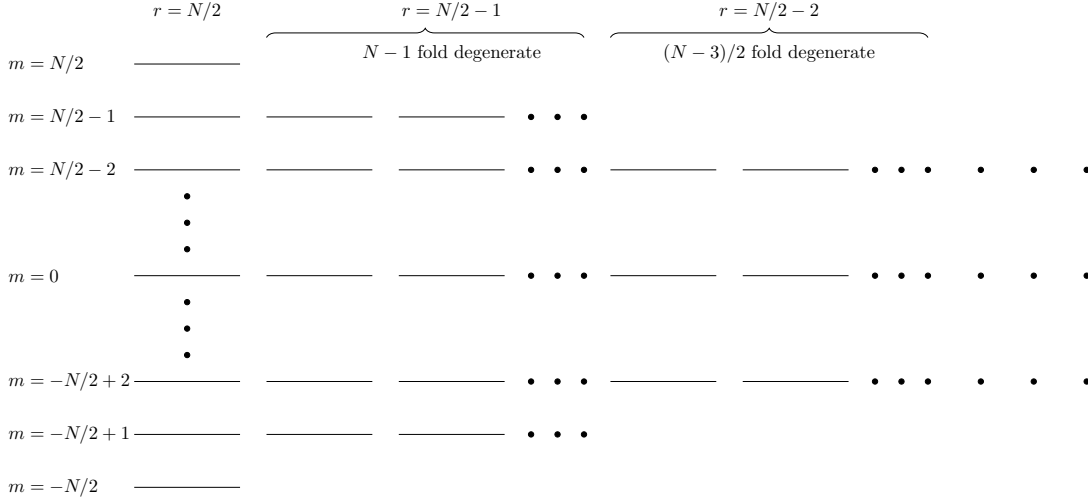
FIG. 1: The Dicke Manifold. The energy states of the N-atom system are arranged such that there is one unit of energy separation (one atomic excitation) between vertically ordered states. Due to the possible arrangement of atomic excitations, there are varying levels of degeneracies for particular m-states.

was introduced which corresponds to the "length" of the angular momentum vector with m being its projection along the $z-$axis. An analysis of the radiation rate from such a system gives

$$\Gamma_{coop.} = \Gamma(r + m)(r - m + 1), \tag{7}$$

Γ being the single atom decay rate. For $m = 0$, $\Gamma_{coop.}$ scales as N^2 and for $m = -N/2 + 1$ it scales as N. Samples that are large in extent $(V \gg \lambda^3)$ somewhat modify the anticipated rate but the scaling remains the same [23]. Experiments carried out early in the development of superradiance consisted of studies in warm vapor cells where systems were fully inverted $(m = N/2)$ and the cascade of fluorescence down the Dicke chain was observed [24, 25, 26]. What was particularly interesting about the inversion of the whole system was the eventual observation of the N^2 scaling for the emitted intensity and decay rate once the $m = 0$ level was reached; indicating there was a coherent process coming out of spontaneous emission.

While the $m = -N/2 + 1, r = N/2$ state only has the N dependent scaling, it too carries a unique significance separate from all others: it lies adjacent to states that *do not* decay as there are no energy levels that reside below them. The population essentially becomes trapped in these states and never re-emits the incident light. In reality, motional effects, collisions, and other dephasing mechanisms will cause the system to slowly decay.

Nevertheless, with a long decay time these states could be used as a type of light storage for quantum memories. Originally, the decay from the $r = -N/2 + 1$ states was labeled as *limited-superradiance* [27], but now has taken on the name *subradiance* [28, 29, 20]. Its study is a topic of much research and due to recent experimental work [28], the door has been opened to study subradiant states as a way of creating quantum memories.

The subradiant states are not directly accessible due to the way the system is excited. They must be reached indirectly through the superradiant states. One way which has been proposed [20] is to transfer the population from the first excited superradiant state. For the case of an extended sample, this state has been called a *timed-Dicke state* [30] (to be discussed more in depth later on) and its emission of light called *single-photon superradiance*. It has been studied fairly extensive theoretically [31, 32, 33, 34], but only until very recently has single photon superradiant decay been studied experimentally in a gas of atoms [35, 36, 37, 38]. Experimental investigation of single photon superradiance will be the main feature of this thesis.

Other than linking the outside world with subradiant states, the study of single photon superradiance importantly impacts many fields such as precision measurements and quantum sensors [39, 40]. This is in part due to a counterpart of single-photon superradiance known as the *cooperative Lamb shift*. The cooperative Lamb shift is analogous to the single atom Lamb shift in that it involves a shift of the atomic absorption line but results from the exchange of virtual photons between different atoms. The shift is highly dependent on the shape of the atomic sample and we will give an expression for it in the next chapter. With regards to precision measurements, optical lattice clocks [41] have become the most precise time standard device ever and they require very specific knowledge of sources of light shifts of the atomic energy levels. The shift and decay rate from superradiance would act as parasitic effect in this case and means must be taken to properly account for them.

Cold atoms provide a great environment to study both of these effects. The samples created are nearly free of Doppler broadening and can be arranged into shapes as desired for specific applications. Atom species can be chosen with nearly closed electric-dipole transitions that allow for close comparison with simple two-level system theory. Unlike many new research areas, the samples do not have to be degenerate gases and the single photon studies can be done with standard atom traps such as magneto-optical traps and far-off resonance traps. We choose these systems as our tool to study the superradiant effects.

The thesis is organized as follows: In Chapter 2, we will discuss from a microscopic point of view the theory of light scattering in a large atomic sample and explain how it leads

to the idea of single-photon superradiance. However, we will need, in addition, the use of analysis from the point of view of classical optics to also explain experimental results. The classical optics approach will be developed slowly throughout as it is needed in different places in different contexts. In Chapter 3, we will discuss the basics of atom trapping and the techniques we use to realize cold atom samples. Chapter 4 describes an experiment revealing the pitfalls of doing absorption measurements in small, dense atomic ensembles and how the index of refraction comes into play through beam propagation. In Chapter 5, the experimental setup used to measure the fast decays and frequency shifts of the atomic sample is described. In Chapter 6, we will present the time resolved and spectrally resolved measurements of the forward emitted light from the atomic system. We will also draw parallels with what one would expect from a classical system and discuss how this affects the interpretation of the experimental results and of microscopic light scattering theory in general.

CHAPTER 2

THEORY OF MICROSCOPIC LIGHT SCATTERING

In this chapter the general formalism is derived and presented for understanding cooperative effects in a large sample of atoms at zero temperature. This analysis is based on a quantized, scalar photon field interacting with an atomic system represented by point particles. While a realistic model would include effects due to polarization, atomic dipole orientation, and the multi-level atom structure, a scalar formalism serves well to show the qualitative response and corresponds closely to experimental observables due to the low density and nearly-closed transition probed in the experiments reported here.

2.1 THE INTERACTION HAMILTONIAN

The Hamiltonian describing the interaction between an electromagnetic field and an atom can we written in the Coulomb gauge as [42],

$$\hat{H} = \frac{1}{2m} \sum_{\alpha=1} \left[\hat{\mathbf{p}}_\alpha + e\hat{\mathbf{A}}(\mathbf{r}_\alpha) \right]^2 + \frac{1}{2} \int d\mathbf{r}\sigma(\mathbf{r})\phi(\mathbf{r}) + \frac{1}{2} \int d\mathbf{r} \left[\epsilon_0 \hat{\mathbf{E}}_{\mathbf{T}}(\mathbf{r})^2 + \mu_0^{-1}\hat{\mathbf{B}}(\mathbf{r})^2 \right], \quad (8)$$

which is also known as the *minimal-coupling* Hamiltonian. Here, m is the mass of an electron, p_α the momentum of the αth electron, $\mathbf{r}_\alpha$ the position of the αth electron, e the electron charge, $\hat{\mathbf{A}}$ the quantized vector potential, $\sigma(\mathbf{r})$ the charge density, $\phi(\mathbf{r})$ the scalar potential, ϵ_0 the electric permittivity of free space, $\hat{\mathbf{E}}_{\mathbf{T}}$ the quantized *transverse* electric field, μ_0 the magnetic permeability of free space, and $\hat{\mathbf{B}}$ the quantized magnetic field. Expressions for the electric field and vector potential are given by [42, 43],

$$\hat{\mathbf{E}}_{\mathbf{T}}(\mathbf{r}) = \sum_{\mathbf{k}\lambda} \mathbf{e}_{\mathbf{k}\lambda} \left(\frac{\hbar\omega_k}{2\epsilon_0 V_{\text{ph}}} \right)^{1/2} \left[\hat{a}_{\mathbf{k}\lambda}e^{i\mathbf{k}\cdot\mathbf{r}} + \hat{a}_{\mathbf{k}\lambda}^+ e^{-i\mathbf{k}\cdot\mathbf{r}} \right] \quad (9)$$

$$\hat{\mathbf{A}}(\mathbf{r}) = -i \sum_{\mathbf{k}\lambda} \mathbf{e}_{\mathbf{k}\lambda} \left(\frac{\hbar}{2\epsilon_0 \omega_k V_{\text{ph}}} \right)^{1/2} \left[\hat{a}_{\mathbf{k}\lambda}e^{i\mathbf{k}\cdot\mathbf{r}} - \hat{a}_{\mathbf{k}\lambda}^+ e^{-i\mathbf{k}\cdot\mathbf{r}} \right], \quad (10)$$

where $\mathbf{k}$ is the wave vector of a particular mode, λ one of two polarization directions about the wave vector, $\mathbf{e}_{\mathbf{k}\lambda}$ the polarization vector, $\hbar$ the reduced Planck's constant, ω_k the frequency of the kth mode, V_{ph} the vacuum quantization volume, and $\hat{a}_{\mathbf{k}\lambda}$ and $\hat{a}_{\mathbf{k}\lambda}^+$ the lowering and raising operators of the photon field, respectively. The first term of (8) represents the

kinetic energies of the electrons and the interaction of the quantized field with the atom. The second term represents the atomic electrostatic energy and the final term is the energy of the free electromagnetic field. By an appropriate unitary transformation [44, 45], (8) can be put into a more convenient form which serves to remove the vector potential from the Hamiltonian and leave dependence only on the field variable operators, $\hat{\mathbf{E}}_{\mathbf{T}}$ and $\hat{\mathbf{B}}$. Performing the transformation and keeping only the lowest order multipole term results in (where the relative size in magnitude is determined by powers of the fine structure constant)

$$\hat{H} = \hat{H}_a + \hat{H}_R + \hat{H}_{ED}. \tag{11}$$

Here H_a is the atomic Hamiltonian which contains the terms that involve the kinetic energies of the charges and all Coulomb interaction energies. The second term, H_R, is the free-field Hamiltonian given by,

$$H_R = \sum_{\mathbf{k}\lambda} \hbar\omega_k \hat{a}_{\mathbf{k}\lambda}^+ \hat{a}_{\mathbf{k}\lambda}. \tag{12}$$

The last term is the electric dipole interaction,

$$H_{\mathrm{ED}} = -\hat{\mathbf{d}} \cdot \hat{\mathbf{E}}, \tag{13}$$

where $\mathbf{d}$ is the electric dipole moment operator of the atom and the $\mathbf{T}$ subscript has been dropped from the electric field (9). [1] In consideration of a two-level atom, the Hamiltonian can be second quantized by assigning operators that take the atom from the ground state to the excited state and vice-versa. This can be formalized as

$$\hat{\sigma} = |g\rangle \langle e|$$
$$\hat{\sigma}^+ = |e\rangle \langle g|. \tag{14}$$

The operators $\hat{\sigma}$ and $\hat{\sigma}^+$ are known as the lowering and raising operators of the atom, respectively. The ground state is represented by the letter g and the excited state by the letter e. Their commutation relations are The atomic Hamiltonian can then be re-written as

$$\hat{H}_a = \hbar\omega_a \hat{\sigma}^+ \hat{\sigma}, \tag{15}$$

---

[1] Here the electric dipole interaction has been written as $\hat{\mathbf{d}} \cdot \hat{\mathbf{E}}$ for sake of understanding, but formally under the Power-Zineau-Woolley unitary transformation briefly mentioned, (9) no longer has the meaning of the electric field. Specifically, $\hat{\mathbf{E}}_{\mathbf{T}}' = \hat{U}_{PZW}^{-1} \hat{\mathbf{E}}_{\mathbf{T}} \hat{U}_{PZW} = \hat{\mathbf{E}}_{\mathbf{T}} - \frac{1}{\epsilon_0} \hat{\mathbf{P}}_{\mathbf{T}}$, which has the form $\epsilon_0 \mathbf{E} = \mathbf{D} - \mathbf{P}$ where $\mathbf{P}$ is the electric polarization of the sample and $\mathbf{D}$ is the *electric displacement*. Therefore, (9) should be interpreted as the electric displacement [46, 47, 48]. This is a subtle point, but is necessary when seeking to recover Maxwell's equations from a microscopic approach [49].

where ω_a is the transition frequency between the ground state and the excited state. The zero of energy is taken as the level of the ground state. The dipole-moment operator can also be redefined,

$$\hat{\mathbf{d}} = \mathbf{d}_{eg} \left(\hat{\sigma} + \hat{\sigma}^+ \right), \tag{16}$$

where $\mathbf{d}_{eg}$ is the dipole matrix element that is taken to be real. Inserting the above expression for $\hat{\mathbf{d}}$ into Eq. (13) results in

$$H_{\mathrm{ED}} = \sum_{\mathbf{k}\lambda} \hbar g_{\mathbf{k}\lambda} \left[\hat{a}_{\mathbf{k}\lambda} e^{i\mathbf{k}\cdot\mathbf{r}} + \hat{a}^+_{\mathbf{k}\lambda} e^{-i\mathbf{k}\cdot\mathbf{r}} \right] \left[\hat{\sigma} + \hat{\sigma}^+ \right], \tag{17}$$

where

$$g_{\mathbf{k}\lambda} = \left(\frac{\omega_k}{2\epsilon_0 \hbar V_{\mathrm{ph}}} \right)^{1/2} \mathbf{e}_{\mathbf{k}\lambda} \cdot \mathbf{d}_{eg} \tag{18}$$

describes the coupling between the atom and photon field. The variable $\mathbf{r}$ should be understood as the position of the center of mass of the atom.

In solving for the dynamics of the atom-radiation system it is convenient to analyze in the interaction picture where the time dependence is shared between both the wavefunction and the operators. The equation of motion for an operator in the interaction picture is,

$$i\hbar \frac{\mathrm{d}\hat{O}_I}{\mathrm{d}t} = \left[\hat{O}_I(t), \hat{H}_0 \right], \tag{19}$$

where the interaction operator is defined as,

$$\hat{O}_I(t) = e^{i\hat{H}_0 t/\hbar} \hat{O}_S e^{-i\hat{H}_0 t/\hbar}. \tag{20}$$

$\hat{O}_S$ stands for the operator representation in the Schrodinger picture where the operator carries no time dependence and $\hat{H}_0$ is the unperturbed Hamiltonian which is the sum of equations (12) and (15). Substitution of the atom and photon operators into (19) and (20) results in the following expressions,

$$\hat{\sigma}_I(t) = \hat{\sigma} e^{-i\omega_a t} \tag{21}$$

$$\hat{a}_{I\mathbf{k}\lambda}(t) = \hat{a}_{\mathbf{k}\lambda} e^{-i\omega_k t} \tag{22}$$

with $\hat{\sigma}^+_I(t)$ and $\hat{a}^+_{I\mathbf{k}\lambda}(t)$ given by the complex conjugates of (21) and (22), respectively. The advantage of configuring the system in the interaction picture can be clearly seen as the operators pick-up a simple harmonic time dependence with their respective frequencies. The electric dipole interaction term is now

$$\hat{H}_{\mathrm{ED}} = \hbar \sum_{\mathbf{k}\lambda} \left\{ g_{\mathbf{k}\lambda} \hat{\sigma}^+ \hat{a}_{\mathbf{k}\lambda} e^{i\mathbf{k}\cdot\mathbf{r} - \Delta_k t} + \mathrm{adj.} \right\}, \tag{23}$$

where $\Delta_k = \omega_k - \omega_a$, adj. is the adjoint or hermitian conjugate of the first term, and the counter-rotating terms $\Delta_k = \omega_k + \omega_a$ have been dropped. The high frequency terms are dropped in what is known as the *rotating-wave-approximation* as they are non-resonant and will contribute very little to the absorption and emission processes of the atom. From here on, (23) will serve to describe the interaction between the atom and the photon field. However, as it will be seen later on, the inclusion of the counter-rotating terms are necessary to describe correctly the interaction between individual atoms in a sample [50, 51, 52].

We will now move to implementation of (23) in solving for the state evolution of a two-level atom. This will require the use of a technique known as the *Wigner-Weisskopf approximation* [53] where the time dependence of the wavefunction will be explicitly solved for and an expression for the single-atom decay rate can be obtained.

2.2 WIGNER-WEISSKOPF THEORY FOR A SINGLE ATOM

The Wigner-Weisskopf theory is incorporated by making the ansatz,

$$|\Psi(t)\rangle = \beta(t)\,|e\rangle\,|0\rangle + \sum_{\mathbf{k}\lambda} \gamma_{\mathbf{k}\lambda}(t)\,|g\rangle\,|1_{\mathbf{k}\lambda}\rangle , \tag{24}$$

where it is assumed that the system can only exist in one of two states: the atom excited and no photons present or the atom in the ground state and one photon present. Here, β represents the excited state amplitude, e the excited state, $\gamma_{\mathbf{k}\lambda}$ the ground state amplitude of a particular photon mode, and g the ground state. Eq. (24) represents the wavefunction in the interaction picture, and because of such the dynamics of the state amplitudes can be solved from

$$i\hbar \frac{\partial}{\partial t}\,|\psi(t)\rangle = \hat{H}_{\mathrm{ED}}(t)\,|\psi(t)\rangle . \tag{25}$$

For the sake of simplicity we will take the *scalar* [51] form of (23) which involves considering only linearly polarized light and assuming the atom's dipole is aligned with the orientation of the electric field. This approximation will demonstrate the essential steps for evaluating the time dependence of the system.

Inserting (24) into (25) gives the coupled equations,

$$\dot{\beta} = -i \sum_{\mathbf{k}} g_{\mathbf{k}} e^{-i\Delta_k t + i\mathbf{k}\cdot\mathbf{r}} \gamma_{\mathbf{k}} \tag{26}$$

$$\dot{\gamma}_{\mathbf{k}} = -i g_{\mathbf{k}} e^{-i\mathbf{k}\cdot\mathbf{r} + i\Delta_k t} \beta. \tag{27}$$

The latter equation can be formally integrated to give,

$$\gamma_{\mathbf{k}}(t) = -i g_{\mathbf{k}} e^{-i\mathbf{k}\cdot\mathbf{r}} \int_0^t dt'\, e^{i\Delta_k t'} \beta(t') \tag{28}$$

Substituting (28) into (26),

$$\dot{\beta} = -\sum_{\mathbf{k}} g_{\mathbf{k}}^2 \int_0^t dt' e^{-i\Delta_{\mathbf{k}} t'} \beta(t - t') \tag{29}$$

where the time variable has been changed from $t' \rightarrow t - t'$. As the excited state evolution occurs on a time scale much slower than the natural frequency of the transition, the Markov approximation can be made $\beta(t - t') \approx \beta(t)$. This is also equivalent to saying that $\dot{\beta}$ only depends on the current value of β and that all memory of past events are forgotten [54]. Using this approximation and converting the sum over $\mathbf{k}$ to an integral $\sum_{\mathbf{k}} \rightarrow \frac{V_{ph}}{(2\pi)^3} \int d\mathbf{k}$,

$$\dot{\beta} = -\frac{V_{\text{ph}}}{2\pi^2} \beta \int_0^\infty dk k^2 g_{\mathbf{k}}^2 \left\{ \frac{1 - \cos(\Delta_k t)}{i\Delta_k} + \frac{\sin(\Delta_k t)}{\Delta_k} \right\}, \tag{30}$$

with the time integral being explicitly carried out. The time scales of concern, as stated before, are large compared to $\frac{1}{\Delta_k}$ so that $t \rightarrow \infty$. Evaluating the limit,

$$\lim_{t \to \infty} \left[\frac{1 - \cos(\Delta_k t)}{i\Delta_k} + \frac{\sin(\Delta_k t)}{\Delta_k} \right] = -i\text{PV}\left(\frac{1}{\Delta_k} \right) + \frac{\pi}{c}\delta(k - k_a), \tag{31}$$

where PV stands for the principal value. Physically, the first term corresponds to the Lamb shift for a single atom and requires more detail to be properly calculated [42]; here it will be neglected. Finally, upon evaluation of the integral over k we get,

$$\dot{\beta} = -\frac{\Gamma}{2}\beta \tag{32}$$

where $\Gamma = V_{\text{ph}} k_a^2 g_{k_a}^2 / \pi c$ is the single atom decay rate in the scalar approximation. It should be noted that this expression can be easily obtained by a simple application of Fermi's golden rule to the interaction potential (23), however it is insightful to see the Wigner-Weisskopf theory applied to a single atom before analyzing the multi-atom case. Now with the expression for Γ, we have an absolute scale factor when considering the enhanced decay rates and frequency shifts of extended atomic samples.

2.3 WIGNER-WEISSKOPF THEORY FOR MANY ATOMS

Extension to the many-atom case is accomplished by considering the excited state amplitude for each atom. Additionally, it is desirable to include the presence of a driving field as will be the case in the experiment. To this end, the wave function can be written down as [33, 34, 55, 56],

$$|\psi(t)\rangle = \alpha(t)|g\rangle|0\rangle + \sum_{j=1}^N \beta_j(t)|j\rangle + \sum_{\mathbf{k}} \gamma_{\mathbf{k}}|g\rangle|1_{\mathbf{k}}\rangle, \tag{33}$$

with the interaction Hamiltonian now given by,

$$\hat{H}_{\text{int}} = \hbar \sum_{j=1}^{N} \left\{ \frac{\Omega_0}{2} \hat{\sigma}_j e^{i\Delta_0 t - i\mathbf{k}_0 \cdot \mathbf{r}_j} + \text{adj.} \right\} + \hbar \sum_{\mathbf{k}} \sum_{j=1}^{N} \left\{ g_k \hat{\sigma}_j \hat{a}_{\mathbf{k}}^+ e^{i\Delta_k t - i\mathbf{k} \cdot \mathbf{r}_j} + \text{adj.} \right\}. \tag{34}$$

Here α is the amplitude of the state that allows for coupling between the laser field and the atoms, β_j is the excited state amplitude of the jth atom, N is the total number of atoms, Ω_0 is the Rabi frequency of the driving field defined by $\frac{d_{eg} E_0}{\hbar}$ where E_0 is the electric field amplitude of the laser, and $\Delta_0 = \omega_0 - \omega_a$ is the detuning of the laser from the atomic transition frequency. Without the presence of the last term in (33), (33) and (34) would describe the semi-classical evolution of the sample with $\alpha(t)$ assuming the role of the ground state amplitude. As in the experiment, we will only consider the effect of low light intensity incident on the atoms such that $\alpha(t) \sim 1$, meaning there is low probability of atomic excitation.

Applying Schrodinger's equation (25), as in the last section, results in the time evolution equations

$$\dot{\beta}_j = -i\frac{\Omega_0}{2} e^{-i\Delta_0 t + i\mathbf{k} \cdot \mathbf{r}_j} - i \sum_{\mathbf{k}} g_k e^{-i\Delta_k t + i\mathbf{k} \cdot \mathbf{r}_j} \gamma_{\mathbf{k}} \tag{35}$$

$$\dot{\gamma}_{\mathbf{k}} = -ig_k \sum_j e^{i\Delta_k t - i\mathbf{k} \cdot \mathbf{r}_j} \beta_j \tag{36}$$

Again, the equation for $\gamma_{\mathbf{k}}$ can be formally integrated and inserted into (35). The Markov approximation is invoked and the summation term over $\mathbf{k}$ turned into an integral such that it becomes,

$$-\frac{d_{eg}^2 c}{2\hbar\epsilon_0 (2\pi)^2} \sum_m \beta_m(t) \int_0^t dt' \int_{-\infty}^{\infty} dk k^3 e^{-i\Delta_k t'} \int_{-1}^{1} d(\cos\theta) e^{ikr_{jm}}. \tag{37}$$

Here the lower limit on k has been extended to $-\infty$ as this artificially restores the counter-rotating terms that were neglected in (23) [42, 33]. The significance of this will be described shortly. Carrying out the $\cos\theta$ integral,

$$\frac{-id_{eg}^2 c}{2\hbar\epsilon_0 (2\pi^2)} \frac{1}{r_{jm}} \int_0^{\infty} dt' e^{ick_a t'} \int_{-\infty}^{\infty} dk k^2 \left[e^{-ik(ct' - r_{jm})} - e^{-ik(ct + r_{jm})} \right]. \tag{38}$$

Considering the integral over k, it can be written as

$$\int_{-\infty}^{\infty} dk k^2 \left[e^{-ik(ct' - r_{jm})} - e^{-ik(ct + r_{jm})} \right] = -\frac{2\pi}{c^3} \frac{\partial^2}{\partial t'^2} \left[\delta(t' - r_{jm}/c) - \delta(t' + r_{jm}/c) \right], \tag{39}$$

where the delta function is defined by,

$$\delta(t' \pm r_{jm}/c) = \frac{1}{2\pi} \int_{-\infty}^{\infty} d\omega_k e^{-i\omega_k (t' \pm r_{jm}/c)}. \tag{40}$$

The second delta function corresponds to times outside the limits of integration and will be discarded. This amounts to keeping only the retarded time contribution. The time integral portion is now,

$$\int_0^t dt' e^{ickat'} \frac{\partial^2}{\partial t'^2} \delta(t' - r_{jm}/c) = -c^2 k_a^2 e^{ik_a r_{jm}},$$ (41)

after integrating by parts twice. Expression (38) becomes,

$$\frac{\Gamma}{2} \frac{e^{ik_a r_{jm}}}{ik_a r_{jm}},$$ (42)

where $\Gamma = \frac{d_{eg}^2 k_a^3}{2\pi\hbar\epsilon_0}$ is an equivalent form of the decay rate achieved in the previous section. Substitution of (42) back into the rate equation (35) and making the slowly-varying-envelope approximation for the excited state amplitudes $\beta_j \simeq \beta_j e^{-i\Delta_0 t}$ gives

$$\dot{\beta}_j = -i\frac{\Omega_0}{2} e^{i\mathbf{k}_0 \cdot \mathbf{r}_j} + i\Delta_0 \beta_j - \frac{\Gamma}{2} \sum_m \beta_m \frac{e^{ik_a r_{jm}}}{ik_a r_{jm}}.$$ (43)

The $m = j$ terms in the summation will have a real and imaginary part which correspond to the single atom decay rate and Lamb shift, respectively. Pulling out both terms, but absorbing the Lamb shift into the natural frequency ω_a, produces,[2]

$$\dot{\beta}_j = -i\frac{\Omega_0}{2} e^{i\mathbf{k}_0 \cdot \mathbf{r}_j} + \left(i\Delta_0 - \frac{\Gamma}{2}\right)\beta_j - \frac{\Gamma}{2} \sum_{m \neq j} \beta_m \frac{e^{ik_a r_{jm}}}{ik_a r_{jm}}.$$ (44)

Finally, we obtain a set of equations that model the time-evolution of a system of interacting atoms in what is called the *coupled-dipole model* [33, 34, 55, 56]. Looking at the form of (44) it can be seen that there are two terms driving the dynamics. The first is the external laser field Ω_0 which not only excites the atoms, but imprints upon each a distinctive phase $\mathbf{k}_0 \cdot \mathbf{r}_j$ which is responsible for the strongly forward emitted light to be studied. The second term in the rate equation represents the scattered light from surrounding atoms onto atom j. This scattered light is comprised of real, radiated photons which come from the real part of the summation [51] and *virtual* photons from the imaginary portion [50, 51]. The ability to incorporate both comes from the fact that the counter-rotating terms were placed back in at (37). Had only the resonant terms been kept, the summation in (44) would only contain a sin kernel and it would not be possible to explain cooperative frequency shifts for extended samples [50].

---

[2]When the vector nature of the light is taken into effect the interaction term in the summation can replaced by the more general form [55, 38], $G_{\mu\nu}(\mathbf{r}_{jm}) = \frac{e^{ikr_{jm}}}{kr_{jm}} \left[(\delta_{\mu\nu} - \hat{r}_\mu\hat{r}_\nu) + \left(\frac{i}{kr_{jm}} - \frac{1}{(kr_{jm})^2}\right)(\delta_{\mu\nu} - 3\hat{r}_\mu\hat{r}_\nu)\right]\beta_m^\nu$, where $\hat{r}$ is the unit displacement vector between atoms j and m. This is also representive of the potential for interacting radiating dipoles encountered in classical electrodynamics [4].

In the experiment the detected signal will be scattered light from the atoms and therefore it is necessary to know both the time dependence of the excited state amplitude and the resulting emitted intensity. The total average scattered intensity at time t is [47],

$$\langle I(\mathbf{r}_s, t)\rangle = c\epsilon_0 \left\langle \hat{E}^-(\mathbf{r}_s, t)\hat{E}^+(\mathbf{r}_s, t)\right\rangle, \tag{45}$$

where $\mathbf{r}_s$ is the observation point for the scattered intensity and $\hat{E}_s^+$ is the positive frequency component of the electric field from (9),

$$\hat{E}_s^+(\mathbf{r}_s, t) = \sum_{\mathbf{k}} \left(\frac{\hbar\omega_k}{2\epsilon_0 V_{\text{ph}}}\right)^{1/2} \hat{a}_{\mathbf{k}} e^{-i\omega_k t + i\mathbf{k}\cdot\mathbf{r}_s} \tag{46}$$

using the representation in the interaction picture. The expectation value can then be taken with respect to the wavefunction in the interaction picture (33),

$$\left\langle \hat{E}^-(\mathbf{r}_s, t)\hat{E}^+(\mathbf{r}_s, t)\right\rangle = \left|\sum_{\mathbf{k}} \left(\frac{\hbar\omega_k}{2\epsilon_0 V_{\text{ph}}}\right)^{1/2} e^{-i\omega_k t + i\mathbf{k}\cdot\mathbf{r}_s}\gamma_{\mathbf{k}}(t)\right|^2. \tag{47}$$

The expression for $\gamma_{\mathbf{k}}(t)$ was obtained previously from (36) so that (46) becomes,

$$\left|\sum_j \sum_{\mathbf{k}} \left(\frac{\omega_k d_{eg}}{2\epsilon_0 V_{\text{ph}}}\right) e^{-i\omega_k t - i\mathbf{k}\cdot\mathbf{r}_{sj}} \int_0^t dt' e^{i\Delta_k t'}\beta_j(t')\right|^2, \tag{48}$$

where $\mathbf{r}_{sj} = \mathbf{r}_s - \mathbf{r}_j$. Just as in the former analysis for the single atom Winger-Weisskopf theory and for the coupled-dipole equation, the time variable will be changed to $t - t'$ and the Markov approximation used. Applying this and again extending the lower limit of integration of k to $-\infty$,[3]

$$\left\langle \hat{E}^-(\mathbf{r}_s, t)\hat{E}^+(\mathbf{r}_s, t)\right\rangle = \left|\frac{d_{eg}}{4\pi\epsilon c^2} \sum_j \frac{\beta_j(t)}{r_{sj}} e^{-i\omega_a t} \int_0^t dt' e^{i\omega_a t'} \frac{\partial^2}{\partial t'^2}\delta(t' - r_{sj}/c)\right|^2 \tag{49}$$

$$= \left|\frac{k_a^2 d_{eg}}{4\pi\epsilon_0} \sum_j \frac{\beta_j(t)}{r_{sj}} e^{-i\omega_a(t - r_{sj}/c)}\right|^2, \tag{50}$$

---

[3]Here it can be seen that the exponential term contains the retarded time $t - r_{sj}/c$ indicating the casuality of the process. In reality, the β_j term time dependence should also have this form [33], but the Markov approximation was made. One could have simply retained β_j within the time integral and obtained the correct time dependence, but the approximation was made for consistency with previous calculations. Either way, due to the time scale by which the atomic state evolves, $\beta_j(t - r_{sj}) \simeq \beta_j(t)$ as t is taken much larger than the transit time for the light signal from the sample to the observation point $\mathbf{r}_s$. For extremely large samples the Markov approximation can not be applied as previous events begin to contribute to the current state of the system and an effective cavity regime is entered [31].

The sample dimensions are taken to be much smaller than the point of observation such that, $r_{sj} \simeq r_s - \frac{\mathbf{r}_s \cdot \mathbf{r}_j}{r}$. With $k_s = k_a \frac{\mathbf{r}_s}{r_s}$, the intensity (45) takes the form,

$$\langle I(\mathbf{r}_s, t) \rangle = \frac{\hbar \omega_a \Gamma}{8\pi r_s^2} \left| \sum_j \beta_j(t) e^{-i\mathbf{k}_s \cdot \mathbf{r}_j} \right|^2, \tag{51}$$

and the denominator has just been taken as $r_{sj} \simeq r_s$. The intensity falls off as $1/r_s^2$ as expected for emitted light in the radiation zone [57] and there is a dependence on the relative phase between the atoms.

We will now be concerned with solving (44) numerically and looking at the emergent collective properties from the scattered fields. This will serve as a good starting point for determining where and how to look for the cooperative effects experimentally.

2.4 NUMERICAL SOLUTION OF THE COUPLED-DIPOLE EQUATION

To put (44) into dimensionless form, we will take the natural time scale as $1/\Gamma$ and the natural length scale as $1/k_0$,

$$\dot{\beta}_j = -\frac{i}{2} \Omega_0 e^{i\hat{\mathbf{k}}_0 \cdot \bar{\mathbf{r}}_j} + \left(i\Delta - \frac{1}{2} \right) \beta_j + \frac{i}{2} \sum_{m \neq j} \frac{e^{i\bar{r}_{jm}}}{\bar{r}_{jm}} \tag{52}$$

where $\hat{\mathbf{k}}_0$ is the unit vector of the laser beam wave number, $\Omega_0 \equiv \Omega_0/\Gamma$, $\Delta \equiv \Delta/\Gamma$, $\bar{r}_j = k_0 r_j$, and the approximation $k_a/k_0 \simeq 1$ has been made. Then (52) can be cast into a matrix form,

$$\dot{\boldsymbol{\beta}} = \boldsymbol{\Omega} + \underline{M}\boldsymbol{\beta}, \tag{53}$$

with $(\boldsymbol{\Omega})_j = -\frac{i}{2}\Omega_0 e^{i\hat{\mathbf{k}}_0 \cdot \bar{\mathbf{r}}_j}$ and $(\underline{M})_{jm} = \left(i\Delta - \frac{1}{2} \right) \delta_{jm} + \frac{i}{2} \frac{e^{i\bar{r}_{jm}}}{\bar{r}_{jm}}$. In reality, $\Omega_0 = \Omega_0(t)$ and represents the time-dependent pulse shape incident on the atoms. For simplicity and speed of the calculation it will be taken as a square pulse. In experiment this is not exactly the case as there will be some finite rise and fall time of the pulse generated in the electronics used to switch on and off the laser beam. However, we find the square pulse matches well with observed signals in experiment.

Equation (53) can be solved exactly for a square pulse by finding the associated eigenvectors for $\underline{M}$ and making the solutions match at the boundary for the laser beam on and the laser beam off. However, this becomes computationally expensive when diaganolizing $\underline{M}$ for many atoms. A more straightforward method is to use the Runge-Kutta method to solve for $\boldsymbol{\beta}$ in discrete time-steps. Particularly for an equation of the form $y' = Ay + b(t)$

the solution can be written down using 4th-order Runge-Kutta as [58],

$$y_{i+1} = y_i + (k_1 + 2k_2 + 2k_3 + k_4)/6 \tag{54}$$

where

$$k_1 = h\left[Ay_i + b(t_i)\right] \qquad\qquad k_2 = h\left[A(y_i + k_1/2) + b\left(t_i + \frac{h}{2}\right)\right]$$

$$k_3 = h\left[A(y_i + k_2/2) + b\left(t_i + \frac{h}{2}\right)\right] \qquad k_4 = h\left[A(y_i + k_3) + b(t_i + h)\right] \tag{55}$$

The term A takes the role of $\underline{M}$ and b the role of $\mathbf{\Omega}$. The step size is denoted by h and the error in this integration method is to fifth order in its value. Simulations can be performed quite fast using (54) with limitations in the maximum number of atoms stemming from computer memory allocation.

To replicate as closely as possible what is probed in experiment, atoms are distributed randomly within an ellipsoidal Gaussian shape given by

$$\rho(r, z) = \rho_0 e^{-r^2/2r_0^2 - z^2/2z_0^2} \tag{56}$$

where r_0 and z_0 are the short and long axis radii, respectively (see Fig. 2). All atoms are given the initial condition $\beta_j(0) = 0$ and the system is averaged over multiple configurations to achieve good statistics. Fig. 3 shows the angular distribution of scattered light for an increasing number of atoms for 12 sample realizations. The laser beam is incident along the z-direction of the sample. For a single atom the scattered light is isotropic but quickly obtains directional emission with an increasing number of atoms.

In the time domain, the cooperative decay rate also builds up a characteristic dependence on the number of atoms. To examine this, the sample is excited by a temporally short probe pulse $(T = 2/\Gamma)$ and the forward emitted light is observed as function of time. For the forward direction (Fig. 4(a)), the decay is single exponential, scales linearly with the number of atoms, and is proportional through a factor that depends on the particular shape of the sample. This will be discussed in the next section. The single exponential behavior of the scattered light is not a uniform feature as shown in Fig. 4(b). Superradiant emission is strongly coupled to the forward direction, but off axis its intensity is much weaker and it is possible to see contribution from other modes excited in the sample; particularly interesting are subradiant modes which have much longer decays as compared to the single atom case. This effect is more profound for longer probing cycles where state mixing transports larger portions of the population into subradiant modes [29, 28].
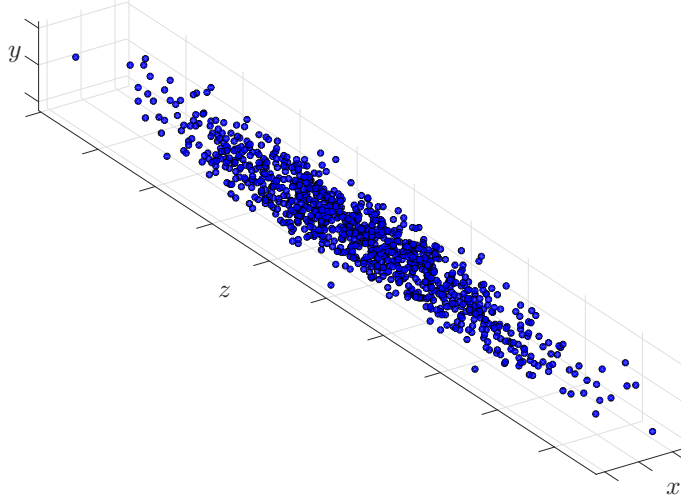
FIG. 2: A single realization of the simulation for 1000 atoms with indications for the long axis z and the short axises x and y (in units of $\lambda/2\pi$). The atoms are placed randomly within a normal distribution of the form (56) with $r_0 = 8/k_0$ and $z_0 = 80/k_0$.

The spectral response is also of interest as the atoms can show a collective shift [13, 59, 51] in addition to a collective decay rate. To analyze this, the atoms are probed in steady state and the scattered light is detected as a function of detuning. Similar to the decay rate, the width of the spectrum has a dependence on the number of atoms and shows a slight shift for the largest number (Figs. 6 and 7). Using the assumption that the atomic response will be Lorentzian as in the single atom case, the scattered light is fit to

$$I(\delta) = \frac{A}{1 + 4 \left(\Delta - \Delta_N \right)^2 / \Gamma_N^2},\tag{57}$$

where Γ_N is the collective decay rate of the sample and Δ_N is the collective shift. With regards to the specific kernel used in (44), $\sin(kr)$ does not produce a shift as the $\exp(ikr)$ kernel does. Retaining the full $\exp(ikr)$ term is necessary for describing the correct sample response [27] and for an accurate comparison with experimental data.

The coupled-dipole model is very successful in simulating the many-body dipole-dipole interactions and gives excellent agreement with experiment. However, it would be advantageous to be able to predict the emergent collective properties *a priori* to the simulation or to the experiment with some physical significance given to the sample's decay rate and spectral shift. In fact there is such a way and it involves preparing the sample in what is known as a *timed-Dicke state* [30] where a single photon is absorbed within the sample but it is not known which atom absorbed it. This will be the focus of the next section and will
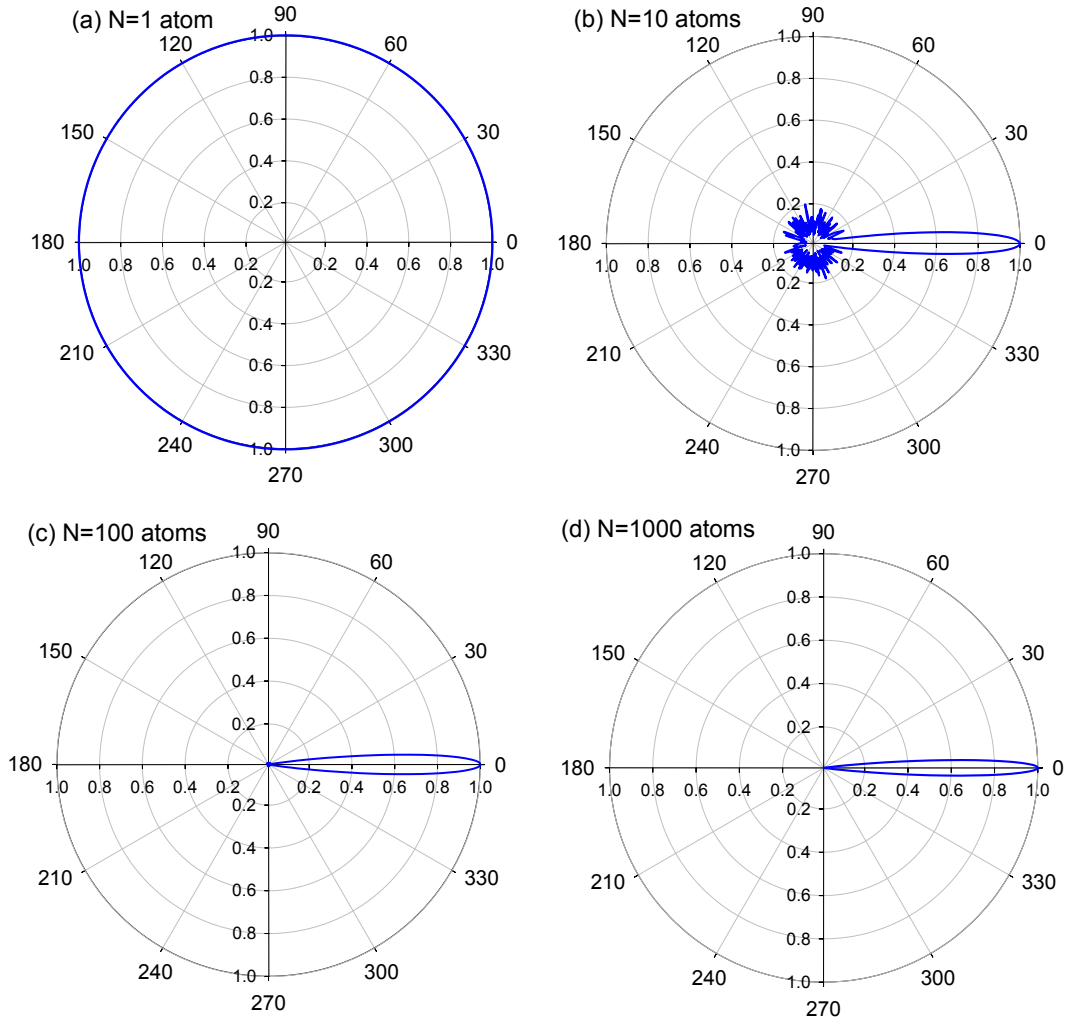
FIG. 3: Simulation of the coupled-dipole equation (44) for N=1, 10, 100, and 1000 atoms on a normalized scale for 12 sample realizations. The sample has the same dimensions as Fig. 2 and is probed with a laser pulse in the z-direction on resonance. Each sample is probed with a laser beam of equal intensity. The angle in the caption refers to the zenith angle θ.
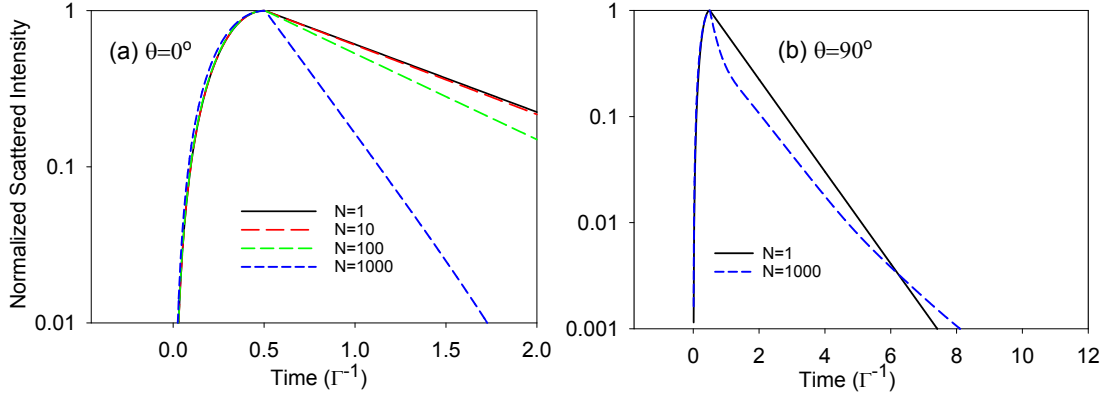
FIG. 4: Time dependence for different numbers of atoms for the same sample dimensions as in Fig. 3 with the laser detuning value $\Delta = -6\Gamma$. (a) The light is collected in the forward direction and the system shows a single exponential behavior. (b) The light is collected at $90°$ with respect to the direction of the laser beam and averaged over 48 sample configurations. There is no longer a simple exponential behavior. This is due to more contribution from subradiant modes.
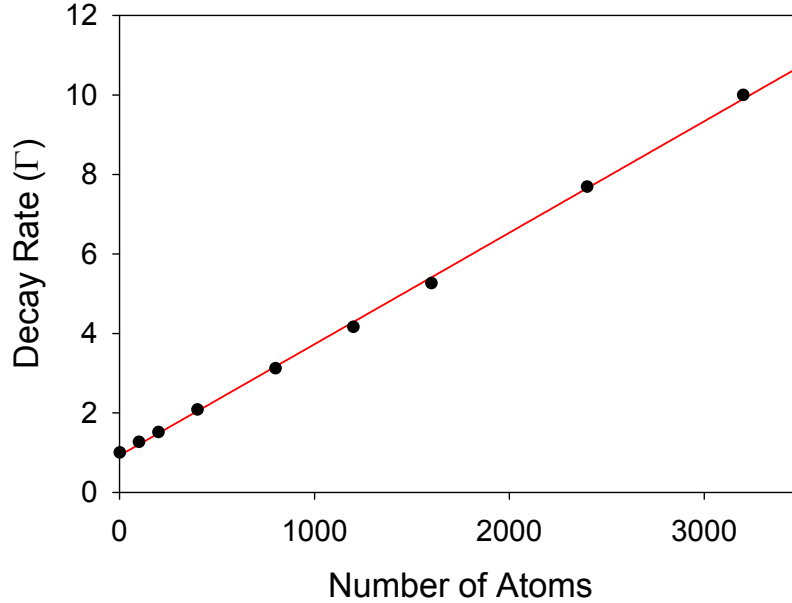
FIG. 5: Decay rate values extracted from the sample-emitted light in units of the single atom decay rate Γ. After the laser beam is shut off the decay of the scattered light is fit to a single exponential and it is found that the decay rate increases linearly with the number of atoms converging to the single atom limit at low N. The red line is a linear fit to the data.
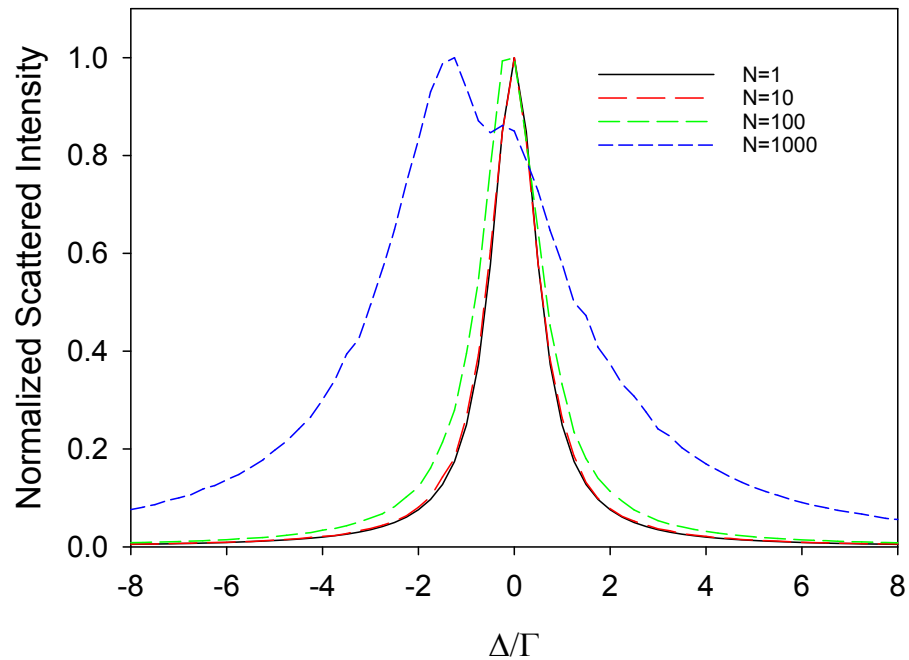
FIG. 6: Spectral response as a function of the number of atoms. The frequency of the laser beam is represented in units of the single atom decay rate. As the number increases the width of the scattered light increases and also shows a shift in the peak response. Eventually, the shift develops a distortion that is linked to propagation effects within the sample.
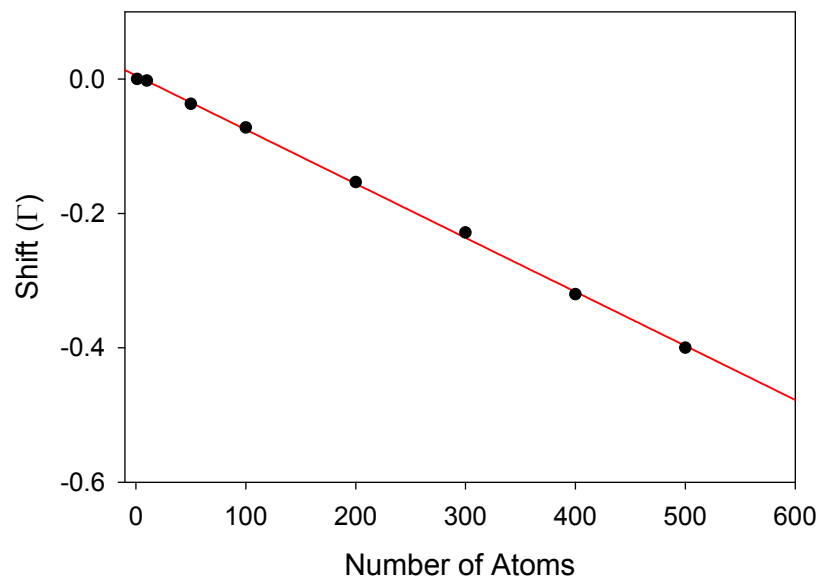
FIG. 7: The shift extracted from fitting the spectral data to a Lorentzian spectral line shape (57). The red line is a linear fit to the data.

add more meaning to the idea of collective system properties.

2.5 SINGLE-PHOTON SUPERRADIANCE

If we assume there is a way to excite the sample of atoms such that, on average, each one has equal probability to absorb a photon, but it is not known which, we could construct a state of the system given by

$$|+\rangle_{\mathbf{k}_0} = \frac{1}{\sqrt{N}} \sum_j e^{i\mathbf{k}_0 \cdot \mathbf{r}_j} |j\rangle \tag{58}$$

where each atom picks up a phase factor $e^{i\mathbf{k}_0 \cdot \mathbf{r}_j}$ determined by the laser beam direction of propagation and the atom's location in space. This state is commonly referred to as a timed-Dicke state [30] due to the order in which the atoms are excited as the phase in (58) corresponds to a time t_j. As opposed to solving for the time evolution of each indivdual atom we could seek to find the time dependence of this state and modify the previous wavefunction (33) to

$$|\psi(t)\rangle = \alpha(t) |g\rangle |0\rangle + \beta_+(t) |+\rangle_{\mathbf{k}_0} + \sum_{\mathbf{k}} \gamma_{\mathbf{k}}(t) |g\rangle |1_{\mathbf{k}}\rangle, \tag{59}$$

where $\beta_+(t)$ is the state amplitude of (58) and allows us to consider the time evolution of the entire sample. The interaction Hamiltonian is still given (34) and applying the same analysis as in the previous sections, the state evolution equation is found to be,

$$\dot{\beta}_+ = -\frac{i}{2}\sqrt{N}\Omega_0 + i\left(\Delta_0 - \Delta_N\right)\beta_+ - \frac{1}{2}\Gamma_N\beta_+, \tag{60}$$

with

$$\Delta_N = \frac{\Gamma}{2N}\mathrm{Im}\left[\sum_{j,m\neq j} \frac{e^{ik_a r_{jm}}}{ik_a r_{jm}} e^{-i\mathbf{k}_0 \cdot \mathbf{r}_{jm}}\right] \tag{61}$$

$$\Gamma_N = \frac{\Gamma}{N}\mathrm{Re}\left[\sum_{j,m} \frac{e^{ik_a r_{jm}}}{ik_a r_{jm}} e^{-i\mathbf{k}_0 \cdot \mathbf{r}_{jm}}\right]. \tag{62}$$

The terms corresponding to $j = m$ in (61) have been removed as before and renormalized into ω_a. The interpretation of (60) is as follows: the state of the system is governed by the dynamics of the β_+ amplitude by which interactions between the atoms gives rise to a real, enhanced decay rate Γ_N produced by real photon scattering from one atom to the next and a virtual (imaginary) shift Δ_N of the resonance line by virtual photon exchange between atom pairs [51]. Taking $N \to \infty$ such that we can assume the continuous limit, (62) takes the form of $\Gamma_N = \Gamma + \alpha(N-1)\Gamma$, where the factor α is given by,

$$\alpha = \frac{\sqrt{\pi}}{4\sigma\sqrt{\eta^2 - 1}} \exp\left[\frac{\sigma^2}{\eta^2 - 1}\right] \left\{\mathrm{erf}\left[\frac{\sigma}{\sqrt{\eta^2 - 1}}\left(2\eta^2 - 1\right)\right] - \mathrm{erf}\left[\frac{\sigma}{\sqrt{\eta^2 - 1}}\right]\right\}. \tag{63}$$

This result is derived in appendix A. Here $\sigma = k_0 r_0$ and $\eta = z_0/r_0$ which is commonly referred to as the aspect ratio of the sample [55, 60]. Putting (61) into a closed form expression is more difficult and is only possible in extreme sample limits [61]. For comparison between simulation and experiment we will calculate it explicitly using the atom positions as randomly distributed within a Gaussian shape given by (56). Because the construction of the timed-Dicke state only assumes one photon within the sample at a time, the process is also referred to as *single-photon superradiance*.

Below, the emergent collective properties that were observed in simulation through the coupled-dipole equation are compared with the quantities obtained in (61) and (62). The decay rates are in good agreement for the lower number of atoms and some discrepancy begins to occur for the larger number. The effect is more associated with the optical depth of the sample than it is the absolute number, and so the sample geometry chosen also plays a role. The origin of the deviation stems from the fact that the sample is not quite represented by a timed-Dicke state. This is because it is very optically thick and so picks up a more complicated decay structure compared to the anticipated single-exponential behavior from (62) [32]. The shift predicted from (61) is on the same order as the simulation but the differences are more noticeable. One reason for this could be that in the simulation the scattered fields are subject to propagation effects which come from the effective index of refraction of the medium. This causes, as will shown in Chapter 4, red-detuned light to be pulled more into the sample resulting in a greater chance of further scattering.

An important feature must be mentioned in regards to the accessible states in the timed-Dicke manifold. By virtue of the symmetry of the wavefunction (58), the problem of the time evolution of β_+ is only a superradiant one; meaning there is no way to determine the subradiant response of the system which corresponds to anti-symmetric states. This is where the analysis falls short and why the coupled-dipole equation (44) must still be counted on in helping to understand experimental results. The timed-Dicke state can be thought of as an ideal case in which there is no mode-coupling between superradiant and subradiant states such that what is observed is always superradiant. In actuality, a timed-Dicke state can be initially excited but due to the presence of virtual photons the superradiant state is degraded and some of the population is transfered into subradiant modes [62, 63]. However, the current problem of interest is the forward emitted light which is almost entirely dominated by superradiance and so the analysis in this section still provides a very good platform for understanding and discussing the results.
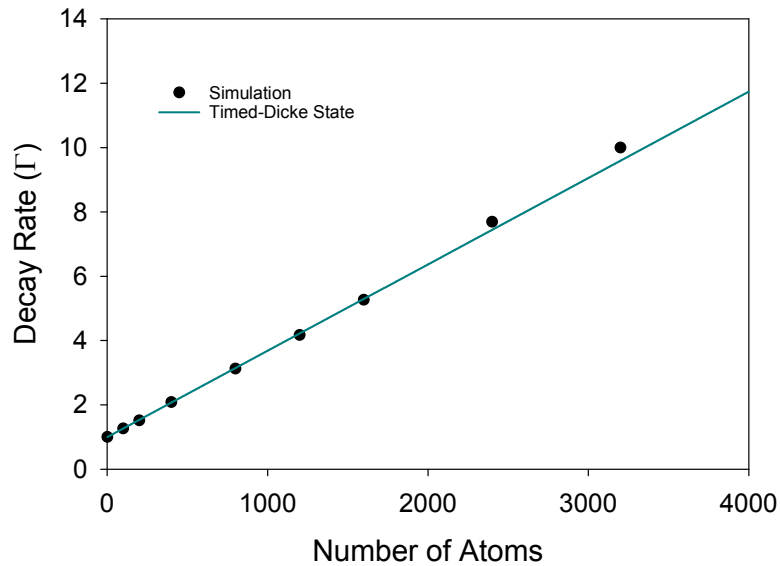
FIG. 8: Comparison of the timed-Dicke state and simulation of the coupled-dipole equation. The match is good for lower number of atoms, but as the number increases there is a slight deviation. This deviation is not explicitly related to the number of atoms but more to the optical thickness of the sample.
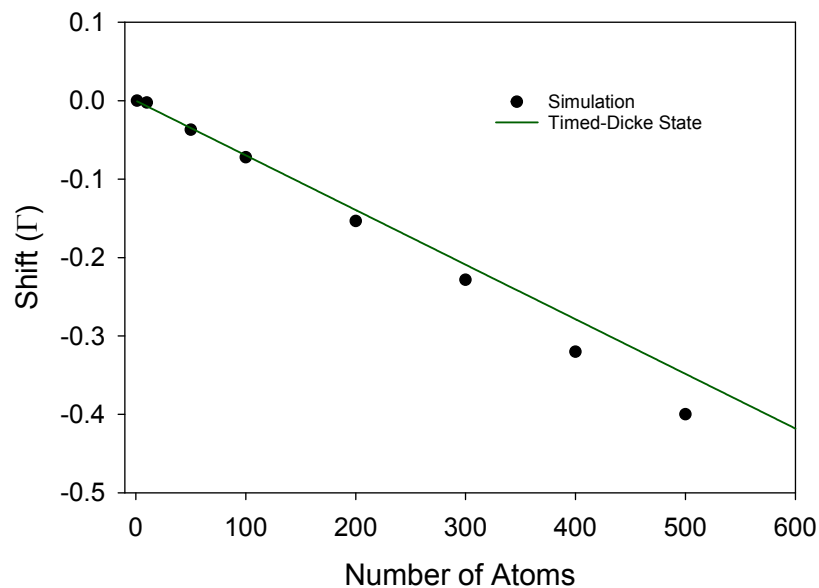
FIG. 9: Comparison of the shift of resonance for the timed-Dicke state approach and the simulation. Both show a linear dependence and are on the same order. Slight differences are potentially from propagation effects of the emitted fields in simulation which cannot be accounted for in the timed-Dicke state.

CHAPTER 3

TRAPPING ATOMS

The analysis of the previous chapter introduced some intriguing ideas regarding the many-body physics of interacting atoms. In order to observe these effects experimentally, one must be able to collect a large group of atoms and localize them in space. This task is not trivial and requires extensive knowledge of atom-light interactions and the use of technical laboratory equipment. Fortunately, researchers in cold atom physics have worked hard to perfect trapping techniques and the ability to create atomic samples has become quite standard. Here, we will present the concepts of creating two specific atom traps; namely magneto-optical traps (MOTs) and far-off-resonance traps (FORTs). MOTs involve the process of laser cooling intertwined with the use of a magnetic field to create large, but dilute samples. FORTs rely on optical dipole forces to trap atoms in samples that are not as large as MOTs, but which can be many orders of magnitude more dense [11].

3.1 MAGNETO-OPTICAL TRAPS

Magneto-optical traps have become an essential part of cold atoms physics. What started out 30 years ago [64] as a ground-breaking method for trapping atoms has now turned into just another basic step in an experiment. MOT's are probably the simplest way to create a large collection of cold atoms and they typically serve as a reservoir for more advanced traps such as FORTs, optical lattices, and magnetic traps. While the future may prove to use more novel, general techniques for producing cold atoms [65], MOTs for the time being are the standard. We discuss briefly the mechanisms that allow atoms to be confined in MOTs and then describe how MOTs are made in practice.

3.1.1 THEORY BEHIND MAGNETO OPTICAL TRAPS

From its name, optical implies the presence of a light field that will induce a scattering force to cool the atoms. This will require some background into a simple two-level atom interacting with an external field and presentation of the optical Bloch equations. As it is not only required that the atoms move slowly, but that they are also confined spatially, the role of the magnetic field will also be explained.

Two-level Atom in an External Field

In order to understand the trapping mechanisms of a MOT, we must see how an atom interacts with an external field. The Hamiltonian is again centered around the electric dipole interaction and is given by,

$$\hat{H} = \hbar\omega_a\hat{\sigma}_z - d_{eg}\left(\hat{\sigma} + \hat{\sigma}^+\right)E_{ext} \tag{64}$$

where $\hat{\sigma}_z = |e\rangle\langle e|$ and determines the occupation of the excited state. The electric field E_{ext} will be taken as real. The free electromagnetic field (12) and its interaction with the atom has been left out, but it will be inserted later by hand. The ability to explain the forces on the atom requires us to understand the dynamics of the state populations which are represented by the diagonal elements of the density matrix,

$$\hat{\rho} = \begin{pmatrix} \rho_{ee} & \rho_{eg} \\ \rho_{ge} & \rho_{gg} \end{pmatrix}, \tag{65}$$

where ρ_{ee} and ρ_{gg} are the excited and ground state populations respectively. ρ_{eg} and ρ_{ge} are some times referred to as the optical coherences and will be shown later to correspond to the polarization field of the atom. By use of Liouville's equation, rate equations can be obtained for the density matrix elements given by,

$$\dot{\rho}_{ee} = -\frac{i}{\hbar}\left(\rho_{eg}d_{ge}E_{ext} - \rho_{ge}d_{eg}E_{ext}\right) - \Gamma\rho_{ee} \tag{66a}$$

$$\dot{\rho}_{gg} = -\frac{i}{\hbar}\left(\rho_{ge}d_{eg}E_{ext} - \rho_{eg}d_{ge}E_{ext}\right) + \Gamma\rho_{gg} \tag{66b}$$

$$\dot{\rho}_{eg} = -\frac{i}{\hbar}\left[\hbar\omega_a\rho_{gg} + (\rho_{ee} - \rho_{gg})d_{eg}E_{ext}\right] - \frac{\Gamma}{2}\rho_{eg} \tag{66c}$$

$$\dot{\rho}_{ge} = \dot{\rho}_{eg}^* \tag{66d}$$

The effects of the vacuum field have been added by hand through insertion of the dephasing rates Γ and $\Gamma/2$ [66]. To simplify the analysis we can assume the electric field is represented by,

$$E_{ext} = \frac{1}{2}A(\mathbf{r},t)e^{i\mathbf{k}\cdot\mathbf{r}-i\omega t} + \text{c.c} \tag{67}$$

where $A(\mathbf{r},t)$ is a slowly varying function in $\mathbf{r}$ and t, and the electric field is monochromatic with frequency ω. Additionally, we will also assume that the optical coherence ρ_{eg} can be put into the same form,

$$\rho_{eg} = \tilde{\rho}_{eg}(\mathbf{r},t)e^{i\mathbf{k}\cdot\mathbf{r}-i\omega t} \tag{68}$$

where $\tilde{\rho}_{eg}$ is also a slowly varying function in $\mathbf{r}$ and t. Its dependence on $\mathbf{r}$ has been inserted for generality. Substituting (67) and (68) into (66c) and dropping the rapidly oscillating terms,

$$\dot{\tilde{\rho}}_{eg} = -\frac{id_{eg}}{2\hbar}A(\rho_{ee} - \rho_{gg}) - (\Gamma/2 - i\Delta)\tilde{\rho}_{eg}, \tag{69}$$

and $\Delta = \omega - \omega_a$. We assign a value to the population difference $W = \rho_{ee} - \rho_{gg}$ and enforce $\rho_{ee} + \rho_{gg} = 1$ (meaning the system population is conserved) to get the *optical Bloch equations*,

$$\begin{aligned}
\dot{W} &= -\Gamma(W+1) + i(\Omega\tilde{\rho}_{ge}^* - \Omega^*\tilde{\rho}_{eg}) \\
\dot{\tilde{\rho}}_{eg} &= -\frac{i}{2}\Omega W + (i\Delta - \Gamma/2)\tilde{\rho}_{eg}
\end{aligned} \tag{70}$$

where $\Omega = \frac{d_{eg}}{\hbar}A$ is the Rabi frequency. The form of (70) along with Maxwell's equations are helpful in determining the transient response of the atom. However, we are only concerned with the steady state populations. Setting the time derivatives in (70) to zero we obtain,

$$\begin{aligned}
W &= -\frac{1 + 4(\frac{\Delta}{\Gamma})^2}{1 + 4(\frac{\Delta}{\Gamma})^2 + s_0} \\
\tilde{\rho}_{eg} &= \frac{i\Omega}{\Gamma}\frac{1 + 2i\frac{\Delta}{\Gamma}}{1 + 4(\frac{\Delta}{\Gamma})^2 + s_0},
\end{aligned} \tag{71}$$

where $s_0 = 2|\Omega|^2/\Gamma^2$ is the on-resonance saturation parameter and gives a measure of how strongly the atom is being driven.

Laser-Cooling

When an atom is subjected to a beam of light it will experience a force in the direction of the incident photon. After absorption, this photon is emitted in a random direction such that on average the emission exerts zero force. Therefore, the net average force the atom feels comes from the initial absorption which is written as [67, 68],

$$F_{abs} = \hbar k\Gamma\rho_{ee} = \frac{\hbar k s_0 \Gamma/2}{1 + 4(\frac{\Delta}{\Gamma})^2 + s_0}, \tag{72}$$

using the expression for W and the conservation of population to solve for ρ_{ee}. This has the interpretation that there is a change in momentum for the atom given by $\hbar k$ in a time interval Γ^{-1} regulated by the effect of detuning and saturation.

An atom allowed to move in free space will actually see a detuning $\Delta \pm |\omega_D|$ due to the Doppler effect where $\omega_D = \mathbf{k} \cdot \mathbf{v}$ and $\mathbf{v}$ is the velocity of the atom. If we limit ourselves to movement in one dimension, we can see that in order to cause the atom to absorb a photon,

regardless of the direction of its velocity, we will have to impose two counter-propagating laser beams. The force then exerted is $F_{total} = F_+ + F_-$, where

$$F_\pm = \frac{\pm \hbar k s_0 \Gamma / 2}{1 + 4(\frac{\Delta \mp |\omega_D|}{\Gamma})^2 + s_0} \tag{73}$$

If we only consider small velocities such that $kv \ll \Gamma$, the total force reduces to

$$\mathbf{F}_{total} = \frac{8 \hbar k^2 \Delta s_0 \mathbf{v}}{\Gamma \left[1 + 4(\frac{\Delta}{\Gamma})^2 + s_0 \right]} \tag{74}$$

Choosing the sign of $\Delta < 0$ causes the force to oppose the velocity and dampens the motion. By overlapping three orthogonal sets of beams and retro-reflecting them one can make what is called an *optical molasses* [69], and realize a sample of cold atoms in free space. Unfortunately this method cannot achieve absolute zero velocity as fluctuations in the absorption and emission processes lead to a form of heating [68]. The *Doppler cooling limit*, $T_D = \frac{\hbar \Gamma}{2 k_B}$, is reached when the rate of cooling due to (74) is equal to the heating from absorption and emission fluctuations [67]. For alkali metal atoms this corresponds to a temperature of a several hundred μK. This limit can be overcome with the help of polarization-gradient cooling or *Sisyphus cooling* [70, 71]. Sisyphus cooling occurs as the counter propagating beams form a standing wave whose electric field polarization changes as a function distance to create an oscillatory, spatially-varying light shift in the ground state that depends on the particular Zeeman sublevel. When atoms pass through regions where the light shift is the largest they encounter a potential that is positive and there kinetic energy is reduced. By absorbing a photon at these locations and subsequently decaying into the portion of the standing wave that is at a lower potential, the atoms lose kinetic energy. This process cools the atoms and allows for temperatures below the Doppler limit.

Adding a Magnetic Field

Due to the spatially random nature of light absorption and re-emission, an atom will eventually diffuse its way out of the cross hairs of the laser beams and be lost from the optical molasses. This happens as the force (74) is only velocity dependent and cannot confine it spatially; i.e. there is no restoring force. To do so, requires the use of a magnetic field along with the internal Zeeman structure of the atom. If a magnetic field with the form $B = A_0 z$ is applied in the vicinity of the atom, it will feel a position-dependent Zeeman shift $\omega_z = \mu A_0 z / \hbar$. Here, μ is the effective magnetic moment of the transition. The force from

(74) can be readjusted for this effect,

$$F_\pm = \frac{\pm \hbar k s_0 \gamma/2}{1 + 4(\frac{\Delta \mp |\omega_D| \pm \omega_z}{\Gamma})^2 + s_0} \tag{75}$$

Considering a basic Zeeman structure and magnetic field orientation as in Fig. 10, if an atom moves in the $+z$ direction it will experience a negative Zeeman shift of the $M_J = -1$ level such that it is brought into resonance with the red-detuned laser beam. Making the laser beam σ_- circularly polarized causes an increased chance of absorption and greater scattering force. Likewise, atomic motion in the other direction induces the same effect but with the $M_J = +1$ and the beam is σ_+ polarized. Appropriate choices of Δ and A_0 give an optimal trapping force and substantially increase the capture velocity compared to optical molasses (5 m/s $\to$ 50 m/s). Indeed one can see that the resulting force is now restoring by expanding the denominator so that,

$$F_{total} = -\alpha v - \beta z \tag{76}$$

where the force has just been written out for one dimension, α is given by the prefactor in (74), and $\beta = \frac{\mu A_0}{\hbar k} \alpha$. Finally, we have a magneto-optical trap [64]. Using it, as many as 10^{10} atoms can be trapped in 2 cm diameter beams with average temperatures around 100μK.

3.1.2 REALIZING A MAGNETO-OPTICAL TRAP

For our experiments we trap ^{87}Rb atoms on the $5^2 S_{1/2}$ $F = 2 \to 5^2 P_{3/2}$ $F = 3$ nearly closed hyperfine transition (Fig. 11). Here $F = I + J$ and is the total atomic angular momentum where $I = 3/2$ and is the nuclear spin and J is total electron angular momentum written as the subscript next to the orbital angular momentum numbers S and P. The trapping beam derives from a laser diode (Thorlabs DL7140-201S) in a Littrow configuration (Fig. 12), where a small portion of the emitted light is sent back into the diode with a grating. The laser diode is driven by a homemade current controller and temperature stabilized with a thermo-electric cooler (Marlow Industries DT12-6-01L) working in a feedback loop with a thermistor (Thorlabs TH10K) and homemade temperature cooler. The linewidth of the laser in this setup is $\sim$ 500kHz.

The laser is frequency stabilized using Doppler-free saturated absorption spectroscopy [72] in conjunction with feedback provided by a lock-in amplifier and homemade servo-circuit. The lock-in amplifier is used to current modulate the diode and produce a derivative-like signal where the laser can be locked to a zero-crossing. Once locked, the servo-circuit corrects for temperature and current drifts via adjustment of a piezo connected to the diode gating.
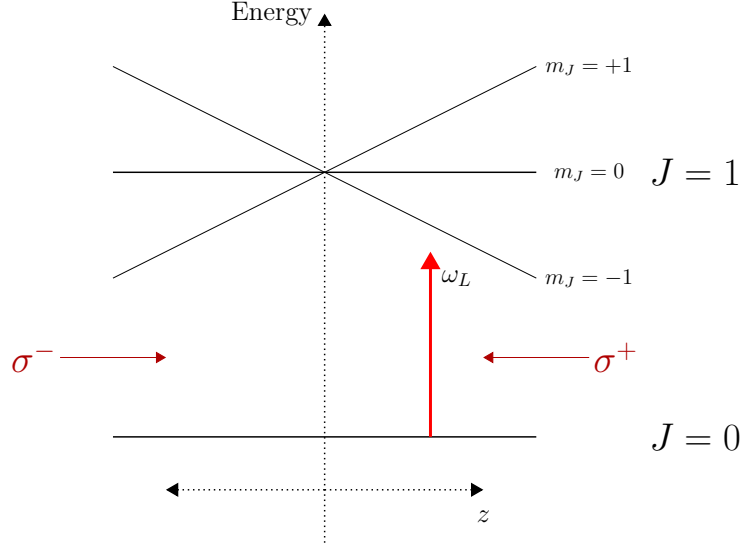
FIG. 10: Energy diagram for an atom with a $J = 0 \rightarrow J = 1$ transition in the presence of a magnetic field and a laser with frequency ω_L. As the atom moves to the right, the Zeeman shifts brings the laser frequency into resonance and causes there to be a near-resonant scattering force from the σ^- beam. Likewise, for an atom moving to the left the M_J level is brought down and it is more likely to absorb the σ^+ beam.

For our application, we lock to the $F' = 2$ and $F' = 3$ cross-over peak (Fig. 14). This laser provides the main trapping beam for the MOT and is appropriately called the "MOT laser." After passing through the saturated absorption the beam is frequency shifted by a double pass acousto-optic modulator (AOM) (Brimrose TEM-200-50-.780) and then injected into a distributed feedback laser (EYP-DFB-0780). This laser is driven by a SRS LDC501 controller and serves as a stage of power amplification for the trapping beams (sometimes called a "slave laser" as it follows the frequency of the master (MOT) laser). The beam is then sent through a final AOM (Gooch and Housego R23080-1-LTD) for fast chopping and over to the vacuum chamber table. A portion of the beam, which will be described later, is sent to a secondary slave laser which is used to probe the atoms in experiment. This setup is featured in Fig. 13.

As there is a small probability for population transfer to the $F = 1$ ground state by inelastic optical scattering from the $2 - 2$ transition, an additional laser must be used. This laser is tuned from the $F = 1$ to the $F' = 2$ excited state and serves to repump the atoms back into the $F = 2$ ground state; accordingly we call this laser the repumper. It is frequency stabilized in the same manner as the MOT laser and its optical setup and
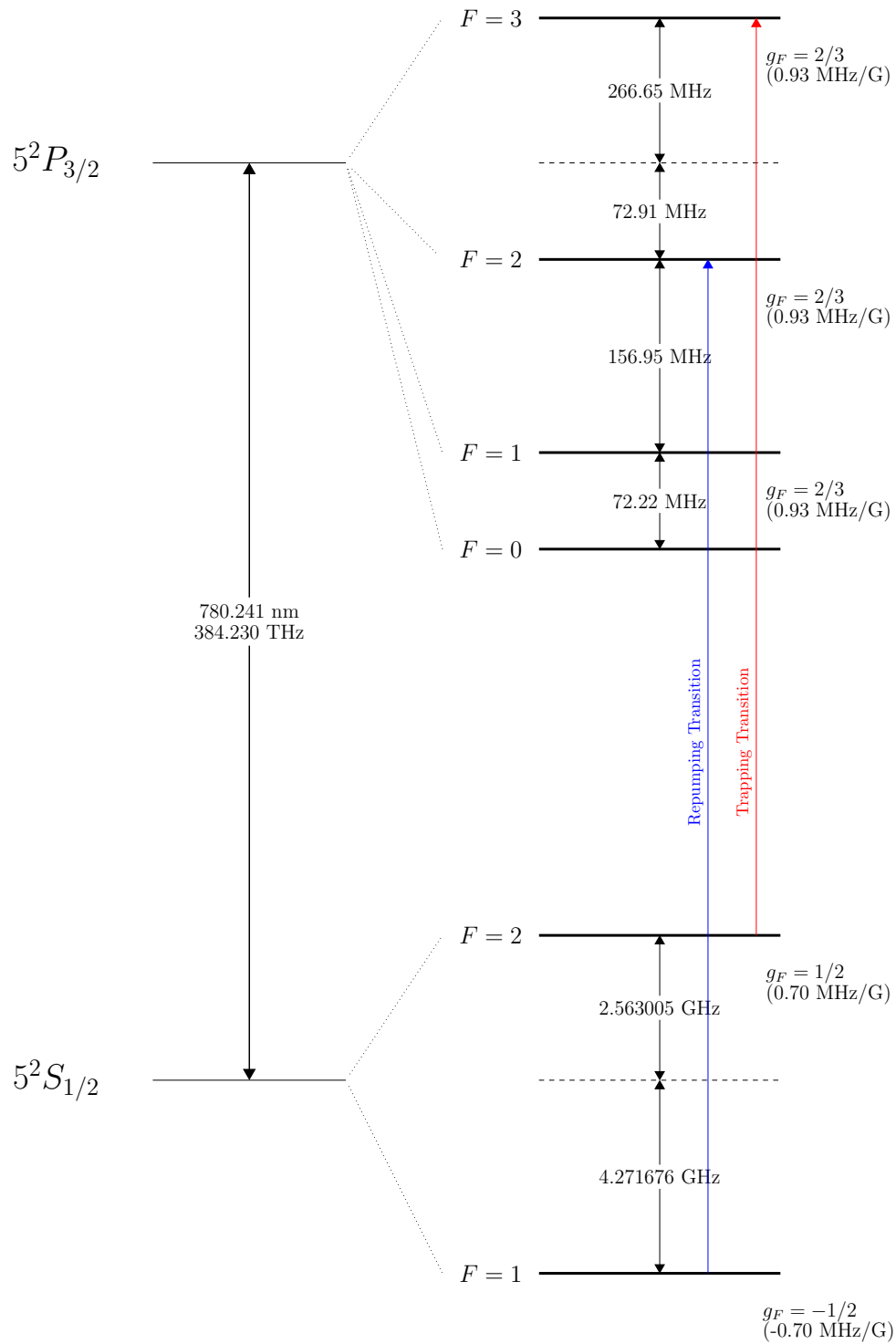
FIG. 11: ^{87}Rb energy level diagram (vertical axis not to scale). The D_2 transition corresponds to the $5^2S_{1/2} \rightarrow 5^2P_{3/2}$ electronic transition.
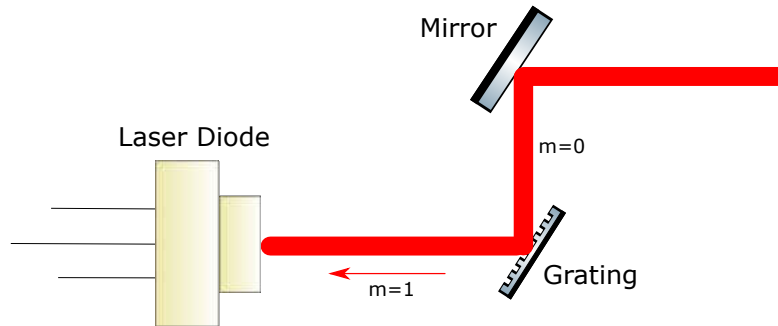
FIG. 12: Schematic of the tunable diode laser in the Littrow configuration. The 1st order beam (m=1) is injected back into the diode and the zeroth order beam (m=0) is sent out. A mirror is added to the output to adjust for beam deflection as the grating is tilted (tuning the laser).
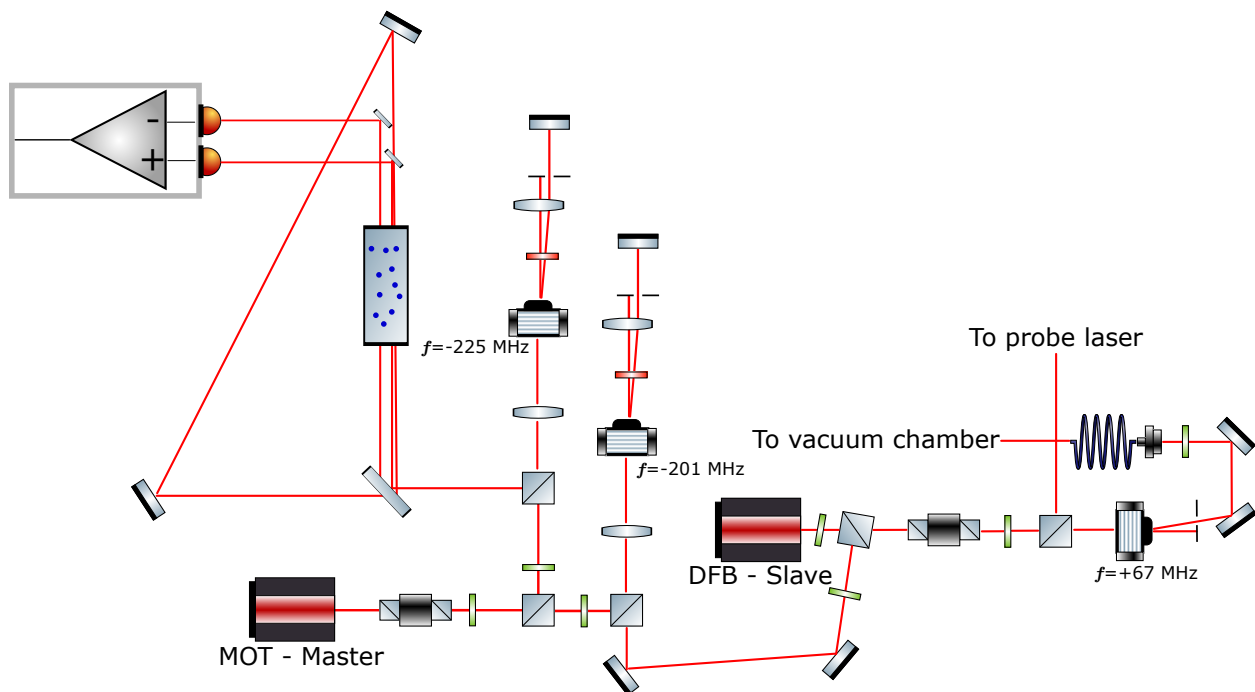
FIG. 13: Optical setup for the MOT laser. Appendix B gives a listing of all optical elements used throughout the dissertation.
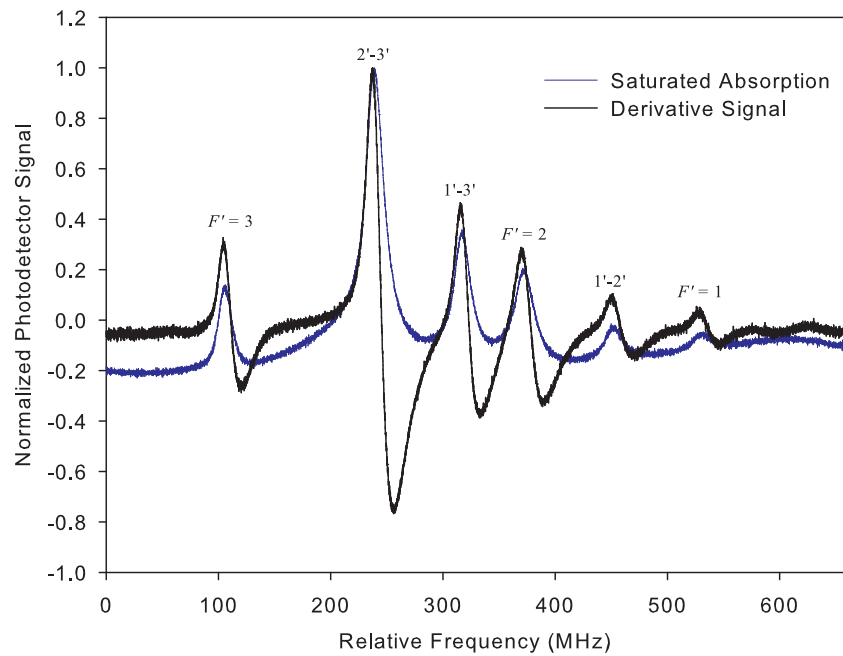
FIG. 14: Saturated absorption spectrum and derivative locking signal for the MOT laser. The transitions for $F = 2$ to an excited F' state are labeled as F'. The crossover peaks are denoted as combinations of the excited state hyperfine energy levels. Here, we lock to the $2' - 3'$ crossover transition. In reality, the peaks to left side of the trace are at a higher frequency but here are represented as they are observed in the lab due to the particular triggering used on the oscilloscope.
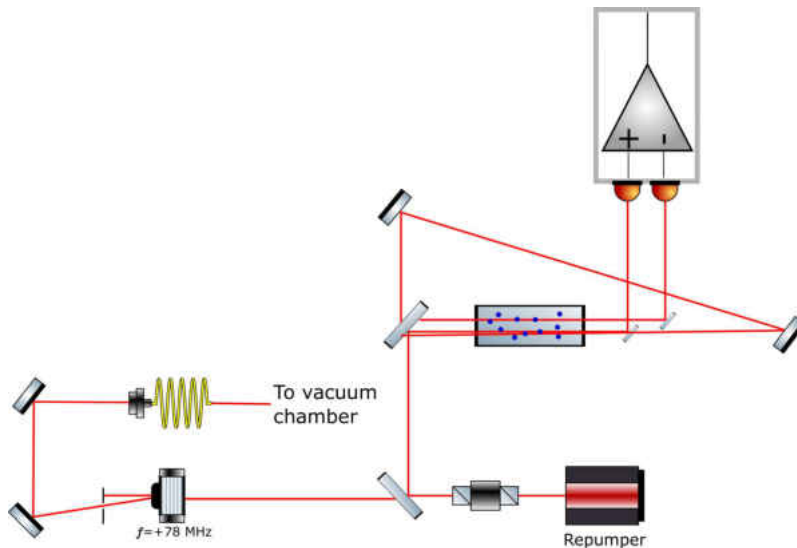
FIG. 15: Optical setup for the repumper laser.

associated saturation absorption are pictured in Figs. 15 and 16, respectively.

Both the MOT and repumper beams are passed over to a second optics table, where the beams are enlarged and a shutter is added to provide additional beam chopping (Fig. 17). The vacuum chamber is pumped with a diode ion pump (VacIon 20 l/s model 911-5036) to a pressure around 10^{-9} Torr. A set of Helmholtz coils is positioned above and below the chamber to provide the necessary magnetic field gradient (~ 10 Gauss/cm) for trapping as discussed in the MOT theory section. Typically, the MOT laser power is kept around 24 mW (beam area ~ 1 cm^2) and the detuning at $\Delta = -3\Gamma$ with respect to the $F = 2$ to $F' = 3$ transition, which are both determined empirically from optimizing the MOT and FORT atom number. The repumper power is ~ 3.5 mW (beam area ~ 1 cm^2) and is tuned to be resonant with the $F = 1$ to $F' = 2$ transition. Atoms are supplied to the chamber by the use of getters (SAES Rb/NF/3.4/12 FT 10 + 10). The getters are dispensers coated with rubidium chromate (Rb_2CrO_4) and a reducing agent (St 101). Running current through the getter generates heat to which a reduction reaction occurs and liberates the rubidium [73]. Once the atoms are trapped (loading time $\sim 3 - 6$ seconds depending on Rb getter current), the sample can be characterized with a charge-coupled device camera (CCD) and photodetector by measuring fluorescence. This characterization, which will be the focus of the next session, lays out how the MOT's atom number, size, and temperature are determined.
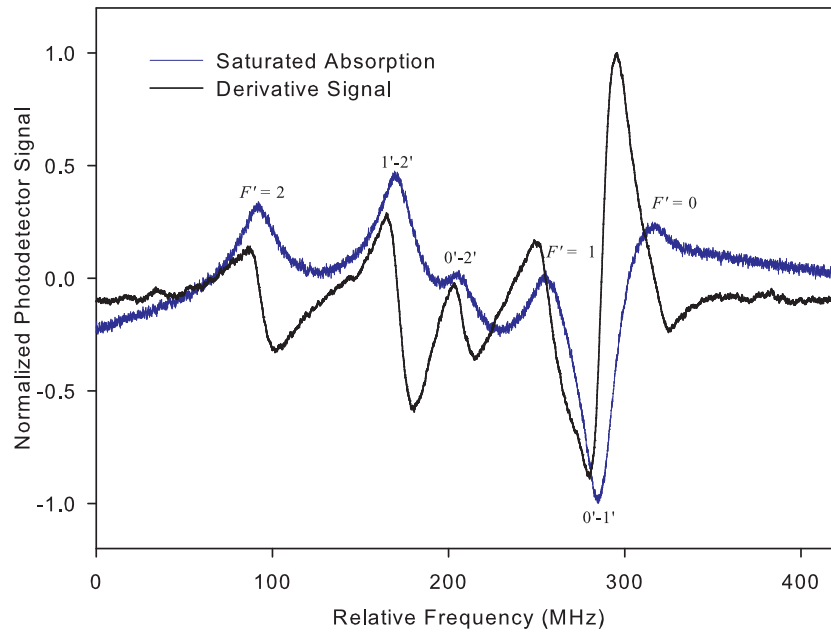
FIG. 16: Saturated absorption spectrum for the repumper laser. The initial ground state is $F = 1$ and we lock to the $1' - 2'$ crossover transition.
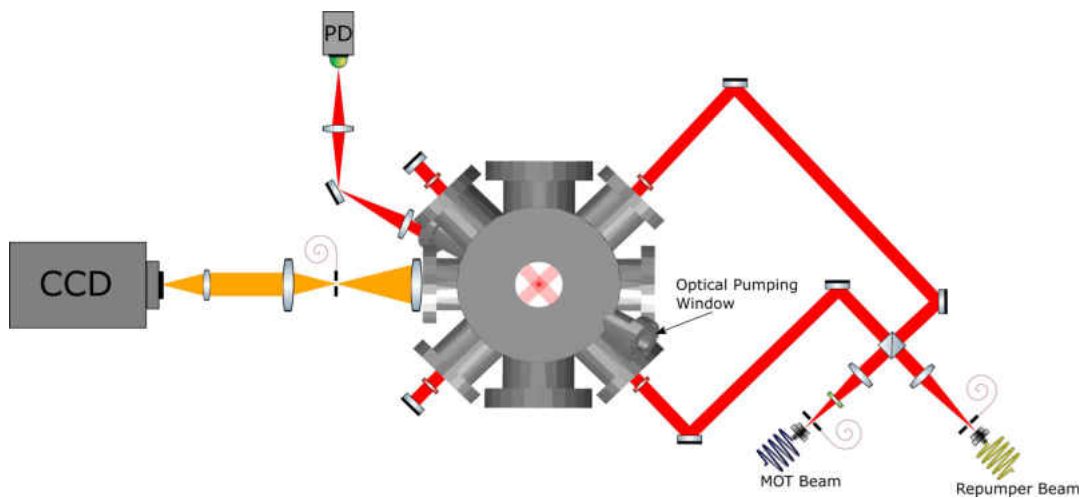
FIG. 17: Optics setup from a top view of the vacuum chamber. The atom fluorescence is represented in orange and is collected on a CCD for sample characterization. Not pictured are the vertically-oriented trapping beams for sake of clarity.

3.1.3 CHARACTERIZATION

Atom Number Determination

The number of atoms is measured by an optical pumping technique [74, 75] where atoms initially in the $F = 2$ ground state are probed on the $F = 2 \to F' = 2$ transition and, by repeatedly scattering, will eventually end up in $F = 1$ ground state and will not be resonant with the probing beam. By monitoring the transmission of the probe beam, the number of atoms can be backed out if the associated branching ratios are known. The branching ratios can be determined by calculating the decay rate for ^{87}Rb taking into effect its multilevel structure [76],

$$\Gamma = \frac{w_a^3}{3\pi\epsilon_0\hbar c^3} \frac{2J+1}{2J'+1} |\langle J||d||J'\rangle|^2 \sum_F S_{FF'}, \tag{77}$$

where

$$S_{FF'} = (2J'+1)(2F+1) \begin{Bmatrix} J & F & I \\ F' & J' & 1 \end{Bmatrix}^2 \tag{78}$$

is the normalized strength factor or partial width of the $F' \to F$ decay. J and J' are the ground and excited state electronic angular momentum values, respectively. I denotes the nuclear spin and the electron dipole moment operator is taken to be approximatively diagonal in its basis [77]. Each strength factor $S_{FF'}$ corresponds to the branching ratio for the $F' \to F$ decay, and evaluation for $2 \to 2$ and $2 \to 1$ produces $1/2$ for each. Using this knowledge of the branching ratios, one can deduce that it takes on average 2 photons to completely pump the atom to the $F = 1$ ground state.[1]

The optical pumping technique is performed by sending a laser beam resonant with the $F = 2 \to F' = 2$ transition through one of the vacuum chamber windows, as indicated in Fig. 17, and collecting the transmitted light with a photodetector on the other side. One data run is performed with no MOT present to calibrate the laser power to the photodetector signal and to see what the unperturbed pulse signal is. With the MOT present, the laser beam shows an initial absorption period which eventually approaches the steady state value (Fig. 18). During the pumping cycle, the repumper beam is turned off and the magnetic field is left on. The required pulse length varies depending on laser detuning and power, but

---

[1]The number of photons scattered can be estimated by considering the probability that the atom returns to the initial ground state ($F = 2$) in subsequent events. With each return to the original ground state, the atom will scatter an additional $1 \times (\frac{1}{2})^n$ photons (n being the number of events). Adding up all contributions gives the total number of photons scattered: $N_{photon} = 1 + \frac{1}{2} + (\frac{1}{2})^2 + \cdots = 2$. The process essentially follows from a Bernoulli distribution.

for $P_{\mathrm{L}} \simeq 20~\mu$W (beam waist ~ 4mm) on resonance the pumping time typically takes no more than $500~\mu$s. Each data run is accumulated for 16 cycles and the difference between the no sample-present run and the sample-present run gives the total absorbed light. The number atoms is then given by,

$$N_A = \frac{\lambda}{2hc}\chi \int dt V(t) \tag{79}$$

where χ is the conversion from beam power to photodetector signal and $V(t)$ is the photodetector signal as a function of time. The factor of $1/2$ accounts for the fact that each atoms scatters on average 2 photons. The method is very robust for varying experimental parameters and requires very little time to perform. It also more accurate and less cumbersome compared to traditional atom number determination methods such as absorption and fluorescence imaging [74].
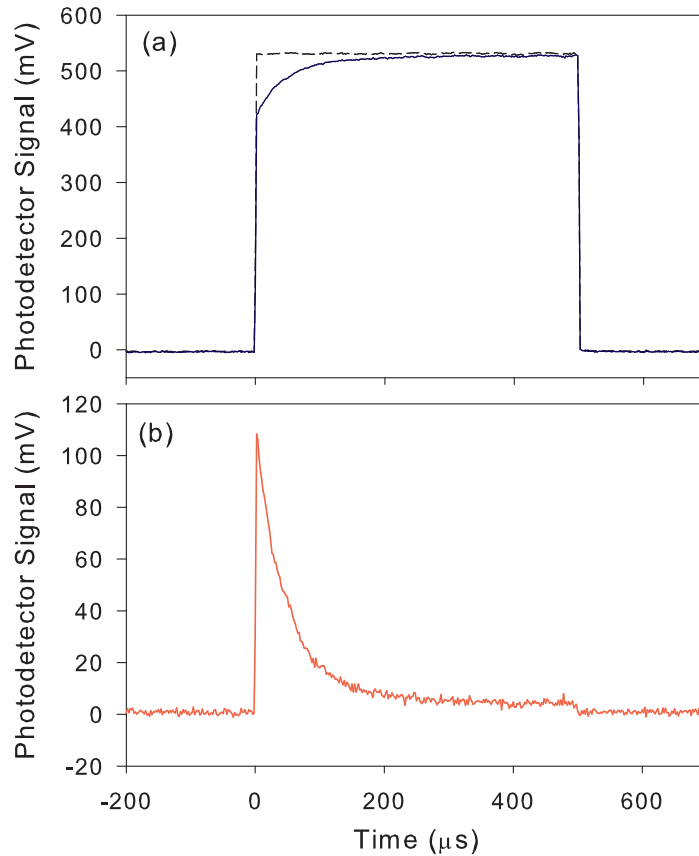
FIG. 18: (a) Optical pumping transmission with the MOT present (solid line) and without the MOT present (dotted line). (b) Difference between the two signals corresponding to $4.01(3) \times 10^8$ atoms.

MOT Temperature

The sample of atoms can be well approximated as having a Maxwell-Boltzmann velocity distribution with a spatial profile given by,

$$\rho(x, y, z) = \rho_0 e^{-x^2/2r_x^2(t)} e^{-y^2/2r_y(t)^2} e^{-z^2/2r_z(t)^2} \tag{80}$$

where $r_i^2(t) = r_i^2(0) + v_i^2 t^2$ and v_i is the root-mean squared velocity of the distribution for a particular direction. The velocity is related to the temperature by $v_i^2 = \dfrac{k_B T}{m}$. Therefore, by observing the spatial profile of the MOT as a function of time the temperature of the atoms can be calculated.

To observe the average motion of the atoms, the trapping beams are turned off for a period of time allowing the sample to expand and then are briefly turned back on to illuminate it. The fluorescence is captured with a CCD camera (PIXIS 1024BR, 13 μm^2 resolution) in a optics train configuration as in Fig. 17. The flash time is chosen as 100 μs to achieve a strong signal without introducing significant image distortion. This process is performed for several different expansion times until enough points are obtained to perform a statistically significant fit to the image radii. The slope of the fit then corresponds to the temperature of the sample. Figure 19 shows an expansion image of the MOT along with a fit to $r_i^2(t)$ vs. t^2. The MOT temperature is typically around 250μK, but this can be significantly reduced by sending it through a compression phase. The compression phase is discussed below for the loading techniques of the FORT. Essentially it involves reducing the radiation pressure within the MOT such that it decreases in size and scatters fewer photons on resonance to give a lower temperature. Getting fluorescence images with the CCD also allows us to make a quick assessment of the atom number if we know the proper atom-to-count ratio between the image signal and atom number determined from methods described in the previous section.

3.2 FAR-OFF-RESONANCE TRAPS

While the operation of a magneto-optical trap relies on radiation pressure from scattering photons, an optical dipole trap operates by spatially confining the atoms in a potential well via a dipole force. This potential well is created by light-shifts induced on the atom's energy levels in the ground state by the interaction with a far-detuned laser beam. Among important parameters for the trap are the wavelength of the laser beam used, the focused spot size, and the beam power. Perhaps the most critical of these specifications is the wavelength used as this will determine how the energy levels shift. Choice of a particular wavelength depends
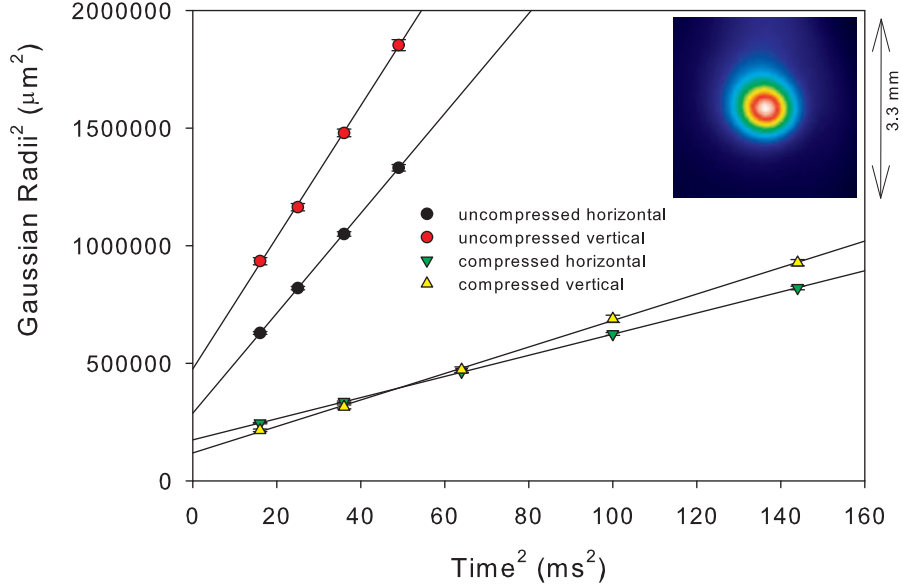
FIG. 19: Temperature measurements for the uncompressed and compressed MOT. Gaussian radii are extracted for the both horizontal and vertical directions on the CCD, squared, and plotted versus time squared. Averaging the slope for both directions gives temperatures of 257 μK and 53 μK for the uncompressed and compressed MOT, respectively. The inset shows a typical CCD image of the MOT.

on the application, but most generally red-detuned lasers are used as they can trap atoms in a simple single pass geometry. This happens as atoms are pulled into more intense regions of the trapping beam. FORTs [78] have been employed almost as long as MOTs but offer a few advantages over their radiation pressure counterparts. These include the ability to create denser atomic gases (up to 10^{14} atoms/cm^3 compared to 10^{10} atoms/cm^3), probe the atoms with no magnetic field present, and evaporatively cool in a pathway to Beose-Einstein condensation [79].

Here we will discuss the theory behind optical dipole trapping as well the methods used to estimate the frequency dependent light shifts. This will be followed by a description of the experimental techniques used to create a FORT and how the sample is characterized.

3.2.1 THEORY OF OPTICAL DIPOLE TRAPS

The potential responsible for optical dipole forces is given by [80],

$$U_{dip} = -\frac{1}{2} \langle \mathbf{d} \cdot \mathbf{E} \rangle = -\frac{1}{2\epsilon_0 c} \text{Re}(\alpha) I(\mathbf{r}), \tag{81}$$

where $I(\mathbf{r})$ is the intensity of the laser field and α is the polarizabilty. For a two-level atom in a field well below saturation, the polarizability is (see Chapter 4)

$$\alpha = -\frac{2|d_{eg}|^2}{\hbar\Gamma} \frac{2\frac{\Delta}{\Gamma} - i}{1 + 4(\frac{\Delta}{\Gamma})^2} \tag{82}$$

where the imaginary portion corresponds to absorptive properties of the atom and the real part to dispersive properties. Dipole traps typically work at frequencies very far from the atomic resonance such that the dipole potential can be written as[2],

$$U_{dip} \simeq \frac{\pi c^2}{w_a^3} \frac{\Gamma}{\Delta} I(\mathbf{r}), \tag{83}$$

where the definition for Γ has been used to rewrite the dipole matrix element d_{eg}. For $\Delta < 0$ the potential is attractive and the energy is minimized in regions of higher intensity (see Fig. 20). It can be seen that the dipole force will fall off as $1/\Delta$ in contrast to the $1/\Delta^2$ dependence for the scattering force. It is this property that allows dipole traps to be effective, as the atoms can scatter very few photons yet still be spatially confined.

For a more realistic atom with a multilevel structure the polarizability is written as [81],

$$\text{Re}(\alpha) = \alpha_0 + \alpha_2 \hat{Q} \tag{84}$$

where α_0 and α_2 are the scalar and tensor polarizabilities, respectively. $\hat{Q}$ is a tensor operator that couples the total angular momentum J to the electric field direction [81, 1],

$$\hat{Q} = \frac{3(\mathbf{u} \cdot \mathbf{J})^2 - J(J+1)}{J(2J-1)}, \tag{85}$$

$\mathbf{u}$ being the polarization of the electric field. The light-shift is then calculated by diagonalizing the combination of the hyperfine interaction and the dipole potential (81) in the hyperfine basis [81] with matrix elements given by,

$$\langle F', m'_F | V_{hfs} - \frac{I(\mathbf{r})}{2\epsilon_0 c} \left(\alpha_0 + \alpha_2 \hat{Q} \right) | F, m_F \rangle. \tag{86}$$

---

[2]The expression (83) has been written down assuming the rotating-wave approximation, but in some instances the frequency of the laser will be so far detuned that $\omega - \omega_a$ and $\omega + \omega_a$ will be on the same order. In this case, $1/\Delta$ should be replaced by $1/\Delta_{eff}$ where $\frac{1}{\Delta_{eff}} = \frac{1}{\omega - \omega_a} + \frac{1}{\omega + \omega_a}$ [1, 80].
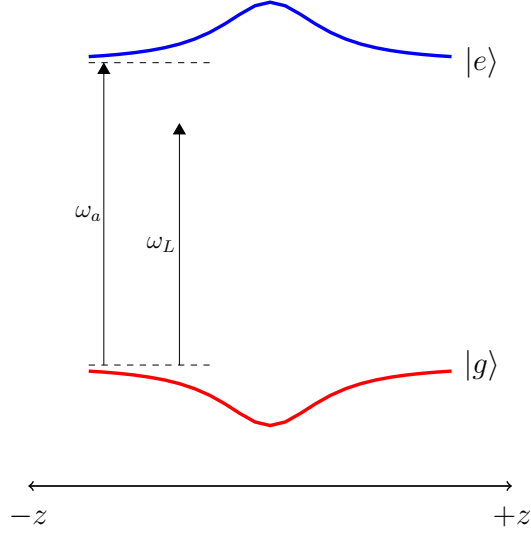
FIG. 20: Light shift created by the dipole potential (83) for the ground state and excited state for a two-level atom; ω_a denotes the transition frequency and ω_L the frequency of the dipole trapping beam. The shift has a z-dependence as determined by the laser intensity (94).

The matrix elements of the hyperfine interaction are [76]

$$\langle F', m'_F | V_{hfs} | F, m_F \rangle = \frac{1}{2} A_{hfs} K + B_{hfs} \frac{\frac{3}{2} K(K+1) - 2I(I+1)J(J+1)}{4I(2I-1)J(2J-1)}, \tag{87}$$

where

$$K = F(F+1) - I(I+1) - J(J+1) \tag{88}$$

and A_{hfs} and B_{hfs} are the magnetic dipole and electric quadrapole hyperfine structure constants, respectively, and I is the total nuclear angular momentum equal to $3/2$ for ^{87}Rb. Taking the trapping beam to be linearly polarized, the matrix elements of $\hat{Q}$ are,

$$\langle F', m'_F | \hat{Q} | F, m_F \rangle = \left[\frac{(J+1)(2J+1)(2J+3)}{J(2J-1)} \right]^{1/2} (-1)^{I+J+F-F'-m_F} \times$$
$$[(2F+1)(2F'+1)]^{1/2} \begin{pmatrix} F & 2 & F' \\ m_F & 0 & -m_F \end{pmatrix} \begin{Bmatrix} F & 2 & F' \\ J & I & J \end{Bmatrix}, \tag{89}$$

which is diagonal in m_F.

Estimates for the values of the polarizabilities can be taken from works of Safranova et al [82, 83, 84, 85, 86]. Here we will describe the general approach and present characteristic results. The polarizability for a particular nL-state (n being the principal quantum

number and L the angular momentum number) is approximately given by the sum of the polarizability of the ionic core of the atom and the valence portion,

$$\alpha^{nL} \simeq \alpha_{core} + \alpha_{val.}^{nL}. \tag{90}$$

For rubidium, $\alpha_{core} = 9.1(5) \, a_0^3$ for the scalar polarizability and $\alpha_{core} = 0$ for the tensor. Here, a_0 is the Bohr radius. The valence contribution to the scalar polarizability is,

$$\alpha_0^v(\omega) = \frac{2}{3(2J_v + 1)} \sum_k \frac{\left| \left\langle k ||\hat{d}||v \right\rangle \right|^2 (E_k - E_v)}{(E_k - E_v)^2 - \omega^2}, \tag{91}$$

where $v = nL$ for a particular nL-state, k is an intermediate state, $\left\langle k ||\hat{d}||v \right\rangle$ is the reduced matrix element between the state of interest and the intermediate state, and ω corresponds to the frequency of the trapping laser. The valence contribution to the tensor polarizability is,

$$\alpha_2^v(\omega) = -4C \sum_k (-1)^{J_v + J_k + 1} \begin{Bmatrix} J_v & 1 & J_k \\ 1 & J_v & 2 \end{Bmatrix} \frac{\left| \left\langle k ||\hat{d}||v \right\rangle \right|^2 (E_k - E_v)}{(E_k - E_v)^2 - \omega^2} \tag{92}$$

where C is

$$C = \left[\frac{5J_v(2J_v - 1)}{6(J_v + 1)(2J_v + 1)(2J_v + 3)} \right]^{\frac{1}{2}}. \tag{93}$$

We take the theoretical values for the reduced dipole matrix elements as quoted in [82, 83, 85] to compute (91) and (92) (see Table 1). Values for the polarizabilites and hyperfine constants for a trapping beam of $\lambda = 1064$ nm are tabulated in Table 2.

Theoretical work has shown that the ground state polarizability is $686.9(9)a_0^3$ [84] and recent experimental studies [87] have measured the excited state polarizabilies directly and found that the scalar and tensor values are $-1149(22)a_0^3$ and $563(22)a_0^3$, respectively. This gives good confidence in the estimated values of Table 2.

The eigenvalues for the combination of the hyperfine and dipole interactions can now be calculated. In Fig. 21(a) it is shown the effect the dipole trapping beam has on the ground state. Because there is no quadrupole interaction for the symmetric S orbital, the ground state only experiences a light shift due to the scalar polarizability. This shifts all hyperfine and Zeeman levels equally. For the excited state, the tensor operator $\hat{Q}$ mixes the F-states which gives rise to differential shifts in both the hyperfine and Zeeman levels. The Zeeman levels remain degenerate in $|m_F|$ due to the linear polarization of the laser beam. The z-dependence of the light shift comes from the functional form of the intensity, $I(\mathbf{r})$,

TABLE 1: The reduced dipole matrix elements (RDME) used for calculation of the polar-izabilites for the $5^2S_{1/2}$ and $5^2P_{3/2}$ levels. The wavelengths of the transitions are given for their measured values in air.

$5^2S_{1/2}$[82, 83]		$5^2P_{3/2}$ [85]	
λ_{air}(nm)	RDME (ea_0)	λ_{air}(nm)	RDME (ea_0)
780.03	5.977	1528.95	10.899
794.76	4.231	1366.5	6.047
420.18	0.541	780.027	5.977
421.56	0.333	1528.84	3.633
358.71	0.202	775.76	1.983
359.16	0.115	629.92	1.512
334.87	0.111	740.82	1.35
335.09	0.059	572.44	1.104
		543	0.845
		615.96	0.708
		526	0.672
		775.94	0.665
		629.83	0.506
		565.37	0.466
		572.49	0.37
		539	0.341
		543	0.283
		526	0.225

TABLE 2: Polarizabilities and hyperfine constants for the levels of interest. The polarizabil-ities can be converted to standard units by multiplication by $4\pi\epsilon_0$ [1, 2].

Energy Level	Hyperfine Constants [76]	Polarizabilities (a_0^3)
$5S_{1/2}$	$A_{hfs} = h \cdot 3.417$ GHz	$\alpha_0 = 688$
$5P_{3/2}$	$A_{hfs} = h \cdot 407$ MHz	$\alpha_0 = -1129$
	$B_{hfs} = h \cdot 85$ MHz	$\alpha_2 = 554$

which is taken as a Gaussian-beam [88],

$$I(\mathbf{r}) = I(\rho, z) = I_0 \left(\frac{w_0}{w(z)}\right)^2 \exp\left(-2\rho^2/w^2(z)\right), \qquad (94)$$

where $I_0 = \frac{2P}{\pi w_0^2}$, P is the power of the laser, w_0 is the radius of the beam at the focal point, $w(z) = w_0\sqrt{1 + (z/z_R)^2}$, $z_R = \frac{\pi w_0^2}{\lambda}$ known as the Rayleigh length, and λ is the wavelength of the beam.

For practical purposes it is sufficient to know the shift in the ground state as the atoms will be trapped there and experimental procedures can be adjusted to account for the differential excited state shifts to optimize trap loading. However, for work that is concerned with precision measurements and time-frequency standards [89, 41], it is pertinent to understand in detail the light shifts. Normally, the interest is in finding ways to shift the ground and excited states the same amount and in the same direction such that there is zero relative light shift for an atom in the trap. This can be done with magic wavelength dipole traps [90, 91], where a single trapping beam shifts the excited and ground state levels by the same amount, or by a combination trapping wavelengths [92].

With some background into the physics of how atoms are retained in optical dipole traps, we will now move on to discussing how the traps are realized. The procedure is a more involved than that used to make a MOT and requires fine control over experimental conditions, but the payoff will be in the production of a denser atomic gas and a more compatible sample geometry for experiments on superradiance.

3.2.2 EXPERIMENTAL SETUP FOR THE FORT

The FORT is loaded by tightly focusing a 1064 nm laser beam (IPG, YLR-30-1064-LP PL1211875) through the middle of the MOT (Fig. 22). As there is very little scattering by the atoms from the FORT beam, careful alignment procedures must be used that rely on overlapping the 1064 nm laser with a resonant 780 nm beam and looking for radiation pressure effects on the MOT with a video camera. The switching of the FORT beam is controlled with a high power AOM (Gooch & Housego, I-M080-1.5C10G-4-AM3) with a rise-time ~ 50 ns. The AOM is powered by a Q-switch driver (Gooch & Housego, QC080-15DC-M05-24V) that allows for external attenuation and modulation control.

Once aligned, the MOT is compressed and cooled in the presence of the FORT beam for a period of 70 ms. This is done by reducing the MOT beam detuning from -3Γ to $\sim -10\Gamma$ and reducing the repumper power by a factor of ~ 100. The compression increases the density of atoms around the most intense portions of the FORT and hence increases the chance that
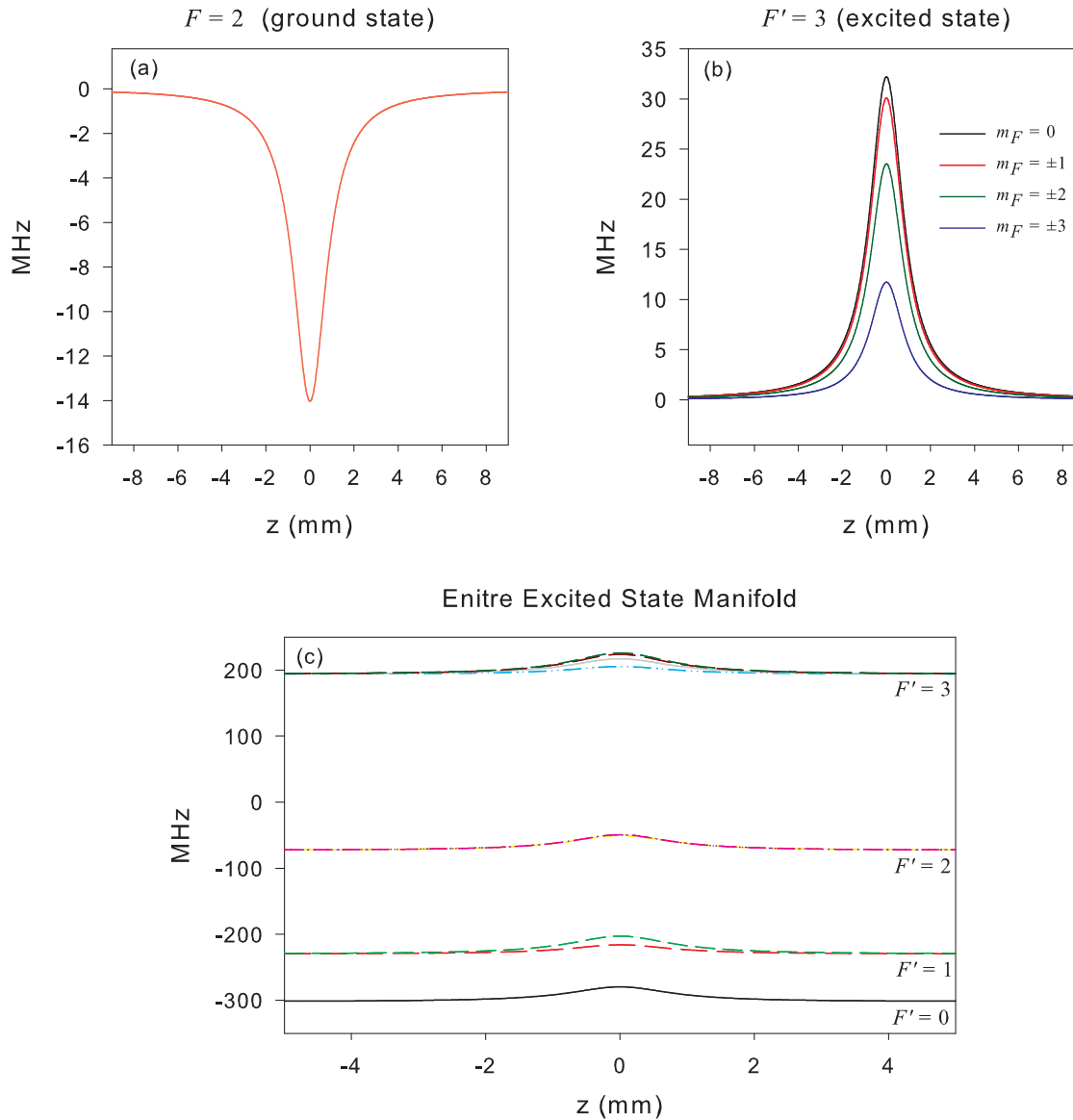
FIG. 21: Shifts of the ^{87}Rb energy levels for (a) the ground state for $F = 2$, (b) the excited state for $F' = 3$, and (c) all excited state hyperfine levels. The beam parameters are $P = 2.12$ W and $w_0 = 18$ μm. For (a) and (b) the shifts are compared relative to the unpertubed energy levels. For (c) the zero corresponds to the relative $5^2P_{3/2}$ level location, in the absence of hyperfine structure.
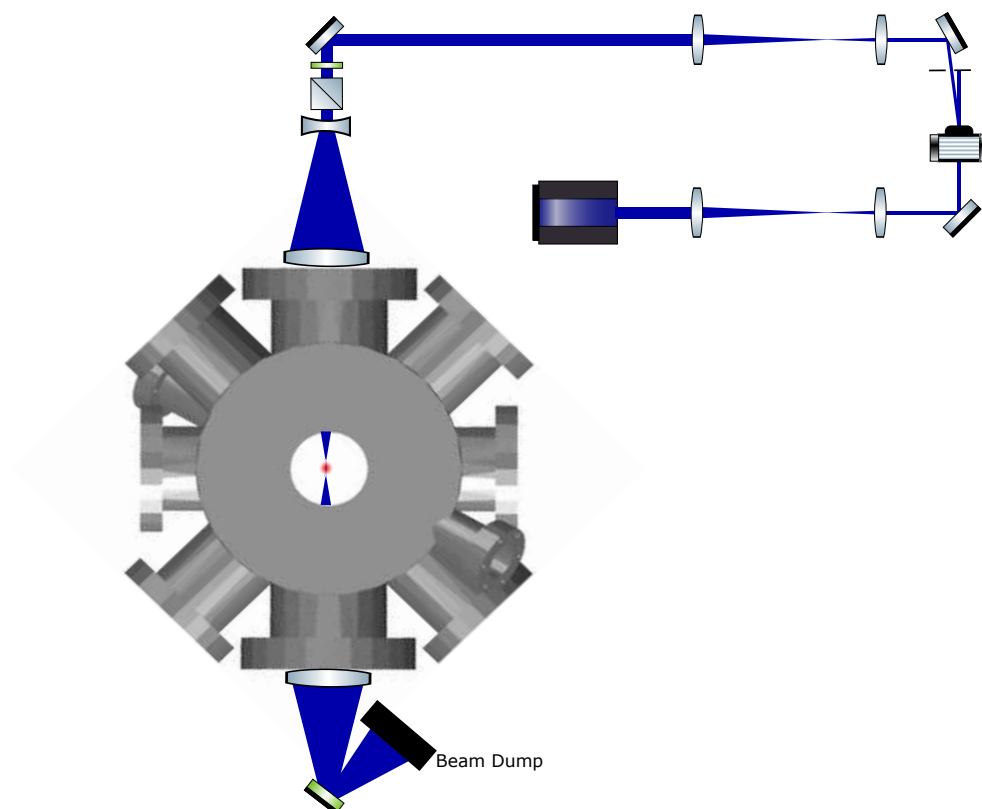
FIG. 22: Optics setup for the dipole trap laser. The mirror on the exit window is dichroic and reflects 1064 nm light, but passes 780 nm. This is needed in the experiments, as discussed later.

they will become trapped.[3] During the process the magnetic field is left on and MOT power is left constant. Some protocols [93, 94] find that the MOT power must be decreased to reduce two-body collisions, but for our trap it was not found necessary. Towards the end of the loading process, the repumper AOM is shut off 4 ms prior to the MOT AOM so as to ensure that most of the atoms get optically pumped to the F=1 ground state. Atoms in the F=1 ground state have a smaller collisional cross section which increases the lifetime of the FORT [80]. Once both AOMs are shut off, the mechanical shutters for each beam are closed to extinguish any light leakage. A diagram for the timing sequence is pictured in Fig. 23.
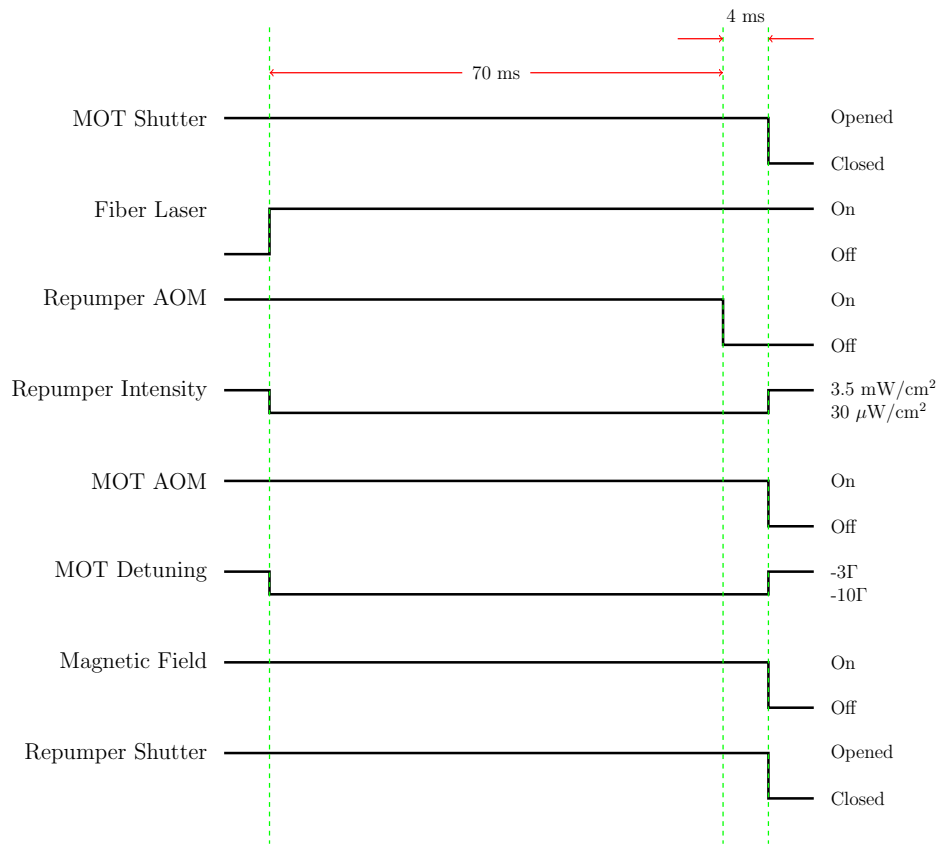
FIG. 23: Timing diagram for FORT loading.

After the MOT and repumper beams are shut off, the atoms are held for typically 200 ms to allow for thermalization. A plot for the number of atoms as a function of time is pictured in Fig. 24 with a double exponential fit to the decay. The initial decay gives approximately the thermalization time and the second decay corresponds to the lifetime of the trap which

---

[3]The atoms, without any other dissipating mechanism, will move through the potential well without becoming trapped as energy is conserved in the process. Dissipation comes about by spontaneous emission which carries away excess energy from the atom's kinetic energy leaving it trapped within the potential well.
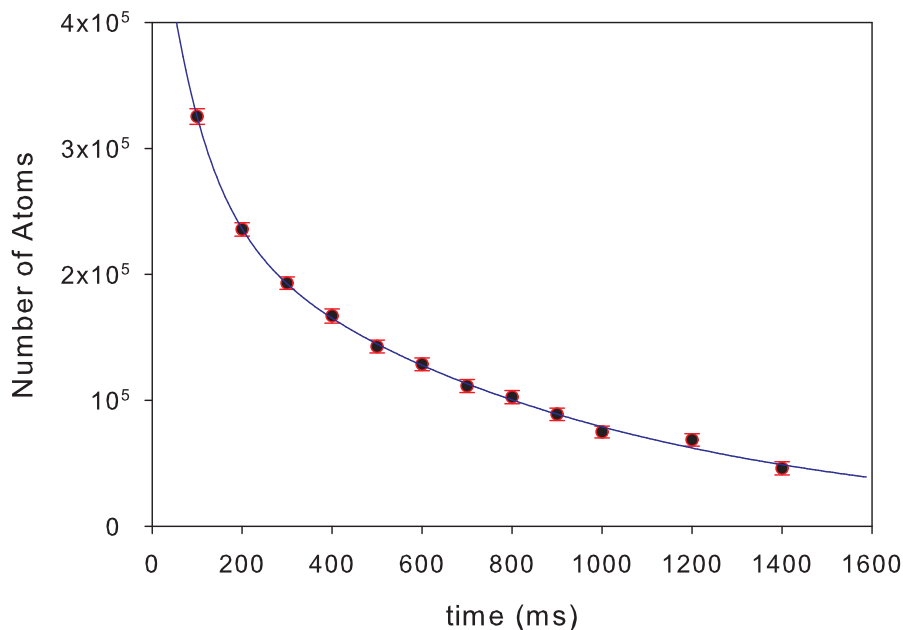
FIG. 24: Hold time of the FORT with a fit to a double exponential. The initial decay gives a time of ~ 90 ms and the long time decay is ~ 830 ms. This sample was created with a beam focus of 13 μm and beam power of 2 W.

is determined by background gas collisions. At a vacuum chamber pressure of 10^{-9}, we get a lifetime of ~ 1 s. The atom number is inferred by taking CCD images of the FORT and converting the pixel counts to atom number using calibration methods discussed in Section 3.1.3.

3.2.3 CHARACTERIZATION

FORT Temperature

The FORT temperature is obtained in much the same way as it is for the MOT: the atoms are released from the trap for a period free expansion and then a CCD image is taken by quickly flashing the MOT and repumper beams for a few different expansion times. While the temperature of the MOT is limited by photon recoil from near resonant scattering, the temperature of the FORT is limited by the trap depth. After the initial period of thermalization, the sample will have a temperature which is a certain percentage of the trap depth. In some cases [94], this can be as low as 10% but it is highly dependent on the

wavelength of the trapping beam and the trap geometry [93, 92, 80]. As a demonstration, Fig. 25 compares the atom temperature for two different well depths. Because the temperature of the atoms is determined solely by the trapping potential, techniques such as evaporative cooling [95, 96] can be used to achieve quantum degeneracy [79, 97] which cannot be done in a MOT.
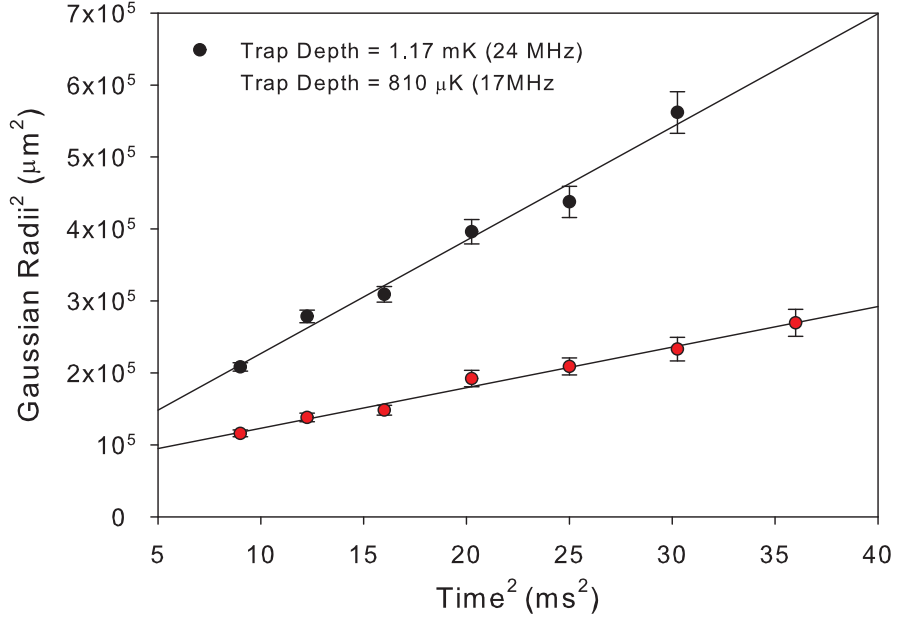
FIG. 25: Temperature of the FORT for two different well depths. For $T_{trap} = 1.16$ mK, the temperature is 164(12) μK and for $T_{trap} = 810$ μK the temperature is 59(3) μK. These temperatures are for the pulsed-technique to be discussed in the experimental arrangement chapter.

FORT Size

Knowing the size of the FORT is important when a high density sample is needed. The radii determined from sample temperature and time dependent extrapolation is not accurate enough to make confident estimates on the unexpanded sample shape. A better method is given by a process called *parametric resonance*. For an atom moving within a one-dimensional harmonic trap potential, the dynamics are governed by

$$\ddot{x} + \omega_0^2 x = 0, \tag{95}$$

where x is the position of the atom and ω_0 is the natural frequency of the trap. If the trap depth is modulated sinusoidally with frequency ω, then (95) can adjusted to

$$\ddot{x} + \omega_0^2 \left(1 + h \cos \omega t\right) x = 0, \tag{96}$$

where h is known as the modulation depth. This specific form is known as *Mathieu's Equation* [98, 99] and for frequencies $\omega = \frac{2\omega_0}{n}$ $(n = 1, 2, ...)$ the system experiences a resonance with decreasing amplitude in n. In the FORT, the potential is shaped by the beam profile,

$$V(r, z) = -V_0 \frac{1}{1 + (z/z_R)^2} e^{-2r^2/w_0^2}. \tag{97}$$

At low temperatures atoms will mostly occupy the very center of the trap such that the expression for the potential can be approximated by

$$V(r, z) \simeq -V_0 + \frac{1}{2} m\omega_r^2 + \frac{1}{2} m\omega_z^2. \tag{98}$$

Here, $\omega_r = \sqrt{\frac{4V_0}{mw_0^2}}$ and $\omega_z = \sqrt{\frac{2V_0}{mz_R^2}}$, which correspond to the resonant frequencies in the radial and longitudinal directions, respectively. In thermal equilibrium the atoms will be represented approximately by a Maxwell-Boltzmann distribution with density profile given by

$$\rho(r, z) = \rho_0 \exp \left(-\frac{V(r, z)}{k_B T}\right). \tag{99}$$

Inserting expression (98) into (99) and assuming the form

$$\rho(r, z) = \rho_0 \exp \left(-r^2/2r_0^2 - z^2/2z_0^2\right) \tag{100}$$

the sample radii are

$$r_0^2 = \frac{k_B T}{m w_r^2} \quad \text{and} \quad z_0^2 = \frac{k_B T}{m w_z^2}. \tag{101}$$

Hence, by knowing the power of the trapping beam and the ground state light shift, a soft modulation will reveal the trap frequencies. Then along with the temperature, the sample shape near the potential minimum can be calculated.

To modulate the trapping beam, a small amplitude sine wave ($\sim 5\%$ of the trap depth) is produced by a function generator (BK Precision, 4084) and added into the analog control line for the AOM driver via a homemade bias tee. The atoms are trapped in the FORT, allowed to thermalize, and then modulated for period of 200 ms at a particular frequency. After the modulation, a fluorescence image is taken and the process is repeated for a different frequency. The number of atoms will be at a minimum once the resonant frequency $2f_0$ has been reached (Fig. 26).
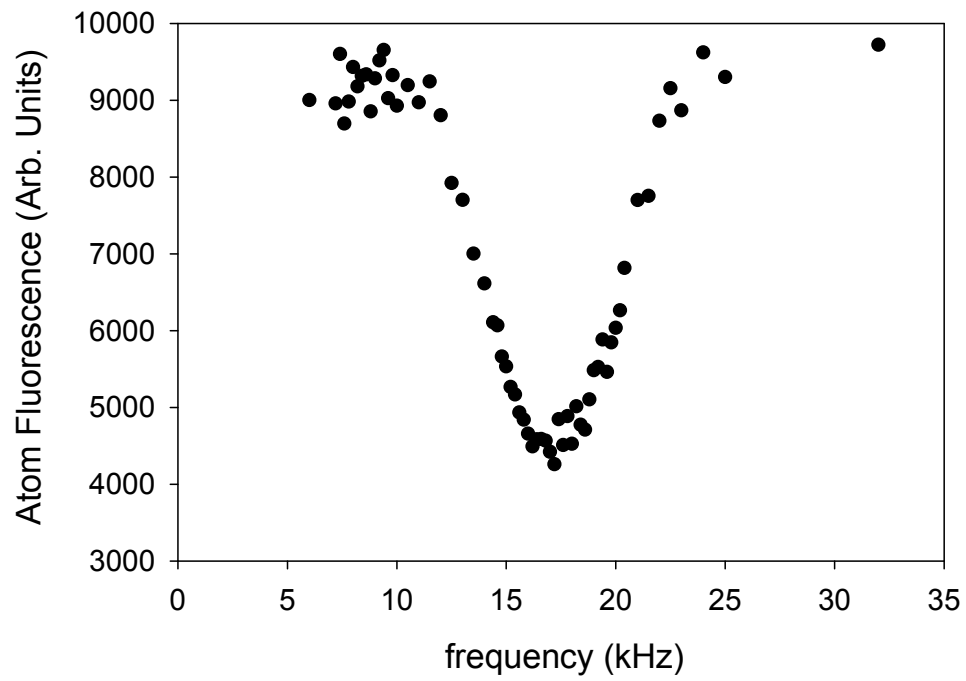
FIG. 26: Parametric resonance response of the FORT near the radial resonance frequency. For a FORT laser power of $P = 2$ W, this gives $r_0 = 2.3$ μm and $z_0 = 123$ μm.

CHAPTER 4

MIPCROSCOPIC LENSING BY A DENSE, COLD ATOMIC SAMPLE

Before interest was taken into the collective time-dependent emission properties of cold atom samples, we focused primarily on the density dependent shifts of the resonance line. To study these effects we created high density atomic samples within the FORT and probed the system in steady state through the most dense portion (Fig. 27). What was observed was a shift of several MHz to the blue of resonance (Fig. 28). Varying the density revealed a linear dependence with respect to the shift as was predicted by theory [12]. However, as further diagnostics were performed it was noticed that the line shift changed depending on where the probe focus was located. As in Fig. 28, the shift moves to the red side of resonance for a different probe focus.

Checking the shape of the transmitted beam on the CCD, it was noticed that the beam profile changed as a function of detuning. As pictured in Fig. 29, for one side of detuning the beam was larger and for the other side of detuning the beam was smaller. This effect is consistent with the dispersive response of the atoms and is analogous to the atoms collectively behaving as a lens. With respect to the transmission curves of Fig. 28, the lensing by the atoms causes the beam to be apertured differently, as a function of detuning, by the collection optics.

In this chapter we will present results that examine the microscopic lensing properties of a high density, cold atomic gas. This involves performing *z-scan* measurements on the atoms [100] where a tightly focused beam is propagated through the profile of the sample.
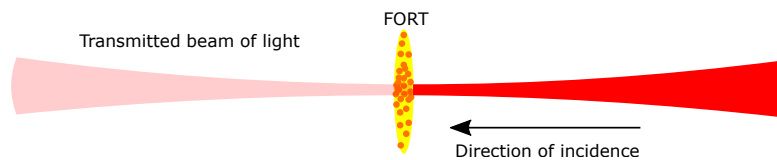
FIG. 27: Earlier experiment where a tightly focused beam is passed through the FORT and the transmitted light is detected on the other side.
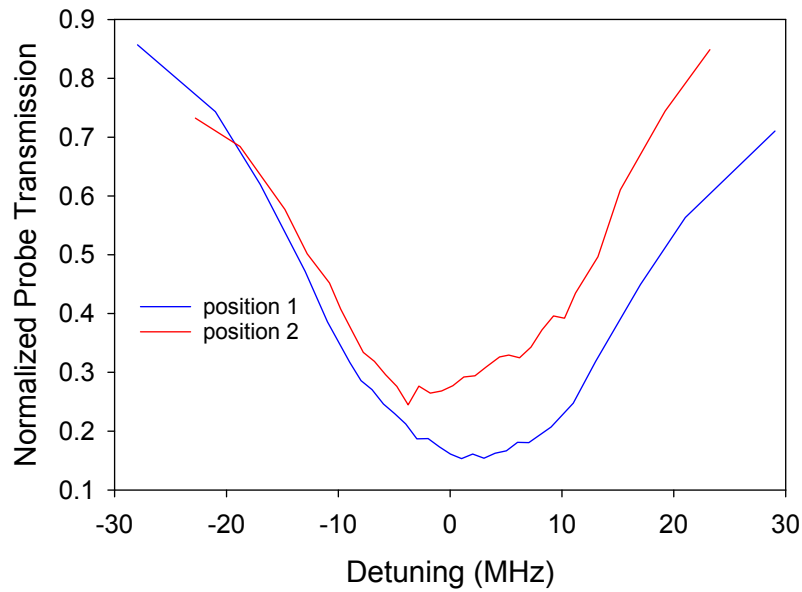
FIG. 28: Normalized probe transmission through the FORT. Position 1 shows an absorption profile shifted to the blue and position 2 shows an absorption profile shifted to the red.
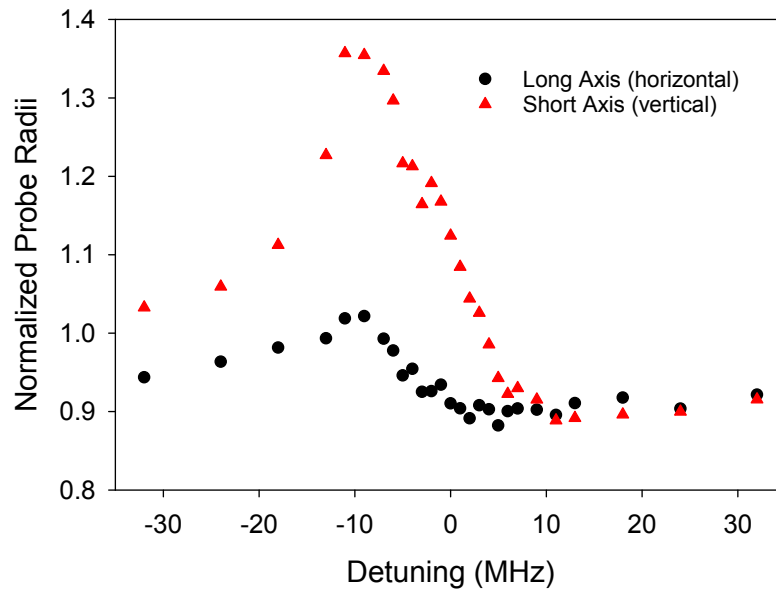
FIG. 29: Fitted radii of the observed probe profile normalized to the probe profile with no sample present. The long axis of the FORT is what is observed in the horizontal direction on the CCD. Likewise, the short axis corresponds to the vertical orientation of the FORT. Because the short axis has a smaller radius of curvature the lensing is more exaggerated.

The results are interpreted using numerical simulations and by modeling the sample as a thin lens with a spherical ball-lens type focal length.

4.1 EXPERIMENTAL SETUP

The experimental setup is shown in Fig. 30(a). There, a linearly polarized probe beam is focused to a 5 μm, $1/e^2$ radius with a peak intensity of 300 μW/cm^2. The beam bisects the sample of ^{87}Rb atoms prepared in a FORT. The FORT in this case has Gaussian radii of $r_x = 255$ μm and $r_y = 3.5$ μm. Atoms in the trap, initially prepared in the 5^2S$_{1/2}$ F=1 ground state, have a temperature ~ 100 μK and number around 9×10^5, giving a peak density of 1.8×10^{13} atoms/cm^3. The experimental duty cycle consists of holding the atoms until they thermalize ($\sim$200 ms), upon which they are pumped to the higher energy F=2 ground level and probed about the resonant 5^2S$_{1/2}$ F=2 $\rightarrow$ 5^2P$_{3/2}$ F$'$=3 D2-line transition. The probe light is focused to controllable locations before and after the FORT by translating the focusing lens, and pulsed for a duration of 10 μs. This interval is chosen to maximize the signal-to-noise without introducing any significant optical pumping. The transmitted light is then spatially filtered with a 0.5 cm diameter aperture and the resulting spatial distribution of intensity captured on a charge-coupled device camera (CCD). The aperture serves as a way to measure intensity and phase fluctuations by a saturable Kerr media, as has been done in other z-scan technique experiments [101, 102]. For each detuning the probe signal is accumulated over 50 runs to acquire good signal-to-noise.

Shown in Fig. 31 is a set of transmission spectra for each focal position of the probe beam. The curves have been normalized by the intensity of the unattenuated probe beam intensity (*i.e.* the probe transmission with no atomic sample present) and, for sake of demonstration, have been given a constant vertical-offset to show the signal progression as a function of z. It can be seen that there is a distinct *flip* in the frequency response of the sample depending on where the beam is focused. This can be attributed to focusing and defocusing effects similar to those described by Labeyrie *et al.* [103], except that in the present case the saturation parameter is low (s$_0$ = 0.2). With observations as in Fig. 31, it easy to perceive why absorption measurements of small, high density samples can be particularly cumbersome to interpret, especially when the numerical aperture of the imaging apparatus is small itself.

Measurements at high-field intensities (s$_0$ $\sim$ 500) were also performed; these yielded curves similar to the ones shown in Fig. 31. The detailed shape of these curves, however, were dependent on the intensity. We attribute this to the fact that, as the $F = 2 \rightarrow F' = 3$ transition is strongly saturated, off resonance scattering on the nearby $F = 2 \rightarrow F' = 1, 2$
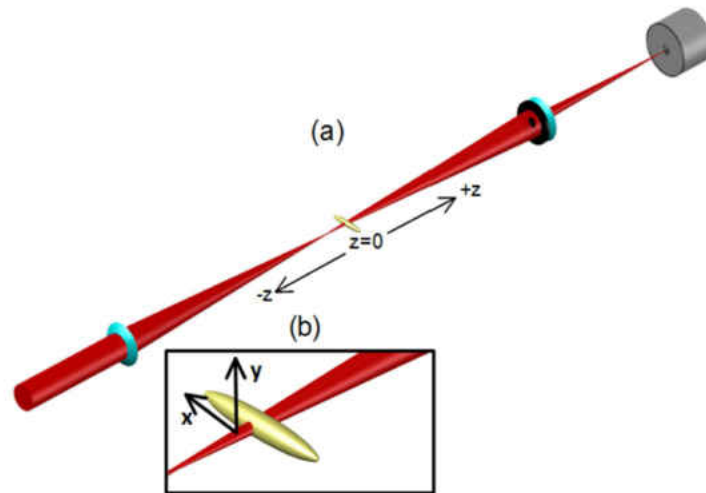
FIG. 30: (a) The experimental configuration used. A near-resonant light beam is incident on a sample ^{87}Rb atoms prepared in a FORT. The transmitted beam is apertured and collected on a CCD camera. Contrary to traditional z-scan measurements, the focal spot of the beam is moved rather than the sample. (b) An enhanced view of the incident probe on the sample, showing the coordinate system used.
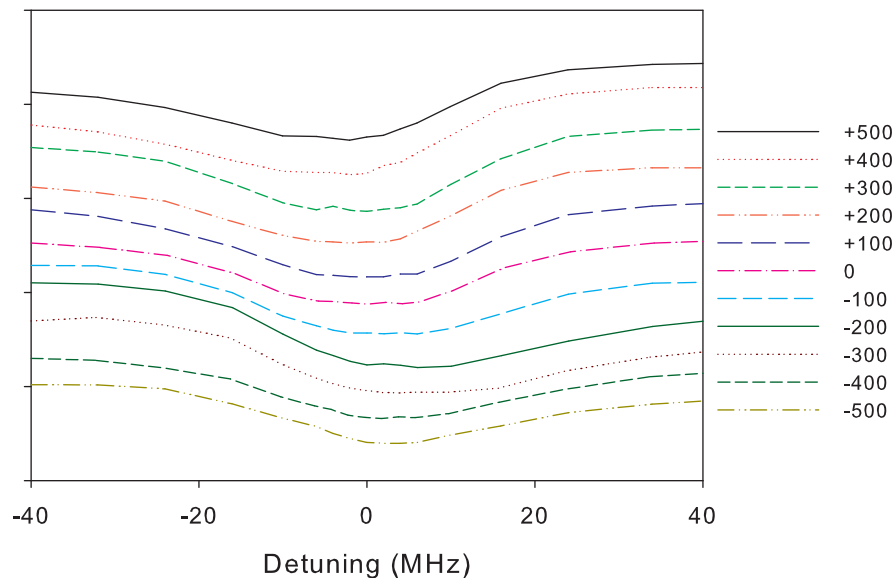
FIG. 31: The frequency response for several different focal locations with respect to the atomic sample. Curves are sequenced in 100 μm steps extending from $z = -500$ μm to $z = +500$ μm. To give a sense of contrast, each spectrum has been given a fixed vertical offset from the previous one.

transitions contribute significantly to the spectral response. Modeling these effects is complicated, and would require calculation not only of the relative strength of these transitions, but knowledge of the scaled cross-sections and line widths, which are generally known to be density dependent [104, 11]. These have not all been determined by measurement or calculation. With this concern, and to maintain the cleanest interpretation of our measurements, we limited our focus to the low-field regime.

4.2 BEAM PROPOGATION SIMULATIONS

As a way to model the z-scan measurements, simulations were performed that closely resembled the experimental conditions. To do this requires a continuation of the discussion started in Section 3.1.1 about the interaction of an atom with an external field. In classical mean-field theory, how a material reacts to an applied electric field can be described by its susceptibility χ [4, 66, 105] with the relation

$$P = \frac{1}{2}\mathrm{p}e^{i\mathbf{k}\cdot\mathbf{r}-i\omega t} + c.c. = \epsilon_0\chi\frac{1}{2}\mathrm{A}e^{i\mathbf{k}\cdot\mathbf{r}-i\omega t} + c.c. \tag{102}$$

where A is the complex electric field amplitude, *c.c.* stands for complex conjugate, P is the polarization of the dielectric medium and p is a slowly varying function that allows the polarization to be written in the same form as the electric field. It is also still assumed that the orientation of the electric dipole is along the direction of the electric field polarization vector. Alternatively, the polarization is defined as the average dipole moment per unit volume,

$$P = \rho_a \langle \mathrm{d} \rangle \tag{103}$$

where ρ_a is the local atomic density assumed to be constant for now. Using the definition of the expectation value of an operator in conjunction with the density operator leads to

$$\langle d \rangle = \mathrm{tr}\left(\hat{\rho}d\right) = \rho_{eg}d_{ge} + \rho_{ge}d_{eg}. \tag{104}$$

The expressions from Section 3.1.1 for the matrix elements of the density matrix and the expression for the electric field, gives

$$P = -\frac{2\rho_a|d_{eg}|^2}{\hbar\Gamma}\frac{2\frac{\Delta}{\Gamma} - i}{1 + 4\left(\frac{\Delta}{\Gamma}\right)^2 + s_0}\frac{A}{2}e^{i\mathbf{k}\cdot\mathbf{r}-i\omega t} + c.c. \tag{105}$$

Comparing (105) with (102), it can be seen that the susceptibility takes the form

$$\chi = -\frac{2\rho_a|d_{eg}|^2}{\hbar\epsilon_0\Gamma}\frac{2\frac{\Delta}{\Gamma} - i}{1 + 4\left(\frac{\Delta}{\Gamma}\right)^2 + s_0}. \tag{106}$$

This is often called the non-linear susceptibility [66] as it has a dependence on the field intensity through the variable s_0. The single atom response which is encompassed in the polarizabilty, mentioned earlier in Section 3.2.1, is related to the susceptibility by $\epsilon_0 \chi = \rho_a \alpha$ [4]. The factor $\frac{2|d_{eg}|^2}{\hbar \epsilon_0 \Gamma}$ is proportional to the total light scattering cross section of the atom and we generalize it for multilevel structure by $\frac{2|d_{eg}|^2}{\hbar \epsilon_0 \Gamma} \to \sigma_0/k_a$, where

$$\sigma_0 = \frac{2F'+1}{2F+1} \frac{\lambda^2}{2\pi}. \tag{107}$$

Therefore we write the complex susceptibility as

$$\chi = -\frac{\sigma_0 \rho_a}{k_a} \frac{2\frac{\Delta}{\Gamma} - i}{1 + 4\left(\frac{\Delta}{\Gamma}\right)^2 + s_0}. \tag{108}$$

The expression for χ shows that the two-level system is saturable as relation to the index of refraction $n = n_r + in_i \simeq 1 + \frac{1}{2}\chi$ gives an absorption coefficient that falls off with increasing electric field intensity [42, 66]

$$\kappa = k_a n_i = \frac{\sigma_0 \rho_a}{1 + 4\left(\frac{\Delta}{\Gamma}\right)^2 + s_0}. \tag{109}$$

We have a basic, but solid description of how the medium responds to an applied electric field and what it left to do is explain how the electric field varies within the medium. Using Maxwell's equations, the wave equation for the electric field is

$$\left(\nabla^2 - \frac{1}{c^2}\frac{\partial^2}{\partial t^2}\right)E = \mu_0 \frac{\partial^2 P}{\partial t^2}. \tag{110}$$

The electric field and electric polarization both have positive and negative frequency components with amplitudes that vary slowly in time and space (equations (67) and (102)). While these assumptions were made somewhat out of convenience for calculation purposes, in reality they are a good approximation as to what happens to the beam as it propagates. If the laser beam is not focused too tightly, then it can be expected to vary minimally in the direction of propagation [66] and, as in experiment, the system will be probed in steady state such that the amplitude change in time will be small when compared to the laser frequency ω. With these two ideas in mind, the slowly-varying envelope approximation can be applied to (110) resulting in

$$\frac{\partial A}{\partial z} = \frac{i}{2k}\nabla_T^2 A + \frac{i}{2kn_0^2}\chi A, \tag{111}$$

sometimes called the *non-linear Schrodinger equation* (NLSE) [66, 106]. Here, ∇_T^2 is the transverse (x-y) Laplacian and n_0 is the linear index of refraction,

$$n_0 = 1 - \frac{\sigma_0 \rho_a}{k_a} \frac{\frac{\Delta}{\Gamma}}{1 + 4\left(\frac{\Delta}{\Gamma}\right)^2}. \tag{112}$$

For densities not too high, $n_0 \sim 1$.

To solve (111) exactly is impossible due to the non-linear dependence on the field intensity through the susceptibility. However, numerical techniques do exist that can handle (111). One method in particular is quite straightforward and it is known as the *beam propagation method* or *split-step method* [106]. In the split-step method, the beam is propagated forward in discrete steps through free space and non-linear corrections, due to the presence of the sample, are made between each one. This method is limited to calculating the beam profile in the forward direction, but it serves well for its intended purposes.

The algorithm can be implemented as follows: The NLSE is grouped into linear and non-linear terms,

$$\frac{\partial A}{\partial z} = \left\{ \hat{L} + \hat{N} \right\} A, \tag{113}$$

where $\hat{L} \equiv \frac{i}{2k} \nabla_T^2$ and $\hat{N} \equiv \frac{i}{2k} \chi$. Integrating (113) formally between z and δz gives,

$$A(z + \delta z) = \exp \left\{ \delta z \hat{L} + \int_z^{z+\delta z} \hat{N} dz \right\} A(z). \tag{114}$$

The trapezoidal rule can be used to estimate the integral containing the non-linear term,

$$\int_z^{z+\delta z} \hat{N} \simeq \frac{z + \delta z}{2} \left[\hat{N}(z + \delta z) + \hat{N}(z) \right]. \tag{115}$$

The exponential expression in (114) can be approximated by [106]

$$\exp \left\{ \delta z \hat{L} + \int \hat{N} dz \right\} \simeq \exp \left(\frac{\delta z}{2} \hat{L} \right) \exp \left(\int \hat{N} dz \right) \exp \left(\frac{\delta z}{2} \hat{L} \right) + \mathcal{O} \left(\delta z^3 \right). \tag{116}$$

To apply the linear operator directly to $A(z)$ is difficult and can be handled better through frequency space. Numerically this is done by applying Fourier and inverse Fourier transforms so that

$$A(z + \delta z) =$$
$$\text{FFT}^{-1} \left\{ e^{-i\delta z 2\pi^2 (q_x^2 + q_y^2)} \text{FFT} \left[e^{\int N dz} \text{FFT}^{-1} \left(e^{-i\delta z 2\pi^2 (q_x^2 + q_y^2)} \text{FFT} \left\{ A(z) \right\} \right) \right] \right\}. \tag{117}$$

Here, FFT stands for fast Fourier transform [107]. As the susceptibility will have a spatial dependence through the atomic density ρ_a and s_0, $A(z+\delta z)$ will have to be solved iteratively. This is done by making the approximation that $A(z+\delta z) \simeq A(z)$ in (115) for the first iteration to solve for $A(z + \delta z)$ in (117). In the next iteration, $A(z + \delta z)$ in (115) is updated to the most recent value and a better estimate is obtained for the electric field amplitude. This process converges quickly and it is found that only two iterations are needed to calculate
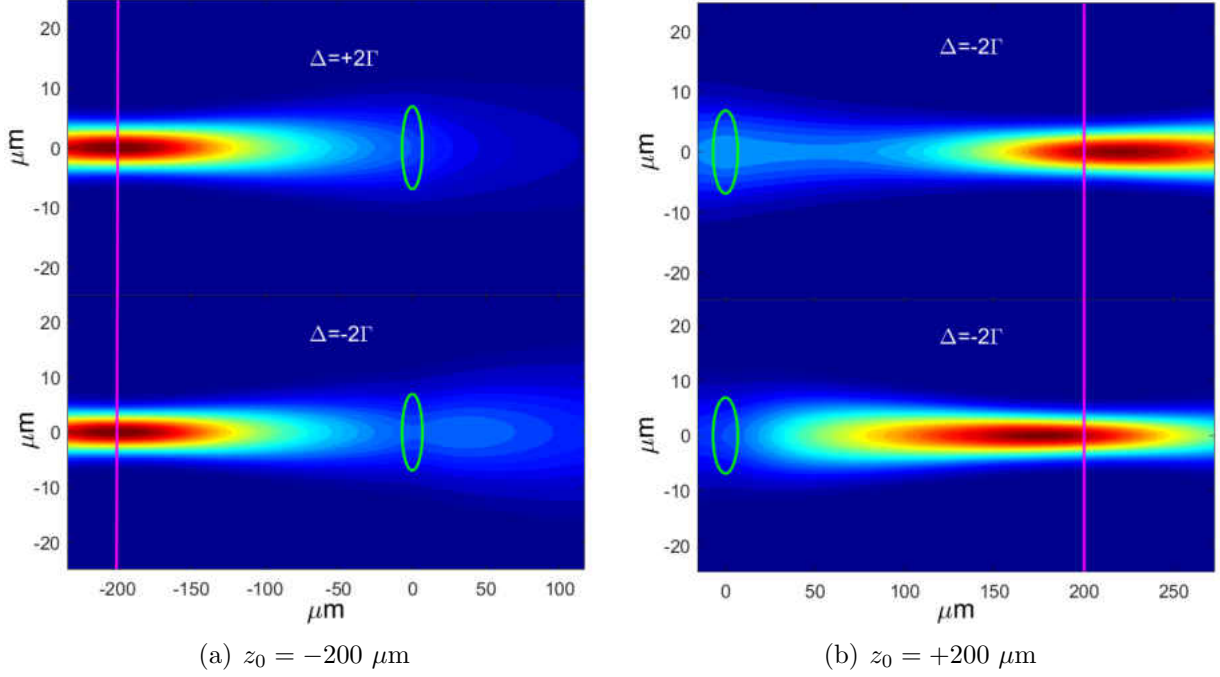
(a) $z_0 = -200 \ \mu$m $\qquad\qquad\qquad\qquad$ (b) $z_0 = +200 \ \mu$m

FIG. 32: Probe focus for (a) $z_0 = -200 \ \mu$m and (b) $z_0 = +200 \ \mu$m. The horizontal axis is the direction of propagation and the vertical axis is aligned along the short axis of the FORT. The intended probe focus is denoted by the vertical purple line and the location of the FORT is indicated by the green circle.

the electric field for $z + \delta z$. To start the initial step, the input electric field is taken as a Gaussian beam [88],

$$A(x, y, z) = A_0 \frac{w_0}{w_z} \exp \left\{ -\frac{x^2 + y^2}{w^2(z)} + ik\frac{x^2 + y^2}{R(z)} - i\xi(z) \right\}, \qquad (118)$$

where $w(z) = w_0 \sqrt{1 + \left(\frac{z - z_0}{z_R}\right)^2}$ is the z-dependent beam waist, $R(z) = (z - z_0)\left[1 + \left(\frac{z_R}{z - z_0}\right)^2\right]$ is the radius of curvature, and $\xi(z) = \tan^{-1}\left[\frac{z - z_0}{z_R}\right]$ is the Gouy phase. Here, z_0 is the focal location. The beam that is transmitted is one whose amplitude is attenuated by the imaginary part of the χ and whose phase is adjusted by the real part.

Results of the simulation are shown in Figs. 32 (a) and (b). The beam is focused to the same spot size as estimated in experiment and is incident on the broad side of the atomic sample. For red detuned light, the sample acts as a positive focal length lens causing the beam to focus. For blue detuned light, it acts as a negative focal length lens and spreads the beam out. Comparison between experiment and simulation can be made by taking the center portion of the simulated beam in the far-field ($\sim 10z_R$) and plotting it along side the
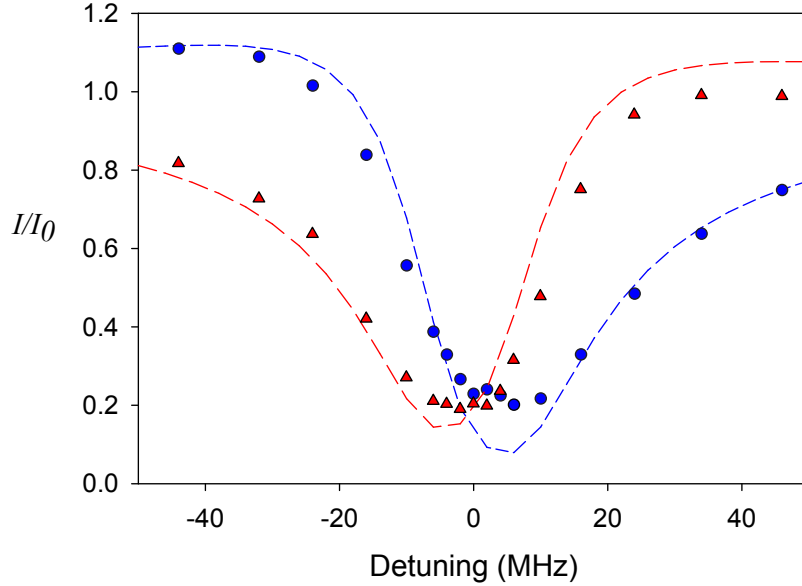
FIG. 33: Comparison between experiment and simulation. Blue curve and blue circles represent $z_0 = -200$ μm. Red curve and red triangles represent $z_0 = +200$ μm.

experimental probe transmission through the aperture. We get very good agreement between experiment and simulation, which suggests that the main cause for the distorted line shapes is due to refraction of the laser beam. It should be noted that our prior experiments [104], although plagued by the lensing effects, consistently showed a broadened spectrum and decreased absorption. Both of these effects could be explained by superradiant scattering in the forward direction, but further investigation was not performed on this experimental setup. The width and cross section determined from that data were 13.2 MHz and 0.04 μm^2 (compared to 0.14 μm^2), respectively, for the density of 2×10^{13} atoms/cm^3 probed in the z-scan experiment. Those values were used in the simulation and were found to help better match it to experiment. Other possible discrepancies could stem from how well the probe focal location is known experimentally and computational limitations in being able to propagate the beam well into the far-field regime.

4.3 SIMPLE LENS MODEL

As mentioned before, the results can be described as a lensing effect [108], but on a much smaller length-scale than has been previously studied. This scale can be estimated by considering beam deflection along the smaller radius of the sample and approximating it as a

ball lens with a focal length given by

$$f = \frac{n_0 r_0}{2(n_0 - 1)},$$

(119)

where r_0 is the radius of the lens and will be taken as $2r_y$ so that it is given in terms of the beam profile definition. The expression for the linear index of refraction (112) will be used with the density taken as constant. Observing the detuning dependence one can see that for $\Delta < 0$, n_0 is greater than 1 leading to a positive focal length and hence a *focusing* effect. Likewise for $\Delta > 0$, n_0 is less than 1 giving a negative focal length or *de-focusing* effect. To give an idea of scale for this ball-type lens, the most acute response occurs for $\Delta = -\Gamma/2$ ($n_0=1.02$) and $\Delta = +\Gamma/2$ ($n_0=0.98$) which corresponds to $f = +176$ μm and $f = -169$ μm, respectively.
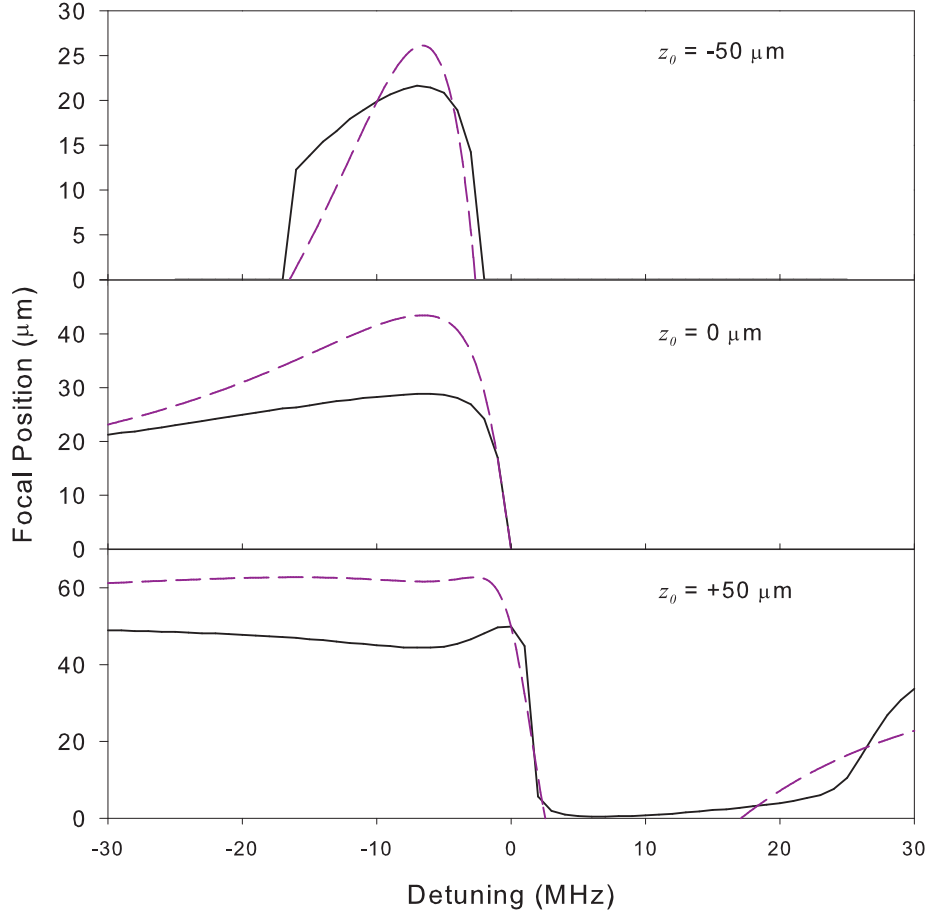
FIG. 34: Comparison between the model (dashed-line) and simulation (solid-line). z_0 is the *intended* focus of the probe beam, but with the presence of the atom sample, the actual focal location is shifted along z.

With an effective focal length for the sample, a focusing distance can be estimated by using ray transfer matrices or the 'ABCD' Law for Gaussian beams [88] which states that

$$\frac{1}{q_2} = \frac{C + D(1/q_1)}{A + B(1/q_1)} \tag{120}$$

where A,B,C, and D are the elements for the transfer matrix and $q(z)$ is the complex beam parameter given by

$$\frac{1}{q(z)} = \frac{1}{R(z)} - i\frac{\lambda}{\pi w^2(z)}. \tag{121}$$

The transfer matrix can be constructed as a combination of a thin lens with focal length given by (119) followed by a free-space propagation of length z,

$$\mathbf{T} = \begin{pmatrix} 1 - \frac{z}{f} & z \\ \frac{-1}{f} & 1 \end{pmatrix}. \tag{122}$$

Solving for the minimum waist results in a focusing location of

$$z' = \frac{(1 - \frac{f}{R(-z_0)})f}{(1 - \frac{f}{R(-z_0)})^2 + (\frac{f}{z_R'})^2}, \tag{123}$$

where $z_R' = \pi w^2(-z_0)/\lambda$ and z_0 is the intended probe focal location. This approach works well when the incident beam is comparable to or less than the size of the sample. Once the beam exceeds the dimensions of the sample, geometrical optics no longer applies as diffraction makes a significant contribution to the propagated beam.

Using the above model and simulation, it becomes clear why the data takes the form it does in Fig. 31. For an intended probe focus before the sample z_0, only the low frequency side of resonance affects the actual probe focus z' by converging the beam after it passes through the sample (Fig. 34). The high frequency side of resonance, due to having an index-of-refraction less than one, only serves to spread the beam out. This gives an absorption profile lower on the blue side than the red. However, once z_0 is sufficiently greater than zero, the red side of resonance will cause the probe beam to focus prematurely while the blue-side extends the focal location giving the illusion of more absorption for $-\Delta$. We may then consider the atomic sample as a microscopic lens as the probe beam can be caused to focus on a micron-length scale.

The above experiment and analysis, while not based on cooperative effects, gives some insight on the difficulty of interpreting measurements on atom-light interactions. Standard classical optics can, in a sense, become parasitic in nature when the underlying microscopic workings are desired. Nonetheless, the lensing experiment provided valuable insight into the

original forward scattering experiments and help lay the ground work for the superradiant experiments with regards to a proper optical setup.

CHAPTER 5

EXPERIMENTAL ARRANGEMENT

The requirements for our experiment to be able to measure single photon superradiance and the cooperative Lamb shift can be categorized into a few areas:

- **Fast laser beam shut-off** The lifetime for ^{87}Rb is $\sim$ 26 ns which is close to the response time of a standard AOM. To shorten the switching time, so that faster, supperadiant emission can be observed, requires more state of the art equipment.

- **Photodetection** Atom fluorescence can be measured a variety of ways, but when the detected signal is fast and of low light intensity, photon counting techniques must be applied.

- **Blocking the incident probe beam** A long time problem with superradiance of any sort is the parasitic effect of reducing the amount of incident light compared to scattered light in the forward direction. There are ways of measuring off-axis superradiant light [35], but for direct comparison with the ideal timed-Dicke state case, the forward directed light is needed.

- **More efficient duty cycle** In our previous experiments the duty cycle of the experiment (the time interval between creation of one atomic sample to the next) was around 6 s which involved creating only one dipole trap per realization. When the prospect of only detecting, on average, fractions of a photon per trap cycle due to photon counting, it is seen that the rate at which data is taken must be increased.

We will now address these issues and describe the techniques to handle each one.

5.1 FAST PROBE SHUT-OFF

When a sample is illuminated with an excitation pulse, the resulting detected time dependence of the fluorescence is given by [109],

$$I(t) = P(t) \otimes G(t) \tag{124}$$
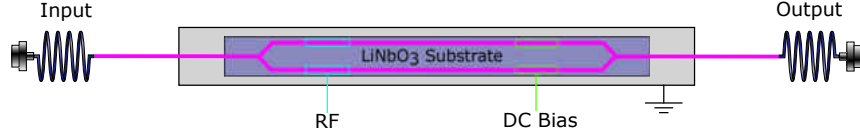
FIG. 35: Basic layout for the LiNbO$_3$ intensity switch.

where $P(t)$ is the response function of the detection system to the excitation pulse, $G(t)$ is the decay law of interest from the sample which is generally single exponential, and $\otimes$ denotes the convolution between the two functions. Provided that the signal level can be observed far enough down in contrast, regardless of the fall time of the excitation pulse, the decay constant can be extracted from the convoluted function $I(t)$ (as the excitation pulse will eventually fall off faster than the exponential). However, in experiment the amount of contrast is limited due to signal-to-noise and there will be some limit as to how fast of a decay can be measured.[1]

The AOM is a typical device used to measure time dependent fluorescence due to its relatively short shut-off (~ 10 ns) compared to most applications. With the decay of ^{87}Rb being on a similar time scale (26 ns), any faster decay from supperadiance would be difficult to measure with good contrast and the decay would essentially blend in with the shut-off of the AOM. To circumvent this we employed the use of a Lithium Niobate (LiNbO$_3$) intensity switch (EOSPACE, AZ-0S5-10-PFU-SFU-780). The LiNbO$_3$ intensity switch acts as a Mach-Zehnder interferometer by splitting the beam into two separate paths that can have their relative phase controlled by the index of refraction of the material. The index of refraction is adjusted by an external RF electric signal and can be used to modulate the intensity output of the switch once the two separate beams are combined. A list of the specifications of our particular switch are included in Table 3.

Just as in any other interferometer the arms must be balanced which can be done through control of a DC bias voltage. The balancing is not perfect as there will still be residual effects from material inhomogeneity, but fluctuations to temperature instability and laser power can be corrected for. In our case, this control voltage is supplied by a home built controller. The circuit diagram is shown in Fig. 36. The circuit is centralized around an

---

[1]Here we speak of obtaining the decay by observing the response $I(t)$ signal on scale where $P(t)$ has significantly fallen off. Usually [109], the contribution of $P(t)$ is handled with a least squares fitting scheme that takes into account the convolution (124) and the separation of I and P is not as critical. What we will see later on with the experimental data is that there is significant leakage light into the detector from the probing pulse which makes least square fitting algorithms less useful, and so fitting relies on observing the decay tail, following sufficient decay of the probe pulse itself.

TABLE 3: Specifications for LiNbO$_3$ switch as quoted by EOSPACE.

Spec	Value
Insertion Loss	2.5 dB
Extinction Ratio	23 dB
Response Time	100 ps
RF V$_\pi$ @ 1 GHz	2.3 V
Input/Output Fiber	1 m long, 5 μm PANDA
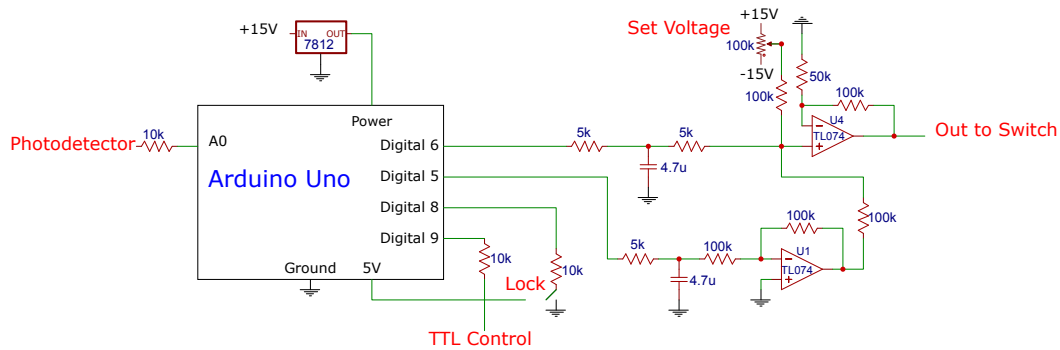
FIG. 36: Circuit diagram for the dc bias control for the LiNbO$_3$ switch. Code for the Arduino microcontroller is included in Appendix D.

Arduino microcontroller which (code in Appendix D) is programmed to correct for power fluctuations detected in a photodetector. Digital output 6 adds positive voltage to the DC input of the switch and digital output 5 adds negative voltage. The correction voltages stem from pulse-width-modulated signals that are integrated to give smooth DC levels. To avoid overdriven oscillations in the output voltage, the photodetector signal is averaged over a coupled hundred ms. The desired operating point can be set with a potentiometer and then locked to that level. A TTL input is also added that temporarily disables the read function with respect to the photodetector when the LiNbO$_3$ switch is modulated. This keeps the circuit from trying to correct for the switch being turned off and on again.

The LiNbO$_3$ modulator can be operated in a variety of modes including non-return-to-zero modulation (NRZ), differential phase shift key modulation (DPSK), amplitude modulation, and pulse modulation [110]. Our specific needs require the latter function which involves driving the switch at the full π voltage. Operating in pulse mode is achieved by tuning the bias voltage such that transmission through the switch is at a minimum and then sending in a fast, large pulse (see Fig. 37 for an example of how the switch varies with bias voltage). Our pulse is generated with a fast voltage comparator (Analog Devices, ADCMP606 Evaluation Board) that has a fall time of approximately 200 ps and an output near 2 V. The comparator, purchased at mouser.com, is meant to be used in differential output mode. However, we were able to use it in a single ended configuration and it provided satisfactory pulse shapes with proper snubbing (Fig. 38). The output of the comparator is sent through a variable attenuator (Kay Elemetrics, 1/839 Attenuator), and amplified by a pulse amplifier (Mini-Circuits, ZPUL-30P \$300) with 35 dB gain and 1 ns response time. Normally LiNbO$_3$ switches are driven with RF driver modules that are seeded with ultrafast pulse generators (< 30 ps response time). This equipment would be ideal for creating the fast pulses needed to observe superradiance, but are quite costly. Since the transit time jitter of the PMT used to detect the signals is very near 1 ns, and fundamentally limits the timing resolution of the experiment, the comparator and Mini-circuits amplifier were sufficient.

The fast pulse is delivered to the vacuum chamber using the setup in Fig. 39. A second slave laser (the probe laser) powered by a SRS diode driver is injected with light from the DFB slave laser (Fig. 13). The probe beam is sent through an AOM operating at $f = 75$ MHz and the -1st order beam is taken. To monitor the stability of this laser and ensure that it is following the seeding light, the zeroth order beam is picked off and sent to a spectrum analyzer (Thorlabs, SA200-7A). The -1st order beam is sent through another AOM with $f = 160$ MHz. The -1st order beam from this AOM, which is now near the $F = 2 \rightarrow F' = 2$ transition, is used as the optical pumping light for the atom number determination method (Section 3.1.3). The $+1$st order is on resonance with the $F = 2 \rightarrow F' = 3$ transition and is sent to the LiNbO$_3$ switch. The third role of this AOM is to further extinguish the probe beam once the intensity switch has pulsed. Usually, the AOM is allowed to turn on ~ 15ns before the switch pulse such that light intensity is constant in time and then turned off ~ 15 ns after. Adding the AOM in series ensures that the atoms see no resonant light until the actual probing pulse is sent. Preceding the switch is a linear polarizer which serves to clean the polarization as the switch is quite sensitive to any polarization drift and the extinction is degraded if not properly keyed to the slow axis of the fiber.
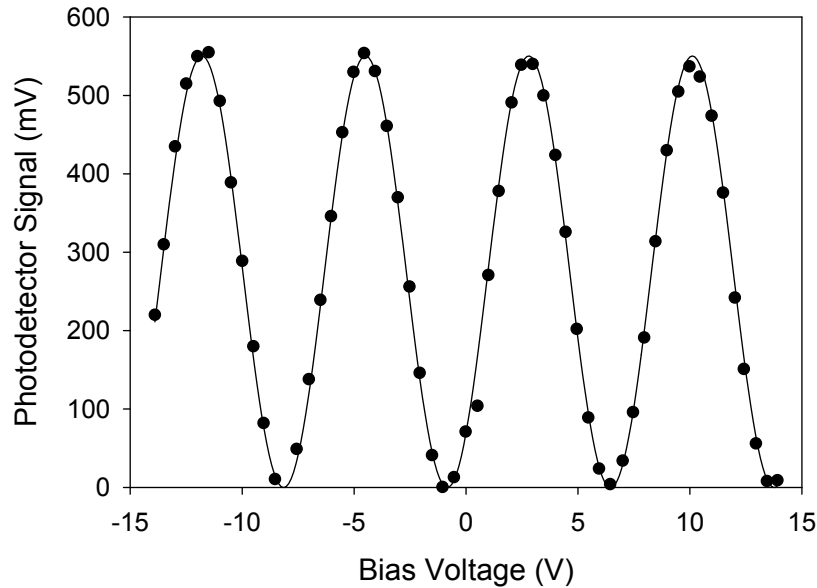
FIG. 37: Intensity switch transmission as a function of DC bias voltage. The dependence varies sinusoidally with bias voltage.
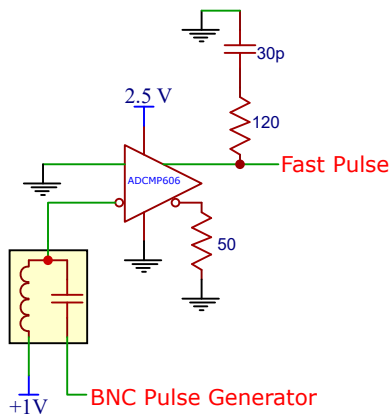
FIG. 38: Comparator circuit used to create a sharp square pulse. A triggering pulse, from an external pulse generator, is sent into a bias-tee to give a positive offset from ground. The comparator is triggered when this NIM level pulse drops below 0 V and the output is taken from the non-complementary side. To reduce ringing on the output, a snubber circuit is added via trial and error with different combinations of capacitors and resistors. It was found that no hysteresis was needed to condition the output signal.
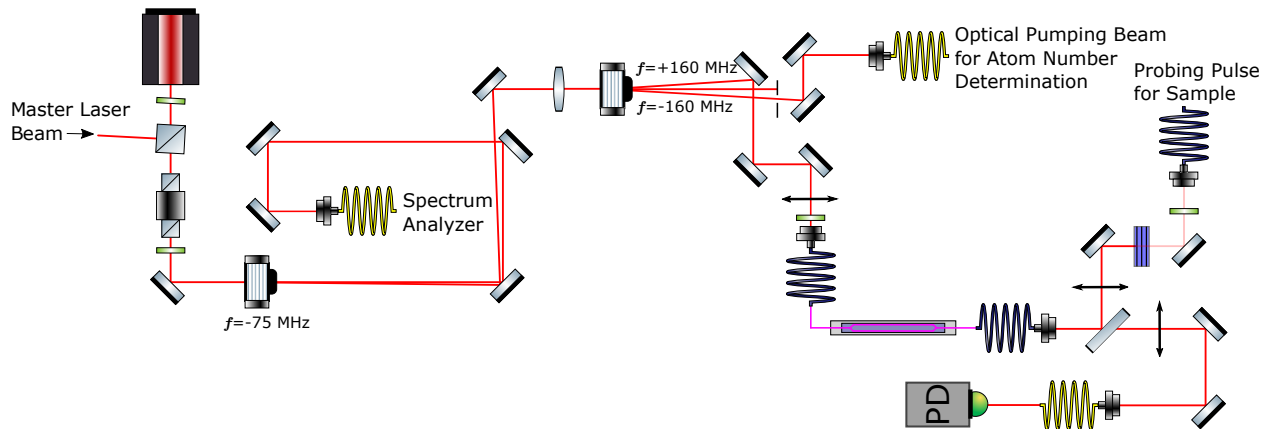
FIG. 39: Optics setup for the probe laser. The 200 MHz AOM is used for better extinction in conjunction with the LiNbO$_3$ switch and for frequency shifting to the $F = 2 \rightarrow F' = 2$ transition for the atom number determination via optical pumping.

It was noticed that the output beam, even when keyed properly on the input, could have some polarization ellipticity which caused issues when the beam was sent to the vacuum chamber table. To overcome this, the beam was passed through a non-polarizing beam splitter with a polarizer in each arm (one path for probing the atoms and the other for biasing control). This cleaned the polarization and as well made the DC bias controller sensitive to these drifts which it could correct for by beam intensity compensation. An attenuator, placed before the beam was sent to the chamber table, provided control over the probing light power.

5.2 TIME CORRELATED SINGLE PHOTON COUNTING

Time correlated single photon counting is a technique for registering individual photon events that relay information on the dynamics of the underlying physics. Typically, the systems of interest are radiative transitions from atoms or molecules where the quantity desired is the intensity decay law followed. With proper equipment this technique can be use to make timing measurements on the order of picoseconds [109]. This fact, along with its sensitivity, makes photon counting a great tool for detecting single photon superradiance.

The process can be pictured as detecting an incident photon with some efficiency on a detector. The photon generates an electron or collection of electrons that are carried to an external circuit where the arrival time is correlated with respect to some start event (usually an electrical signal from a pulse generator). With each detection there is an associated dead

time which limits the system to sensing only one photon event at a time. By repeating this process a great number of iterations, a time dependent function can be developed that is representative of the physical process at hand.
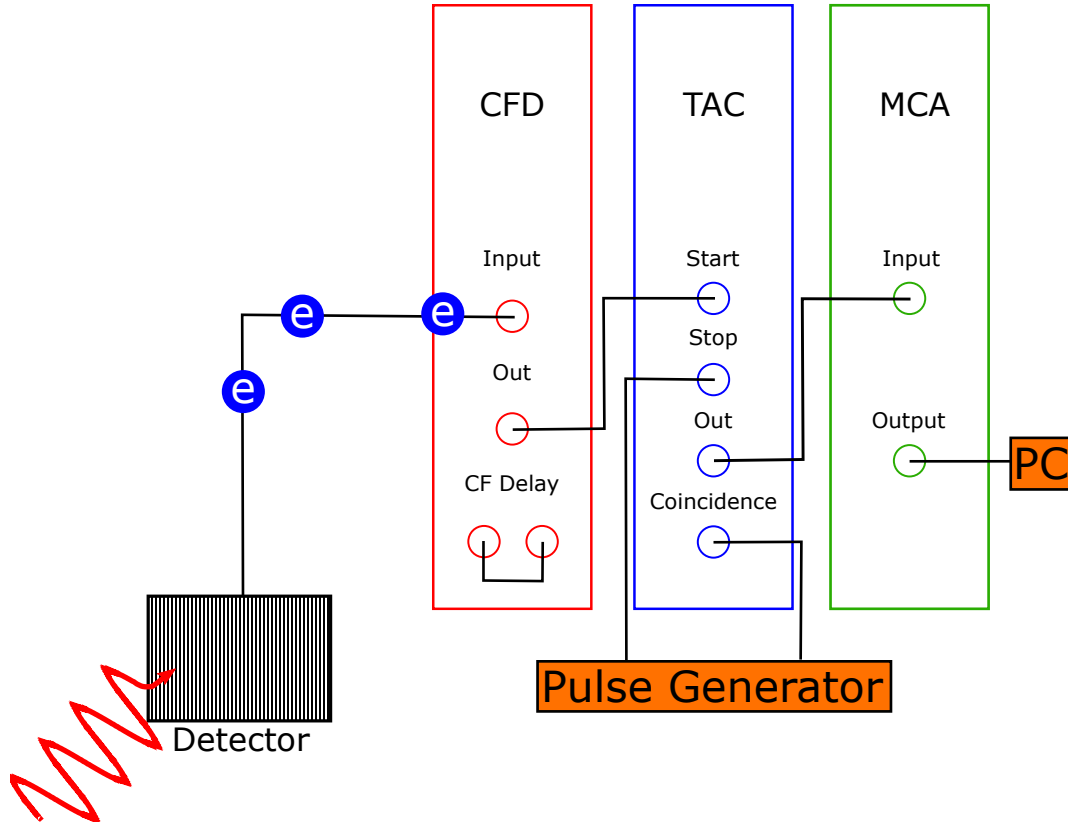
FIG. 40: Setup for time correlated single photon counting. Light incident on a detector emits a charge pulse that is discriminated, compared in time to a pulse generator using a TAC, and counted with a MCA. More details with respect to the overall timing of the experiment will be given in later sections.

Photons are usually detected with a photo multiplier tube (PMT) or avalanche photodiode (APD). APDs are fast devices (down to 10's of picoseconds transit time jitter) and have high quantum efficiencies in the infrared, but require many stages of amplification. PMTs have very high gain with moderate timing resolution if chosen properly, but suffer from low quantum efficiency in the infrared. In our setup we have a Hamamatsu 9110P PMT built specifically for photon counting due to its low dark-count rate (500 s^{-1}) and extremely high gain (10^8). With such high gain we find that it is not necessary to amplify the output signal which is advantageous in terms of reducing noise and electronic pick-up. The transit time jitter is 1.2 ns and fundamentally limits the timing resolution in the experiment.

The individual photons can be counted and binned using a time-to-amplitude converter (TAC) and a multi-channel analyzer (MCA). The TAC (Tennelec, TC862) operates by converting the difference in time between two input pulses into a pulse of constant width but varying height; the two inputs are appropriately called the start and stop pulses. This height is recorded by the MCA (Ortec, EASY-MCA-2k) which bins it into a histogram plot. The timing calibration between the TAC and MCA is carried out by taking the PMT signal generated by background light and splitting it into two lines, delaying one, and using the advanced signal as the start pulse for the TAC and the delayed one as the stop pulse. A delay line box (Ortec, DB463) is used for this purpose, and the observed signal on the MCA can be recorded in time as the set delay. The calibrated time resolution is a combination of the TAC time range settings and the number of bins used in the MCA. Typically, the time range chosen is 250 ns over 512 bins giving a calibrated value of $\Delta t = .522(1)$ ns.

As stated above, the PMT pulses are timed relative to an external source such as a triggerable pulse generator. The natural setup for this is to assume that the external source sends a start pulse to the TAC and some time later the PMT pulse is received which can be binned accordingly. However, because the detection of photon signals is random in nature there will be some cases in which the TAC receives the start pulse and no stop pulse from the PMT arrives. This is problematic as this type of event increases the recovery time of the TAC and hence leaves it inactive for the next round of measurements. If the experiment is being operated on a fast duty cycle then signals will be lost. A clever work around [109] is to use the PMT signal as the start pulse and the external source as the stop pulse. In this way, the user is never penalized for not reading a photon and the TAC is ready for operation on the next event cycle. The only adverse effect produced is to make the measured response appear backwards in time on the MCA, but this is easily fixed in post-processing procedures.

Not all counts transfered to the TAC will be of interest as there will some contribution due to thermionic emission of the PMT photocathode or other sources. To block this signal a constant fraction discriminator (Ortec, 584) is placed before the TAC. The CFD will trigger off a PMT pulse for a given level and generate an output pulse with fixed width and height. This pulse is then sent to the start input of the TAC. The discriminator level is chosen by empirically changing the threshold setting until a satisfactory level of background noise is acquired over a certain time range. In addition, the use of a CFD helps guard against time walk from the PMT. Time walk occurs because the distribution of pulses coming from the PMT will vary in height and this causes the time at which they are detected to move around (as the slope of the pulse once it passes the trigger level is more steep for some than others).
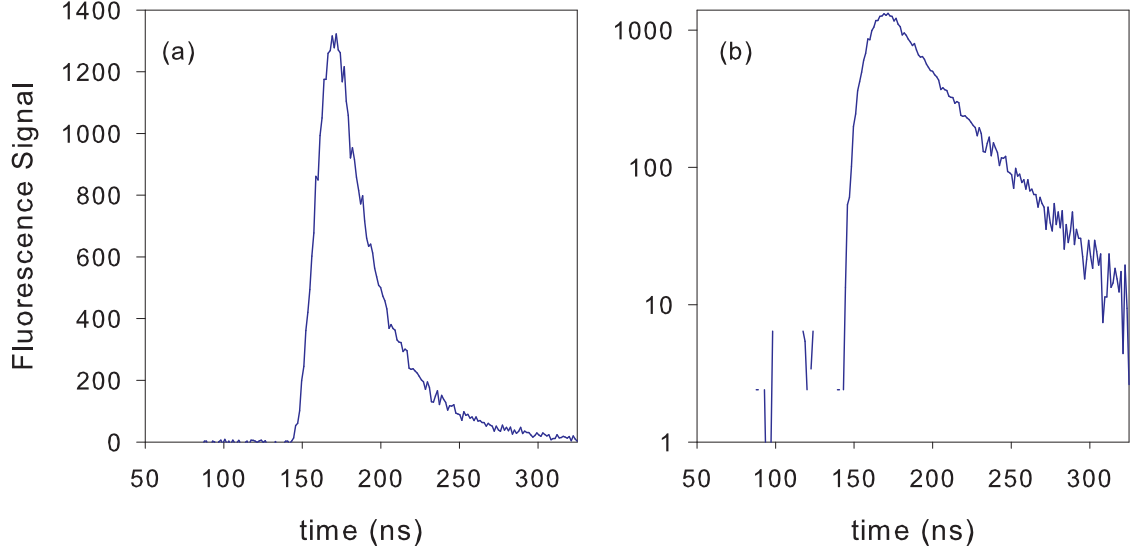
FIG. 41: Fluorescence decay from the FORT obtained by photon counting at 90° to the incident probe beam on a linear scale (a) and on a log scale (b). At long times the decay is mostly single exponential with some distortion due to imperfect background subtraction.

The CFD corrects for this by only triggering at a certain "fraction" of the peak of an input pulse. Therefore, all pulses are timed with respect to the same point in their rise time. A signal obtained from photon counting is displayed in Fig. 41. The temporal shape is a combination of the incident probe beam and a single exponential decay given by (124). The light is detected at 90° with respect to the incident beam which scatters off $\sim 10^5$ atoms. For this measurement the time interval is 1.29 ns and the probe frequency is on resonance.

One last concept to discuss about photon counting is the issue of *pulse-pileup*. Pulse-pileup occurs because TCSPC is limited to detecting one photon at a time and for stronger light signals there will be a tendency to count more photons on the leading edge of the signal. This leads to measured responses such as that in Fig. 42. This can be corrected for by using the formula [109],

$$N_A = \frac{N_i}{1 - \frac{1}{N_E} \sum_{j=1}^{i-1} N_j} \tag{125}$$

where N_i is the observed counts in channel i, N_E is the number of excitation cycles, and N_A is the corrected number of counts for channel i. In our time resolved measurements the pulse duration is very short and the count rate ($\sum_j N_j/N_E$) is less than 5% over the whole course of a data taking run. Because of this, and the fact that our experiment does not seek
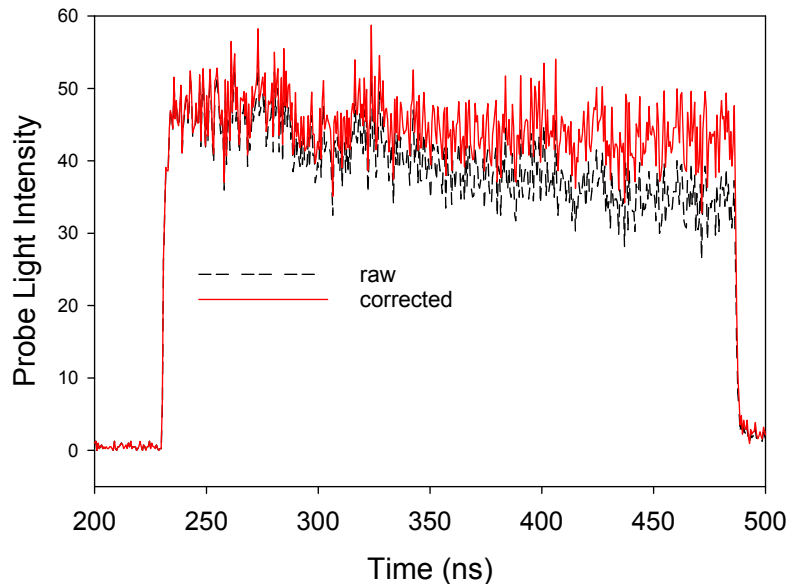
FIG. 42: Example of pulse-pileup correction. The signal comes from stray laser light detected by the PMT. For earlier times there is not much difference between the raw signal and the corrected one. At larger times, however, the effect is more pronounced and must be addressed.

to make a precision measurement [111], we do not perform pulse-pileup correction for the time-resolved data with regards to a short pulse excitation. This is not the case for a longer probe pulse where the distortion builds up over time and is one of the reasons we avoid using TCSPC when investigating the scattered light in the steady state regime of the atoms.

5.3 EXPERIMENTAL GEOMETRY

Observing fluorescence in the forward direction presents a challenging task as the signal propagation direction coincides with that of the incident beam. This means any observed signal would be dominated by un-scattered laser light and runs the risk of saturating the PMT. There are instruments capable of filtering out the more intense laser light [112] that rely on the photorefractive effect in which the laser beam is deflected away from the exact forward direction. However, no material has been developed for the low intensities used in typical cold atom, light scattering experiments. In addition, polarization analyzer arrangements prove useless when the scattered light has the same polarization as the incident beam.

The key to suppressing the laser light is knowledge of how the sample emits the scattered light. Referring to Sections 2.3 and 2.5, the light emitted in the timed-Dicke state will have the form

$$\langle I(\mathbf{r}_s, t) \rangle = \frac{\hbar \omega_a \Gamma}{8\pi r_s^2} \frac{|\beta_+(t)|^2}{N} \left| \sum_j e^{i(\mathbf{k}_0 - \mathbf{k}_s) \cdot \mathbf{r}_j} \right|^2. \tag{126}$$

Taking the distribution of atoms to the continuous limit [60], the summation term can be written as

$$\frac{1}{N} \left| \sum_j e^{i(\mathbf{k}_0 - \mathbf{k}_s) \cdot \mathbf{r}_j} \right|^2 = 1 + \frac{N-1}{(2\pi)^3 r_0^4 z_0^2} \left| \int d\mathbf{r} \, e^{-(x^2 + y^2)/2r_0^2 - z^2/2z_0^2} e^{i(\mathbf{k}_0 - \mathbf{k}_s) \cdot \mathbf{r}} \right|^2$$

$$\simeq 1 + (N-1) \exp \left\{ -\sigma^2 \left[\eta^2 (\cos\theta - 1)^2 + \sin^2\theta \right] \right\} \tag{127}$$

where the approximation comes from assuming that $k_0/k_s \simeq 1$, $\sigma = r_0 k_s$, $\eta = z_0/r_0$, and θ is the scattering angle with respect to the long axis of the sample. This gives an analytical solution to the spatial distribution of the scattered light in the coupled dipole model. The presence of 1 in the first term signifies there is a incoherent piece of the signal that reduces to isotropic scattering in the low number limit [113]. For sample geometries that keep an elongated aspect ratio but are physically smaller, (127) is broader as function of θ meaning the light is scattered over a greater angular range. If one intentionally *mode-mismatched* the external field with respect to the emitted light, it should be possible that, given a far enough distance away from the sample, the laser light could be spatially discriminated against with respect to the scattered intensity.

The sample used in experiment has dimensions $r_0 = 2.7(1)$ μm and $z_0 = 156(7)$ μm. This corresponds to a full angle of 0.12 radians using (127) and approximately 1 cm radius spot at the observation window for our chamber geometry. To be able to block the probe and collect a significant amount of fluorescence, the Gaussian radius of the laser beam must be well within the cone of emission. Ideally this could be accomplished with a nearly collimated laser beam with a small radius as in Fig. 43. Here the collimated beam is incident on the sample and far down stream is occluded with a block that allows the emitted light to pass around. Of course there will be some leakage due to diffraction but with a small enough beam and a large enough block, this can be minimized. The scattered light could then be collected in a standard $2f - 2f$ lens configuration onto a detector.

To implement the above setup is somewhat complicated due to the limitation of accessible window ports on our vacuum chamber. The only viable option is to come in either with the direction of the dipole trap laser or in the opposite direction (Fig. 22). Coming in the
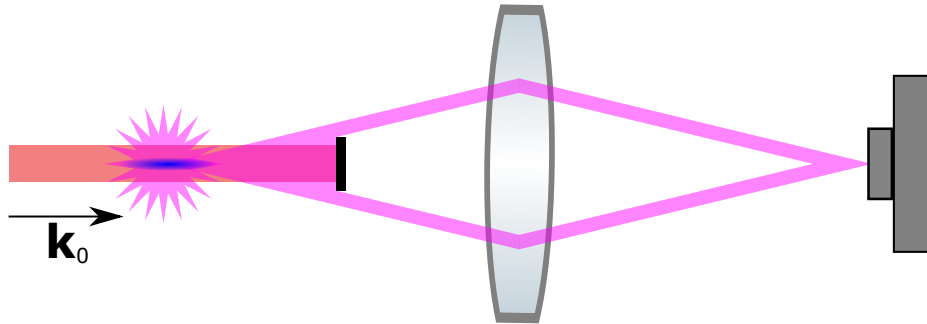
FIG. 43: Possible arrangement for light detection of the forward emitted light.

opposite direction is cumbersome as that requires being able to collect the scattered light through many 1064 nm optics, meaning there would be much optical loss for the 780 nm light. The best option, then, is coupling in the probe beam with the 1064 nm beam splitter and sending it in parallel with the dipole trap laser. There will be some loss for the probe beam, but that is better handled than the emitted light which is the quantity of interest. To accomplish this requires shaping the probe beam to match the lens setup of the dipole trap laser which cannot be moved due to the sensitivity in keeping the trap laser and MOT overlapped with one another.

The optics setup used is displayed in Fig. 44. To be able to use the dipole trap laser optics to collimate the excitation light, the output beam must be adjusted to focus 100 mm before the last positive focal length lens. The calculated collimated beam radius for this setup is 670 μm. Using the CCD to image the beam we estimate the horizontal and vertical radii to be 505 μm and 637 μm, respectively. We take the average of the radii, 570 μm, as the actual radius of the probe beam. Alignment of the dipole trap and probe beam is performed by picking two points of reference on either side of the chamber and walking the probe beam until it passes through both points. It also checked that a fluorescence image of the FORT can be seen at 90° with respect to the direction of incidence by scattering the probe beam off the atoms.

In practice, blocking the unscattered probe beam is made difficult by spurious reflections of the 780 nm light off the 1064 nm optics which have $\sim 15\%$ reflection per surface. This causes off-axis probe light to mix with the atomic emitted light and dominates the detected signal. By chance, most of the off-axis light spreads out further than the coherence cone of the forward emission. We therefore insert an iris that blocks this light but still allows most of the fluorescence through. It is found that a small strip of metal blocks a large
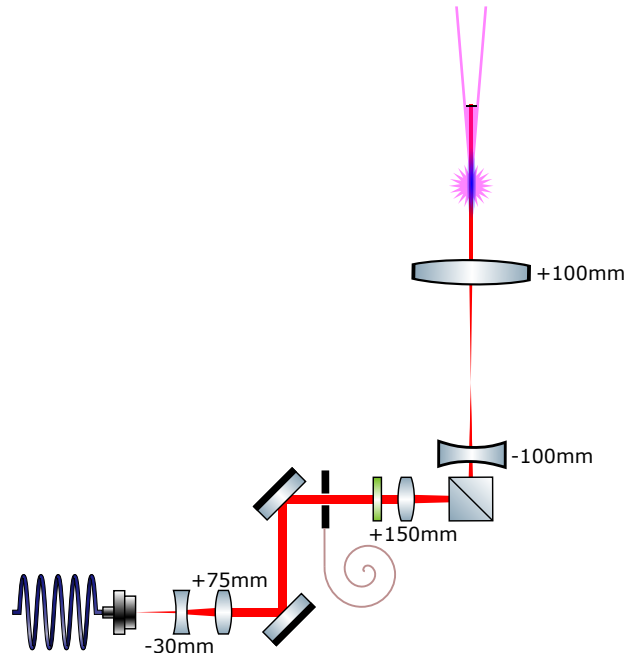
FIG. 44: Optical setup for exciting the atomic sample with the probe beam.

portion of the on-axis probe beam such that the forward emission can be observed. A CCD image of the forward emission is shown in Fig. 46. We determine where the forward emitted light should appear by taking a fluorescence picture of the FORT by flashing the MOT and repumper beams. Then using that location as the region of interest, we flash only the probe beam and look for scattering off the FORT. There is obviously some image aberration but we successfully observe the forward emission. The images can be seen in single shot runs indicating the directional strength of the scattering.
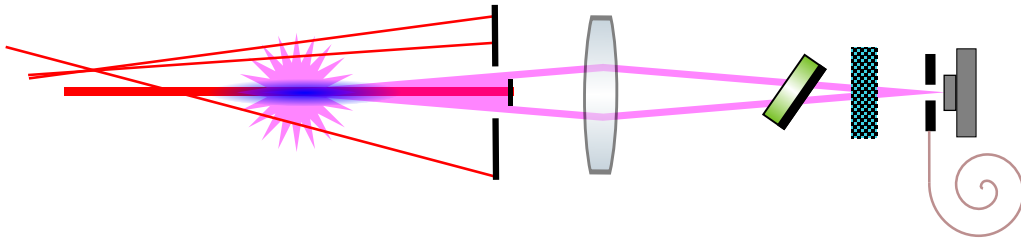
FIG. 45: An iris is inserted to block the reflections of the 780 nm beam off the 1064 nm optics. In addition to the dichroic mirror, an interference filter at 780 nm is placed to block the dipole trap laser from getting into the detector. A shutter is placed before the detector (either the PMT or CCD) to reduce background light detection during periods of no data collection.

(a)   (b)
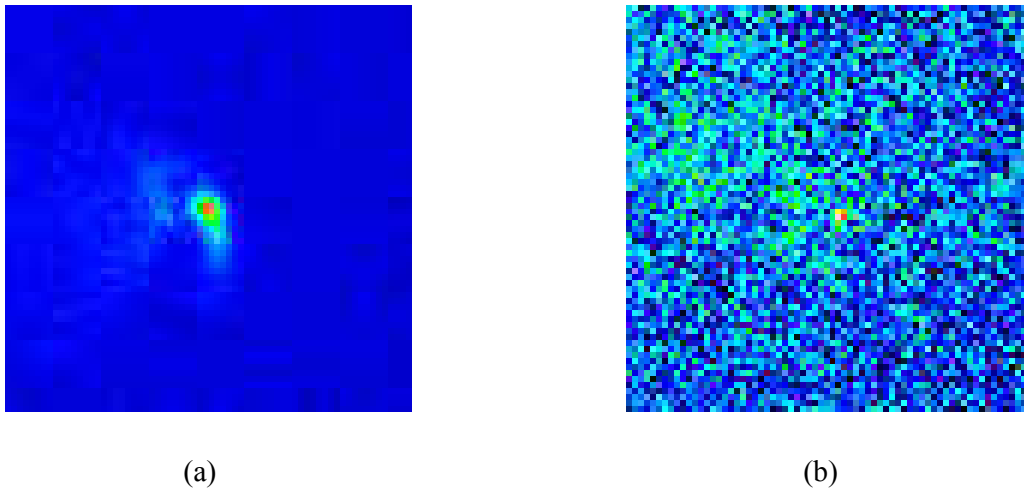
FIG. 46: CCD image in the longitudinal direction of the FORT by (a) flashing the MOT and repumper beams and (b) scattering the probe beam off the FORT.

5.4 MORE EFFICIENT DUTY CYCLE

In most dipole trap timing series there is a period of MOT growth, trap loading, thermalization, and actual trap interrogation. The timing series can be quite long and in our case is about 6 s. This means that for a detection scheme that is built around TCSPC, no more than one photon can be detected every 6 s. On top of that, under normal (correct) operation, there is a small chance that one photon is even detected in a single cycle. It can be seen then that to build up a few thousand total counts, it would take an enormously long time and this all due to the extremely slow duty cycle of building a FORT. What would be helpful is a way to build the FORT, release the atoms, probe them, and then quickly re-trap them. Fortunately this technique has been applied before [11, 114], and is what we use to increase the rate at which we take data.

We implement this dipole trap pulsing technique by allowing the sample to thermalize in the $F = 1$ ground state after which the trap beam is turned off for 10 μs while the atoms are pumped to the $F = 2$ ground state. Once there, the dipole trap is turned back on for an additional 10 μs and the pulsing sequence begins (Fig. 47). A single cycle has a period of 10 μs itself, where for 0.5 μs the dipole trap laser is shut off. This slot is set aside for the actual probing of the sample and enough time is alloted after the dipole trap is shut off and before it is turned on, for the atoms to be probed without any light shift present. To align the dipole trap and probe pulse in time, we use two separate photodetectors to capture their relative location. This is presented in Fig. 48 on a normalized scale along with the *coincidence* and stop pulse which are used for timing the TAC read operation.

To ensure there were no adverse effects from pulsing the FORT[2], we characterized the sample's temperature and atom number as a function of the number of pulses. This is important as the atoms being retrapped will be in the $F = 2$ ground state manifold which has a higher collisional cross section. We found that there was no significant atom loss for a couple hundred pulse cycles ($< 5\%$, see Fig. 49) and that the sample returned to its same size when imaging it on a CCD camera. For the experiment we limit ourselves to 300 pulses. The temperature, in fact, was observed to decrease for an increasing number of pulses. This would suggest, along with the trap loss versus time, that some form of evaporative cooling was taking place. We did not investigate this effect further, but it would be an interesting

---

[2]In this system the atoms are subjected to a square wave modulation of the trap depth. This is similar to what was presented in Section 3.2.3 with regards to the Mathieu equation. However, with the square wave modulation (also known as *Meisser's equation*) the equation is exactly solvable. For frequencies much higher than the natural frequency of the trap, there should be no resonances encountered.
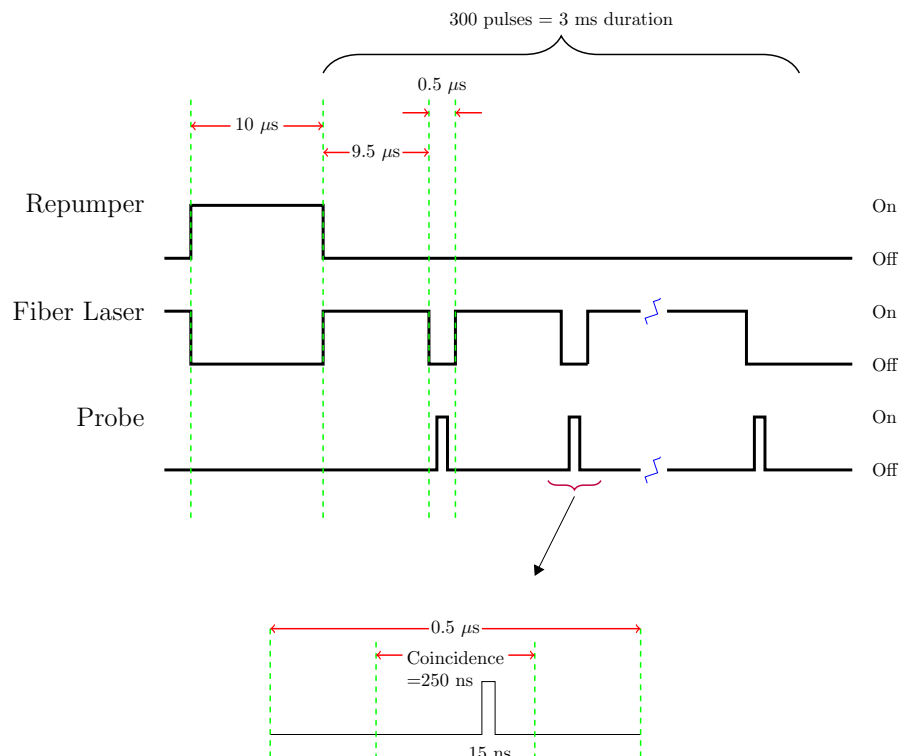
FIG. 47: Timing of the pulsing sequence. Due to constraints with availability of timing channels, the probe pulse has to be set towards the back end of the coincidence.
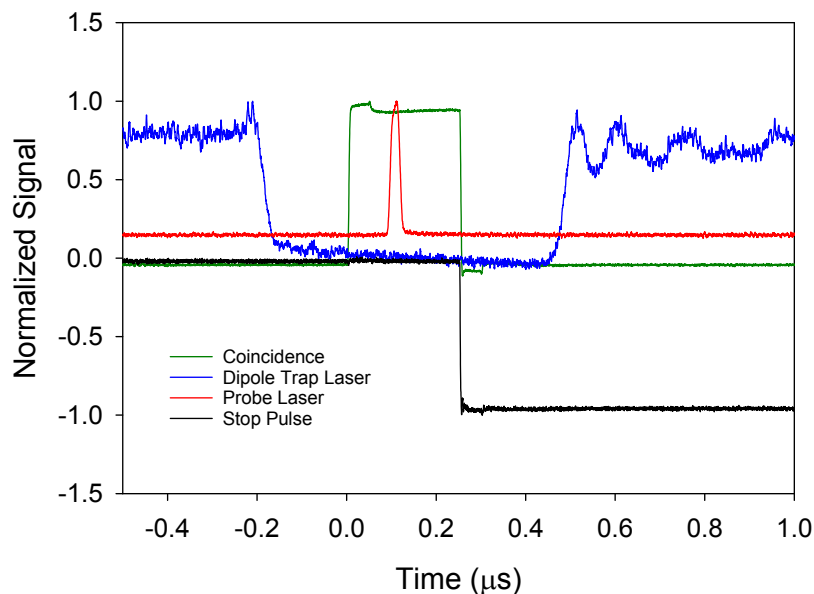
FIG. 48: Scope traces of the switching pulses for the dipole trap, probe beam, TAC coincidence, and TAC stop. The alignment of these four are important for correct detection of scattered light off the sample when the trapping beam is off.
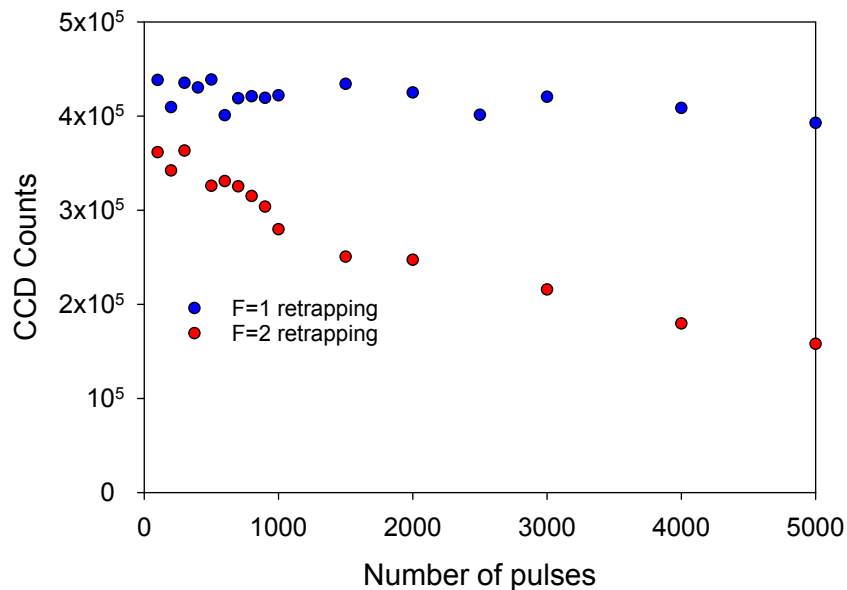
FIG. 49: Atom loss as a function of the number of pulse cycles obtained from fluorescence imaging with the CCD. Results are presented for the $F = 1$ and $F = 2$ ground states. For the $F = 1$ ground state detection, both the MOT and repumper beams must be flashed to image the atoms while for the $F = 2$, only the MOT beam is flashed. This produces a small offset between the two curves but the interpretation of the data is not affected.

process to study in future work.

5.5 PUTTING IT ALL TOGETHER

The previous four sections covered the challenges of creating the experiment and how each is addressed individually. What is left to explain is how to bring all these aspects into one functioning unit that will work reliably. The cornerstone of this, like many other experiments, is timing. With limitations to only standard electronics and on the time scale that we seek, jitter in the instrumentation becomes an issue; normal timing jitter being on the order of nanoseconds for triggerable devices. This requires careful *daisy-chaining* of the control lines from the center operating platform.

In our case, all operations stem from a computer running Labview connected to a data acquisition card (National Instruments, PCI-DIO-32-HS) with 16 output channels. The channels and their respective control responsibility are listed in Table 4. They are for the most part self-explanatory, but some require further detail. For non-pulse applications,

TABLE 4: NI DAQ channels used and their specific operation.

Channel	Operation
3	MOT Shutter
4	Fiber Laser AOM
5	Trigger for Second Quantum Composer
6	Repumper AOM
7	MOT AOM
8	Probe Frequency
9	Probe AOM
10	Trigger for Digital Level Boxes
11	Probe Shutter
12	Magnetic Field
13	FORT Loading Trigger for Digital Level Boxes
14	Repumper Shutter
15	Trigger for First Quantum Composer

channel 4 controls the simple on/off function for the fiber laser AOM to build the FORT. The same goes for channel 9 which functions to keep the AOM warm while the sample is being prepared. Once the pulsed phase is entered, channel's 4 and 9 give up their control by the switching of the digital level boxes by channel 10. The digital level boxes (DLB) [115, 1] are centered around analog switching chips (Maxim, DG419) that allow one input voltage to pass through for a low-level logic control and another input voltage to pass through for a high-level logic control. These boxes are used for tuning the repumper intensity, MOT laser detuning for MOT and FORT loading, probe detuning, and allowing the passage of the pulse sequence to the probe and fiber laser AOMs. The DLB's can be stacked in series to give multiple logic options and we provide one of the schematics below as a reference.

Once all DLB's have switched over, channel 15 from the DAQ triggers an external pulse generator (Quantum Composer, 9614); we will call this QC1. QC1 is set to function on a 10 μs duty cycle running on a burst mode off 300 iterations. Channel 1 on QC1 is used to control the on/off pulse of the dipole trap which is on for 9.5 μs beginning on the leading edge of the cycle. Channel 2 from QC1 is delayed 9.5 μs from ch. 1 and triggers another pulse generator (Standford Research Systems, DG535) that we label as SRSPG. The SRSPG has a total of 9 output channels labeled T0, A, B, AB, $\overline{AB}$, C, D, CD, and $\overline{CD}$. Channel A runs proceeds channel B in time by 250 ns such that ch. AB can produce a TTL pulse to send to the TAC as a coincidence signal. Channel B is delayed from the trigger pulse from
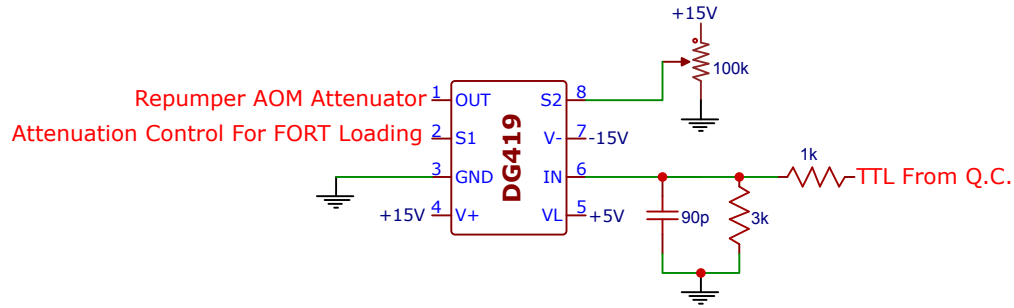
FIG. 50: Example of one of the DLB's used. This specific circuit is designed for switching between another DLB that controls the normal repumper power during MOT loading and reduced power during FORT loading, and the variable repumper pulse width and power during the atom number selection stage before the pulse cycle begins. There is a small integrator on the input to the control switch (pin 6, "IN") that reduces ringing from the external TTL.

QC1 by 1.15 μs and is a NIM level signal that serves as the stop pulse for the TAC. Channel C is delayed from the QC1 trigger by 268 ns and channel D is delayed from C by 40 ns. This creates a pulse with a 40 ns duration from channel CD that is sent to the probe AOM through the DLB's and overlapped with the LiNbO$_3$ switch pulse. The additional channel T0 is used to trigger a BNC 8020 pulse generator (BNCPG) that sends a variable pulse width signal to the ADCMP606 fast voltage comparator. The BNCPG signal pulse is fast and clean enough that no hysteresis is required for the comparator circuit (see Fig. 38). The delay setting for the BNCPG is kept very low as there was found to be considerable jitter effects at higher delay; presumably stemming from variable warming times in the device's circuit board.

The relative timing between the channels from the SRSPG do not line up at the output of the device because of the latency in sending the signals to different parts of the lab. Ideally, all trigger-able devices would be in close proximity to reduce the effects of latency and other signal distortions from line propagation. However, due to the constraints of the laboratory setup, variable length cables have to be used to trigger different devices. This is why a scope had to be used to line up the different signals in Fig. 48. All cables for the pulsing sequence of the experiment are shielded to reduce pick-up and broadcast between adjacent lines.

Channel 5 from the DAQ is used to trigger a second Quantum Composers pulse generator (QC2) 50 ms prior to the onset of the pulse sequence. The main use of QC2 is in the atom number determination for an experimental run, with the exception being its channel 2 which is used to open the external shutter for the PMT or CCD before a pulse sequence begins. The atom number determination method has two stages, the first being the initial repump of some of the atoms in the $F = 1$ up to the $F = 2$ ground state. To only get a partial fraction of the atoms into the $F = 2$ ground state we reduce the repumper power to $\sim 40\mu$W using the DLB pictured in Fig. 50 with the switch trigger coming from ch. 4 of QC2. The atom number is further selected by using a variable length repump pulse generated by ch. 3 of QC2. This length can vary from 8 μs down to 100 ns. The second stage of the atom number determination method comes from fluorescence obtained from the atoms at the end of the pulse sequence. To get this fluorescence we turn on only the MOT beam (so as to only see $F = 2$ atoms) for a period of 3 ms. During this time, the atoms are pumped very slowly down to the $F = 1$ ground state by inelastic scattering off the $F = 2 \rightarrow F' = 2$ transition. This is not an efficient process, but gives ample signal to be detected by a secondary PMT (Hamamatsu, R636) even at low atom number. The PMT is shielded from all other fluorescence, but the FORT, with a home made shutter triggered off channel 1 of QC2 (see Fig. 51). The shutter is simply constructed from a hard-drive motor with leads connected to the voice coil actuator. Any sufficient drive voltage causes the motor to rotate and reduction of that voltage causes it to rotate back.[3] There is considerable latency for this device and it is why QC2 is triggered so early. The fluorescence is calibrated to atom number using the ratio of it to counts collected on the CCD for a fixed number of atoms (Figs. 52). The CCD count corresponds to a certain atom number determined from before (Section 3.1.3).

A schematic diagram for all the important timing connections is shown in Fig. 53. Any timing jitter, with respect to the data, that could occur from the electronics would be after the signals are sent out from the SRSPG. This is because the lines that go to the LiNbO$_3$ switch and the TAC run in parallel. However, the jitter is estimated to be about 100 ps which is far below the time resolution in experiment.

---

[3]See ref. [116] for a more advanced description of this technique. The homemade shutter was needed for the experiment as we had run out of commercial shutters and shutter drivers. It worked well for its intended purpose and actually had opening and closing times of 1 ms.

FIG. 51: A homemade shutter created with a hard-drive motor. A piece of metal is epoxied to the fins to serve as the light block and is placed directly in front of a multimode fiber used to direct fluorescence to the photocathode of a PMT.
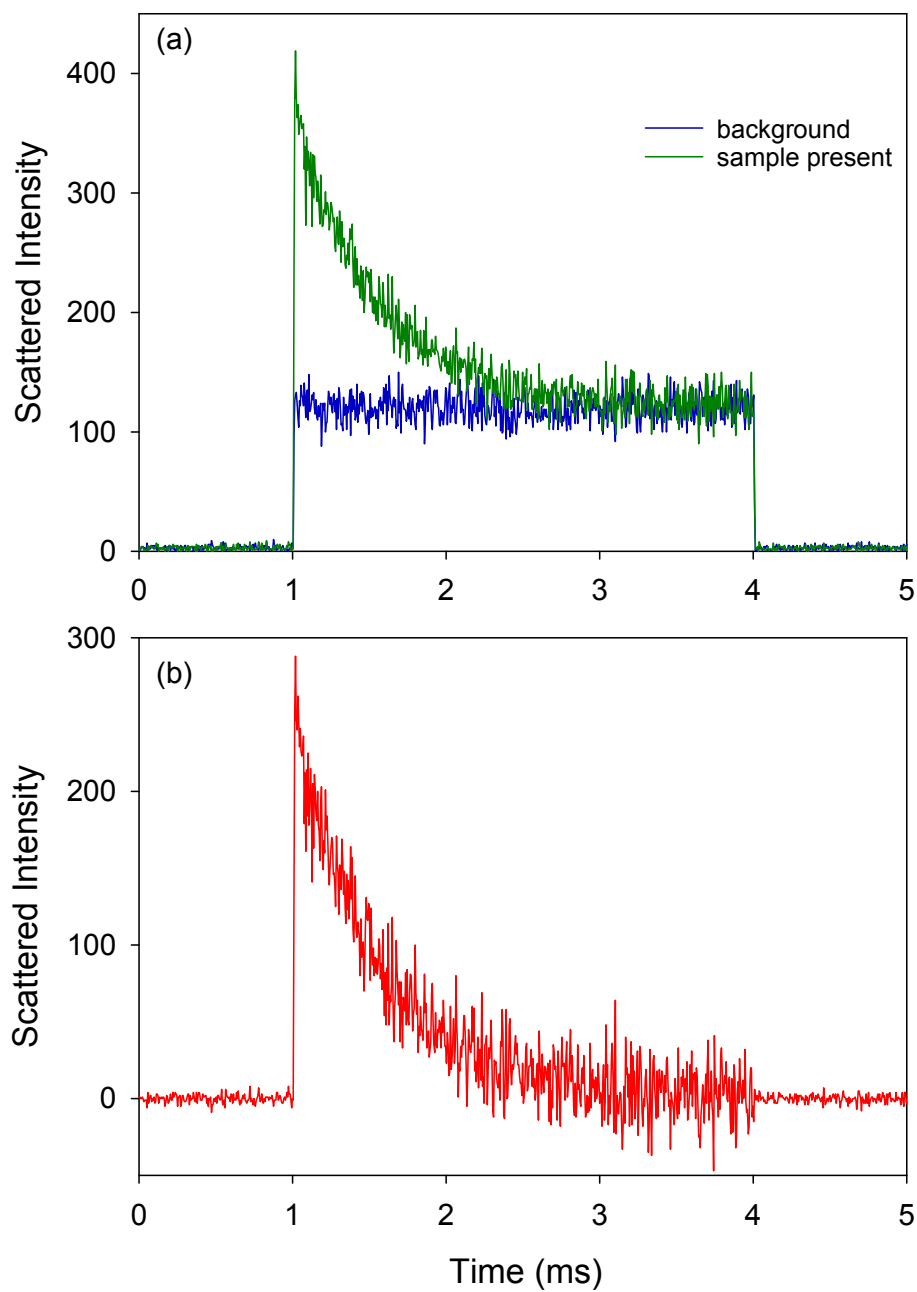
FIG. 52: Fluorescence detected from the FORT with a PMT and counted on a multichannel scalar (Stanford Research Systems, SR430). The PMT signal passes through two stages of amplification (Stanford Research Systems, SR445A) before reaching the MCS. The MCS is triggered on the falling edge from channel 15 on the DAQ.
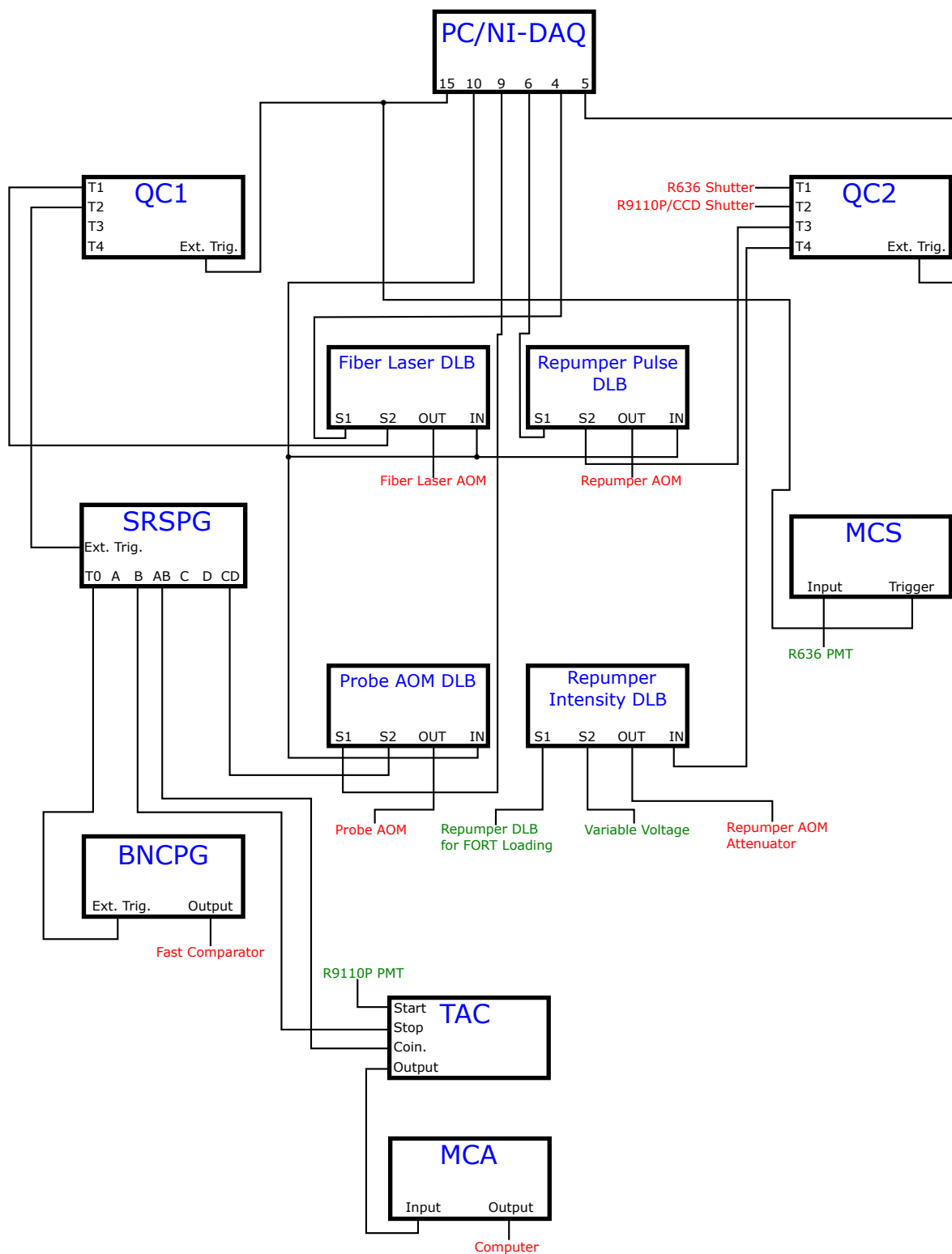
FIG. 53: Schematic of the important timing lines for the experiment. The text in red and green denotes outputs and inputs, respectively.

CHAPTER 6

TIME AND SPECTRAL RESOLVED MEASUREMENTS OF

THE FORWARD EMITTED LIGHT

Here we will present the results of measurements in the time domain on single photon superradiance and in the frequency domain of its counterpart, the cooperative Lamb shift. Both measurements are made in the weak field limit such that they can be compared with the analysis of Chapter 2. We will also give a discussion with the comparison to classical optics and the conflict of interpretations for understanding the data.

6.1 TIME DOMAIN MEASUREMENTS

For each set of experimental conditions, the time domain measurements were collected over a period of two hours using time correlated single photon counting (TCSPC). With the trap creation cycle of ~ 6 s and the embedded pulse sequence, the number of experimental realizations was 3.6×10^5. The probe was programmed for a short 15 ns duration and had a saturation parameter of $s_0 = 0.03$ such that we were in the linear response regime for the atoms. A few of the typical detected curves are depicted in Fig. 54. The curves are characterized by an initial build-up of the signal and the subsequent decay after the probe beam is shut-off. As stated before, there is light leakage of the probe beam present in the detected signal. This occurs because the probe beam has to go through optics anti-reflection coated at 1064 nm, not at the probe wavelength of 780 nm, and each surface has $\sim 15\%$ reflection. With the curvature of the lenses this leads to additional off-axis light with respect to the original probe direction that finds its way to the detector. Additional background may also come from diffraction off the beam block used to separate the probe and forward emitted fluorescence.

To extract the lifetime of the decays we treat the probe signal as a background offset and subtract it from the signals with the sample present. We then choose a point along the curve where the probe has shut off and fit from that point on as single exponential with a vertical offset. The value of the decay depends on the initial point chosen but varies by no more than 10%. The issue of pulse pileup and the distortions it can cause were not considered until after the data was taken and processed. Because the count rate (number of detected
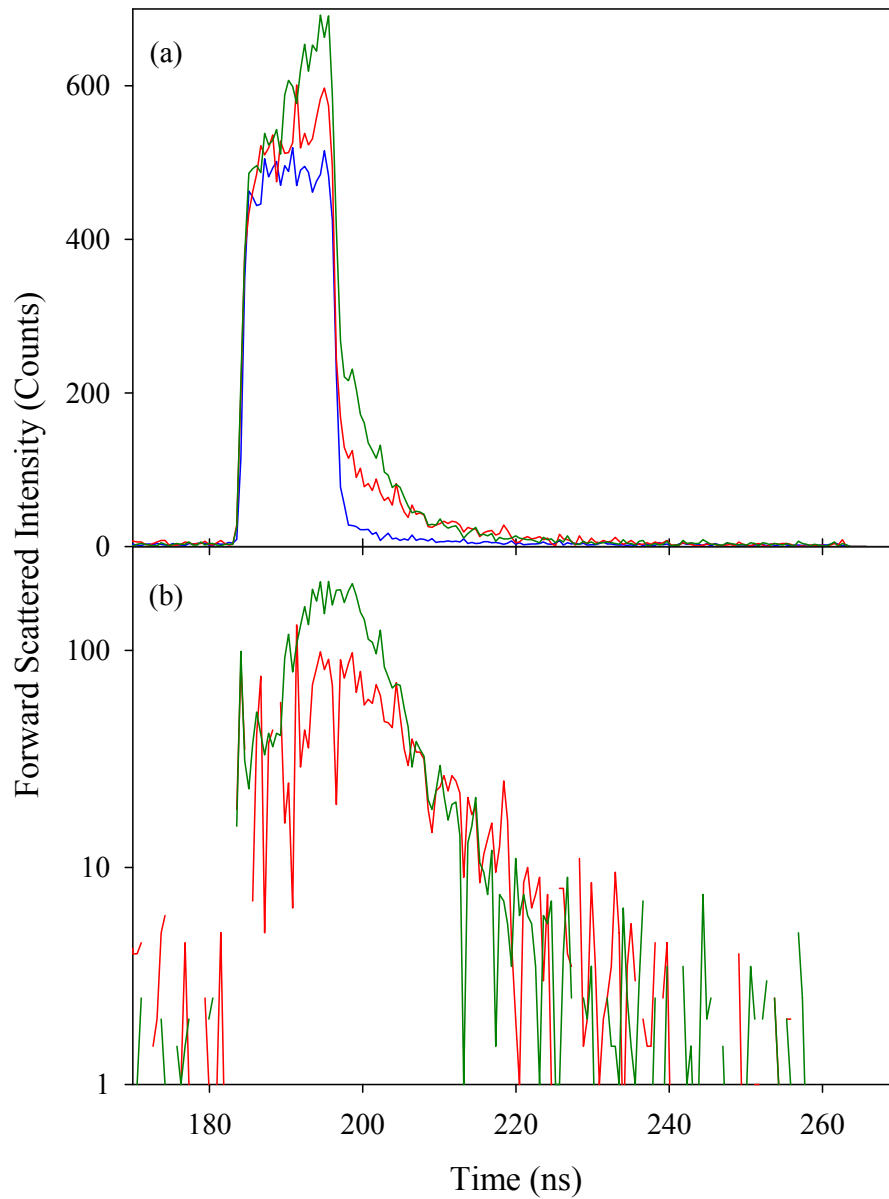
FIG. 54: Representive decay curves for the forward emitted light. The blue curve is light leakage into the PMT from the probe beam and the red and green curves are responses of $N = 10(1) \times 10^3$ and $N = 21(2) \times 10^3$ atoms, respectively. The decay times are 10.6(7) ns for $N \simeq 10,000$ and 5.5(2) ns for $N \simeq 20,000$.
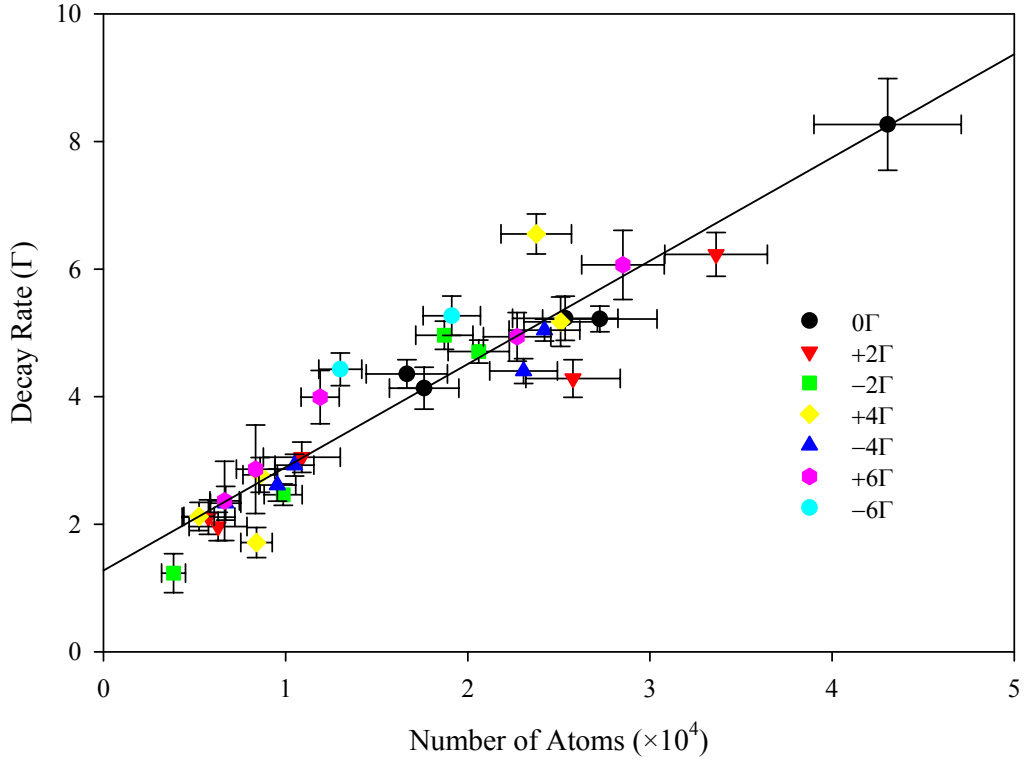
FIG. 55: Decay rate Γ_N vs. N for several detunings, $\Delta = 0, \pm 2\Gamma, \pm 4\Gamma,$ and $\pm 6\Gamma$.

counts over number of experimental realizations) was around 5% and the signal duration was so short, analysis of pulse pileup correction showed negligible change with respect to the extracted decays.

Figure 55 shows the decay rate dependence on the number of atoms. The decay rate is obtained by simply inverting the fitted decay constants from the time dependent data. As predicted from the microscopic theory, the decay rate increases nearly linear in the number of atoms and has a slope of $1.6(1) \times 10^{-4}$ Γ/N and a vertical offset of $1.3(2)$ Γ. This is relatively close to the expression given by (63), where for our trap parameters $\alpha = 2.43(3) \times 10^{-4}$ Γ/N (uncertainty coming from uncertainties in trap radii). Aside from experimental errors in knowing the exact sample shape and the number of atoms, a likely candidate for the discrepancy in the two values is the effect of multilevel structure in ^{87}Rb. While a full vector theory analysis of our system would be advantageous in comparing to experimental data, the scalar approximation is a useful tool to explain the general results. In addition to being linear with respect to the number of atoms, the decay is also independent of detuning
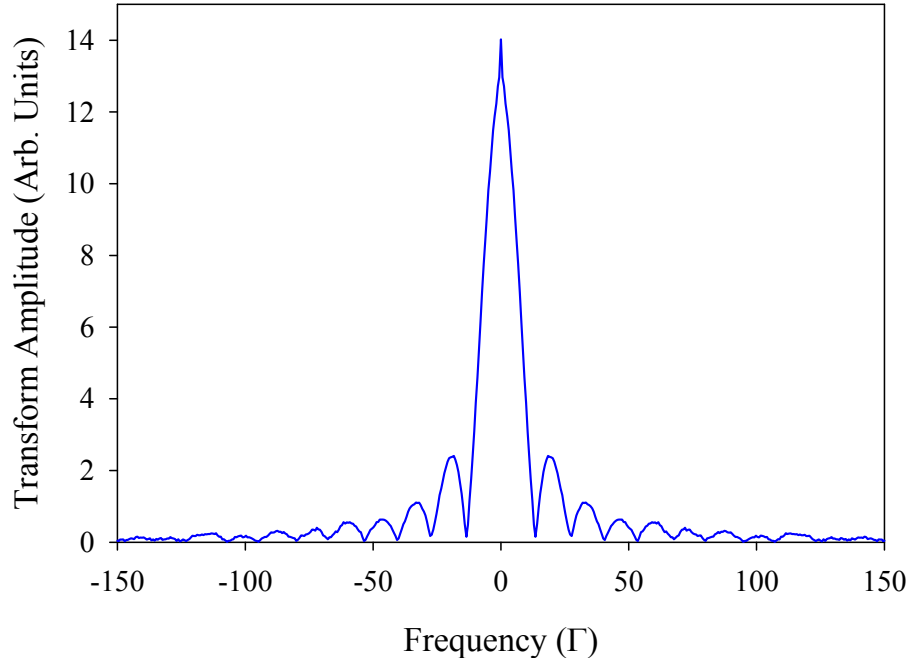
FIG. 56: Fourier transform of the probe pulse that excites the atoms.

within the range of detunings explored in these experiments. This is consistent with the results from the coupled-dipole model over the detuning range probed in experiment. In addition, the probe pulse used has a large bandwidth. In Fig. 56 we show the frequency transform of the probe pulse; it has full a width (within the first envelope) of 165 MHz. This width is quite large compared to the single atom decay rate of 6.1 MHz and if there were any detuning dependence to be discovered faraway from resonance, it would be hard to measure due to the bandwidth. Using the naive approximation that the probe pulse is essentially square, the exact duration can be pulled out which is 12.1 ns;[1] a few ns shorter than the programmed pulse width.

In looking at the polarization degree of the forward emitted light (Fig. 57), we find that it is nearly completely linear polarized in the same direction as the incident probe beam. The polarization is detected by completing a run with no polarizer, a run with the polarizer in the detection arm and in the parallel channel, and a run with the polarizer turned to the perpendicular channel. The results indicate that the emitted light is almost entirely from

---

[1]The Fourier transform of a square pulse gives a width of $\frac{2}{T}$ within the first envelope where T is the duration of the pulse.

Rayleigh scattering (at least in the forward direction).

The data presented in Fig. 55 only shows decays that are observed to be single exponential. As the the number of atoms is increased there is a departure from the exponential behavior and a more complex time dependence appears. Fig. 58 gives an example of the observed signal as well as that predicted by the coupled-dipole model. To compare to the experimental data, the simulation sample has to be rescaled due to computer memory limitations. The optical depth is used as an approximate scaling factor and is matched to what is used in experiment by changing N, r_0, and z_0. For this simulation $r_0 = 0.7$ μm, $z_0 = 41$ μm, $N_{85k} = 5864$, and $N_{147k} = 10000$. The larger samples appear to show an evolution that acquires a bump at the end of the initial decay. As the sample number increases the effect becomes more pronounced. This time evolution is not predicted within the model of the timed-Dicke state (assuming no subradiant coupling [32, 117]) and indicates that propagation of the scattered fields within the sample is more complicated than a single scattering event. Effects similar to this have been seen before but in the context of free-induction decay and optical coherent transients in cold atoms [118, 119, 120, 121, 122]. The reality of these experiments puts an interesting twist on the interpretation of single-photon superradiance and will be a topic of discussion at the end of the chapter.

6.2 SPECTRAL DOMAIN MEASUREMENTS

To make measurements on the spectral dependence of the scattered light we step away from the use of TCSPC due to the issue of pulse pileup and use a very long (10 μs) probe pulse to excite the atoms into their steady state response. The data is no longer taken in a series of pulse trains measurements; instead the sample is probed once per trap realization. The scattered light is detected with a CCD camera with a quantum efficiency of $> 90\%$. The better detection efficiency and increased pulse length make up for the reduction in the total number of experimental realizations that was achieved in the pulse mode. We systematically check that no optical pumping of the atoms occurs during this time from the $F = 2$ ground state to the $F = 1$, so that the atom number can be assumed constant. The data is collected over a period of 30 minutes for each run at fixed detuning. A background image is taken at the beginning of the detuning runs and after, and then averaged. This averaged background is then subtracted from each detuning measurement. The emitted light only takes up a small portion of the CCD (Fig. 59) and so the signal is integrated over that pixel region which is normally a 3 pixel $\times$ 3 pixel square. Larger integration areas were tried but the presence of background noise outside the main image profile caused the count signal to fluctuate for
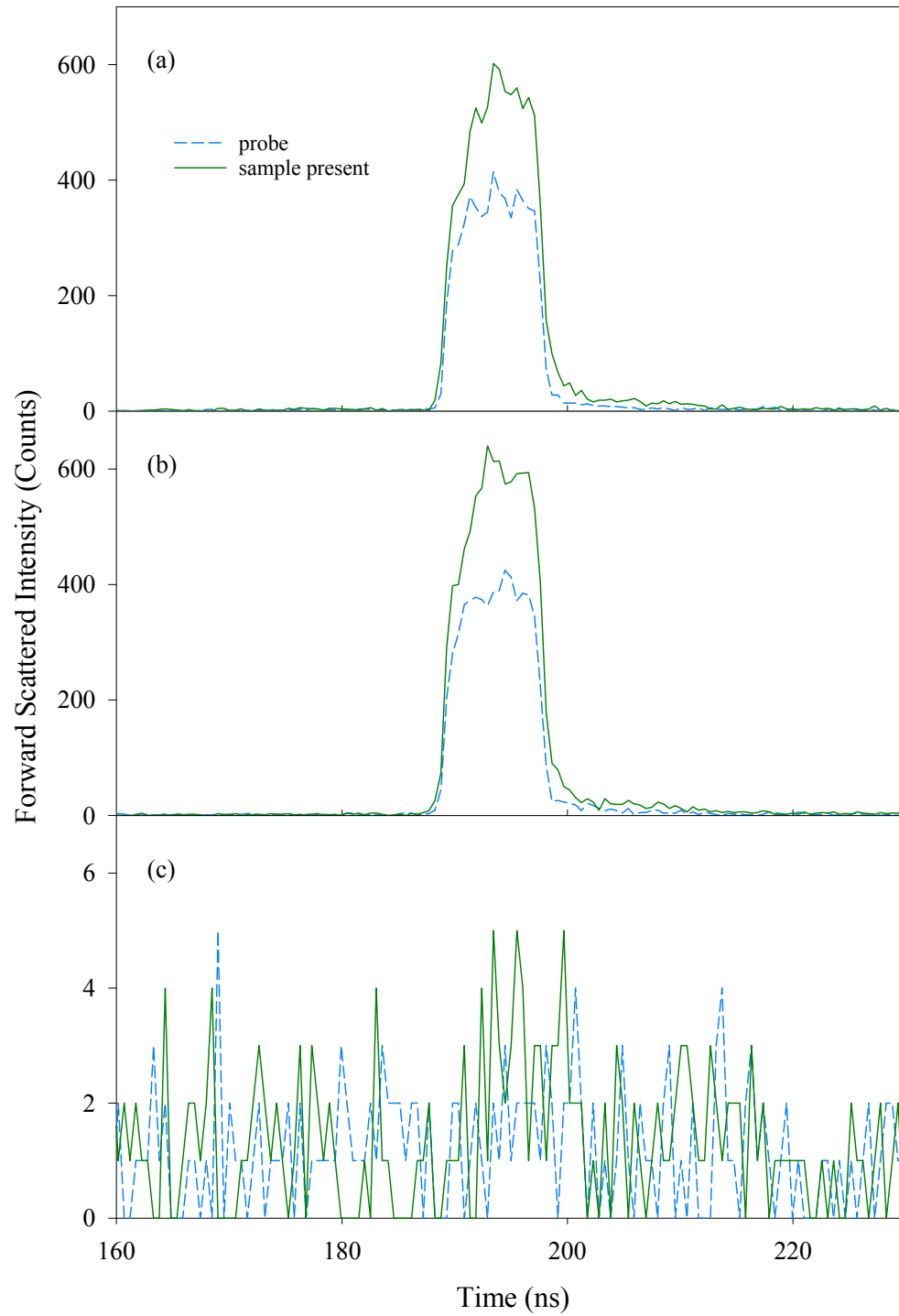
FIG. 57: Polarization dependence of the forward emitted light. (a) No polarizer present with the light from the probe pulse and light from the probe-plus-atomic-sample represented by the dashed blue line and solid green line, respectively. (b) Data taken with a linear polarizer aligned parallel with the polarization of the probe beam. (c) Data taken with the polarizer aligned 90° to the polarization of the probe beam.
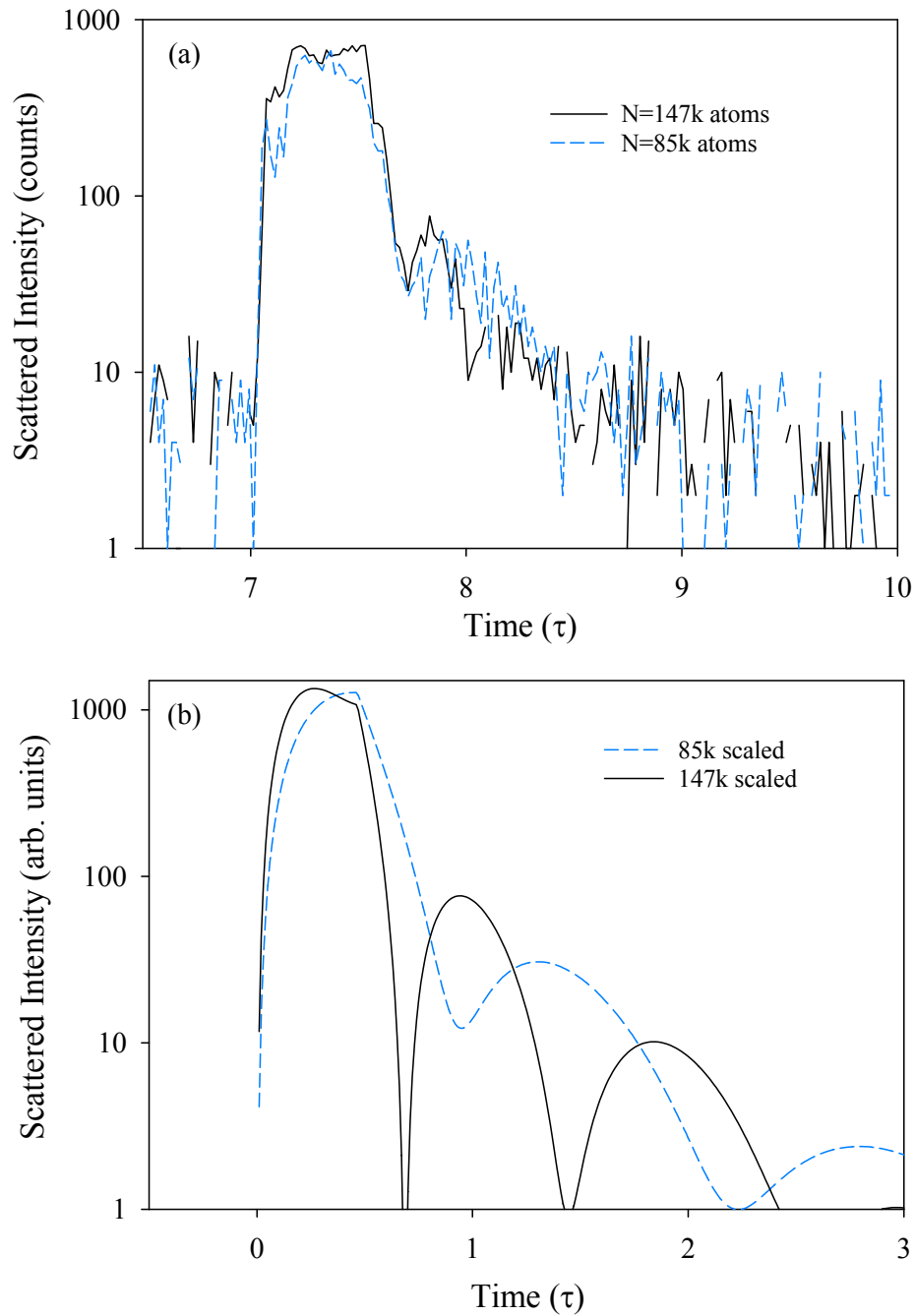
FIG. 58: (a) Measurements for an increased number of atoms. The decay of the scattered light departs from a single exponential behavior and develops oscillations that increase in frequency for an increase in atom number. (b) Simulations using the coupled dipole model, but the sample size is to be rescaled due to computer memory limitations for large numbers of atoms.
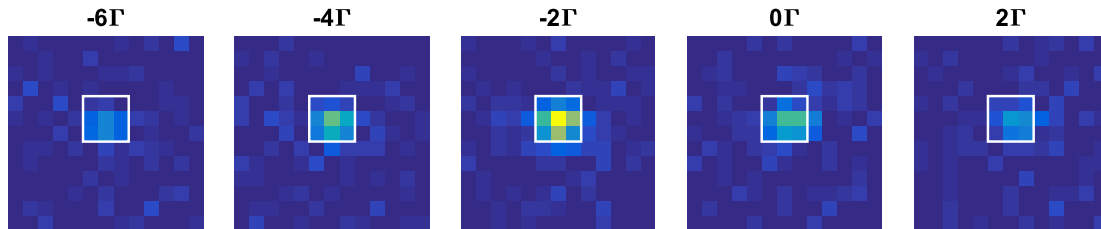
FIG. 59: CCD images for a few different probe beam detunings. The number of atoms for this particular data run is $\sim 2.7 \times 10^4$. In this case a 3 pixel $\times$ 3 pixel box has been drawn around the most intense portion of the image.

increasing box size. The 3 pixel $\times$ 3 pixel box was found to provide the best signal-to-noise.

Several curves are presented in Fig. 60 showing the response of the system to the detuning of the incident probe. For a small number of atoms the scattered light is approximately Lorentzian and shows a slight shift to the red side of resonance. The width of the response is also broadened which would be indicative of superradiant emission. Comparing the results with what is expected from microscopic theory (61) gives reasonable agreement. The differences likely stem from the same discrepancies described in the value of the slope for Fig. 55 and the shape factor α. In Fig. 61, the shifts are extracted from the detuning curves and plotted versus the number of atoms. The shifts are on the same order as predicted by Eq. (61). Widths extracted from the Lorentizian fits do not follow such a smooth pattern as would be predicted by Fig. 55. This likely due to significant background in the CCD image for lower number atoms which would tend to give an apparent broadening. As the sample number increases, a double peak spectrum can be seen to arise. This is interesting as it significantly departs from the expected behavior predicted by single photon superradiance, yet still is described by simulation with the coupled dipole model. We interpret the results as meaning that propagation effects contribute to the sample's response and distort what is expected from the ideal case.

Commonly, the scaling factor that is associated with the collective Lamb shift is the density. However, in what was shown the shift was measured to be quite large even at low density ($< 10^{12}$ a/cc). This is because the shift is also associated with the geometry of the sample, just like in the case for the collective decay rate. Shown in Fig. 62 is the numerical calculation of (61) for different geometries with an indication for which one is our sample.
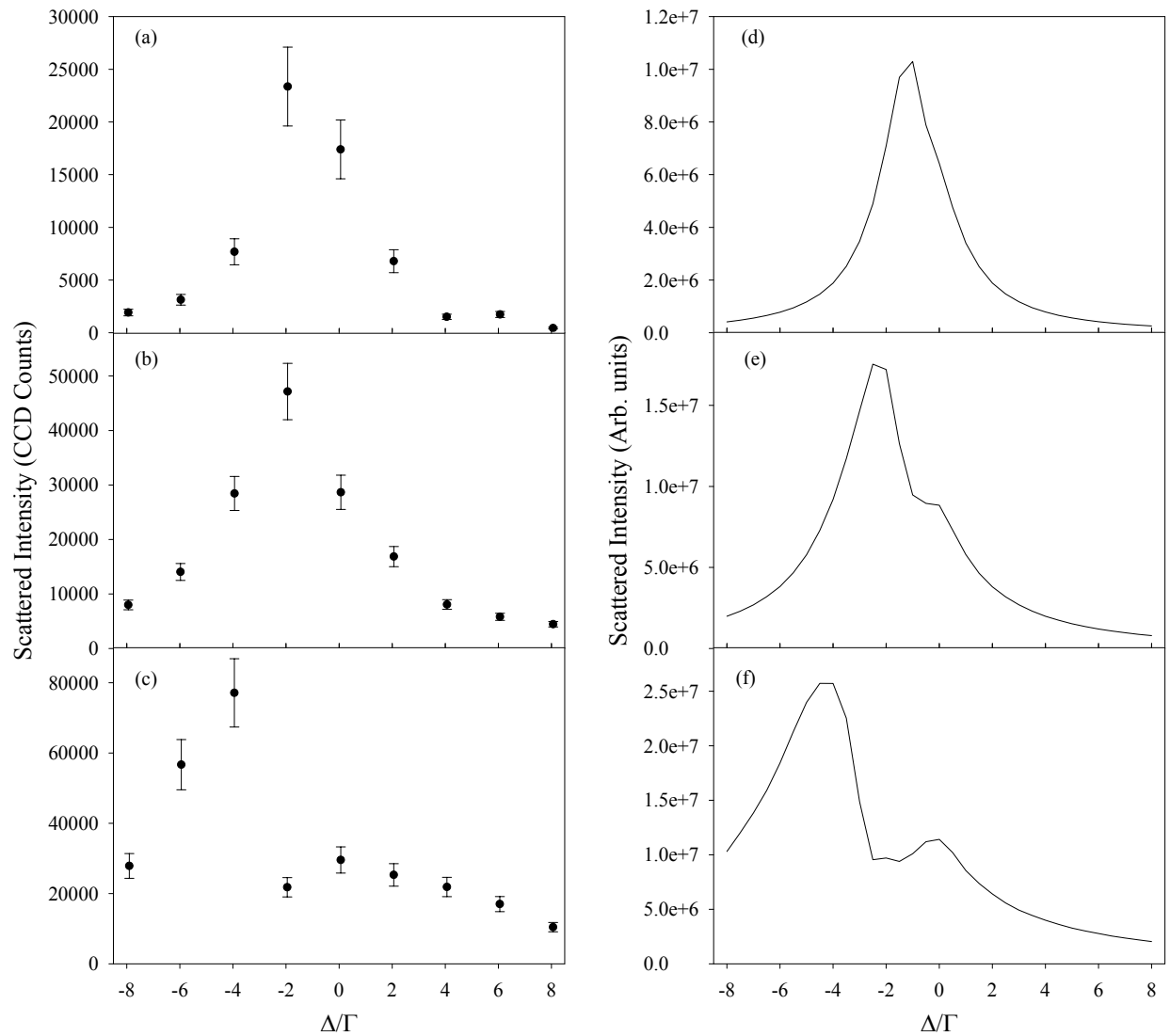
FIG. 60: (a)-(c) are steady-state detuning response curves for $N \simeq 14\mathrm{k}, 27\mathrm{k}$, and $53\mathrm{k}$ atoms. The results are compared to the coupled-dipole model by scaling the sample number down and reducing the sample size so that the optical depth is the same as in experiment. The plots (d)-(f) correspond to $N = 2.5\mathrm{k}, 5\mathrm{k}$, and $10\mathrm{k}$ atoms.
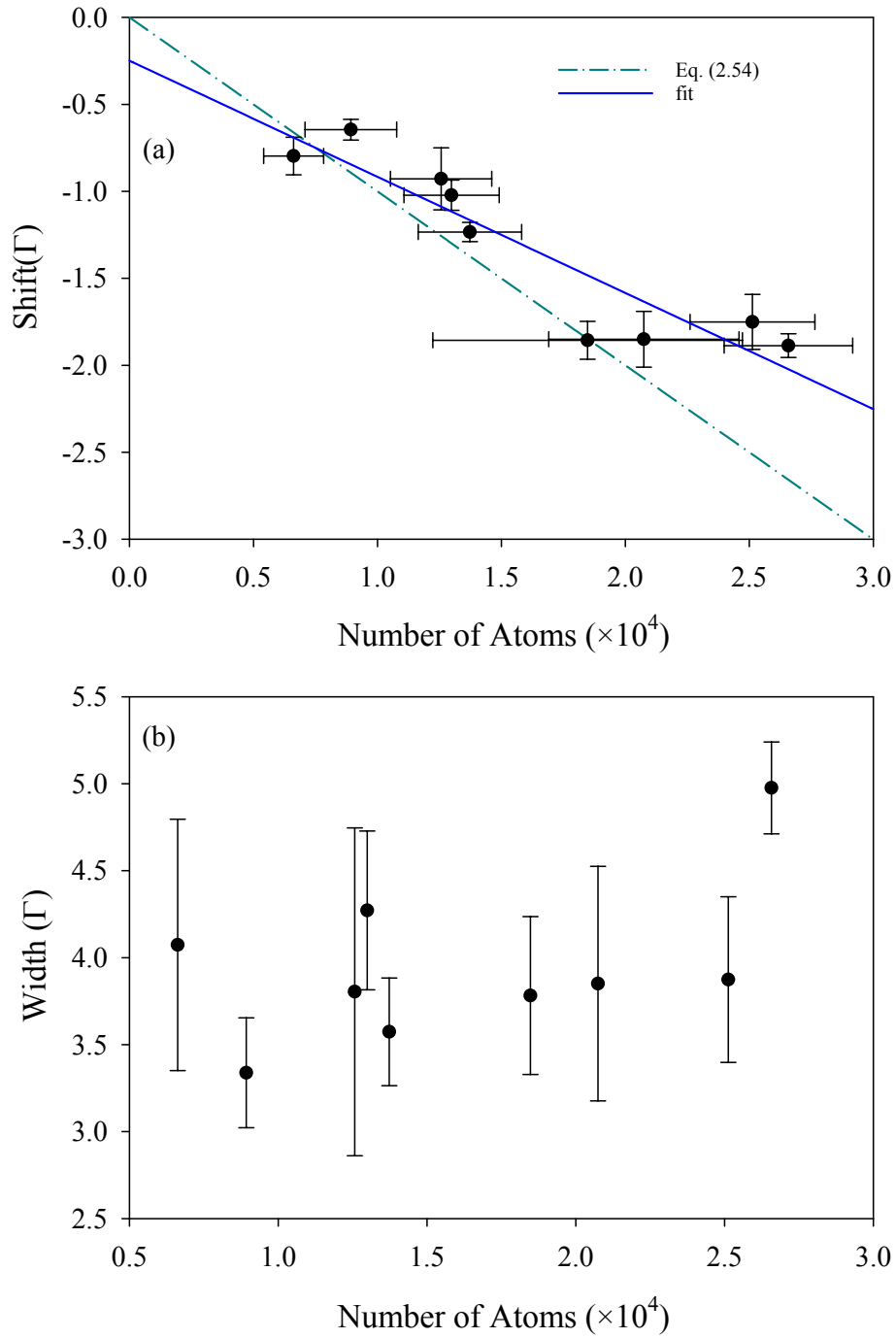
FIG. 61: (a) Shift of the response as a function of the number of atoms. (b) Width of the response as a function of a number of atoms. The error bars are statistical and largely due to background signal contribution.
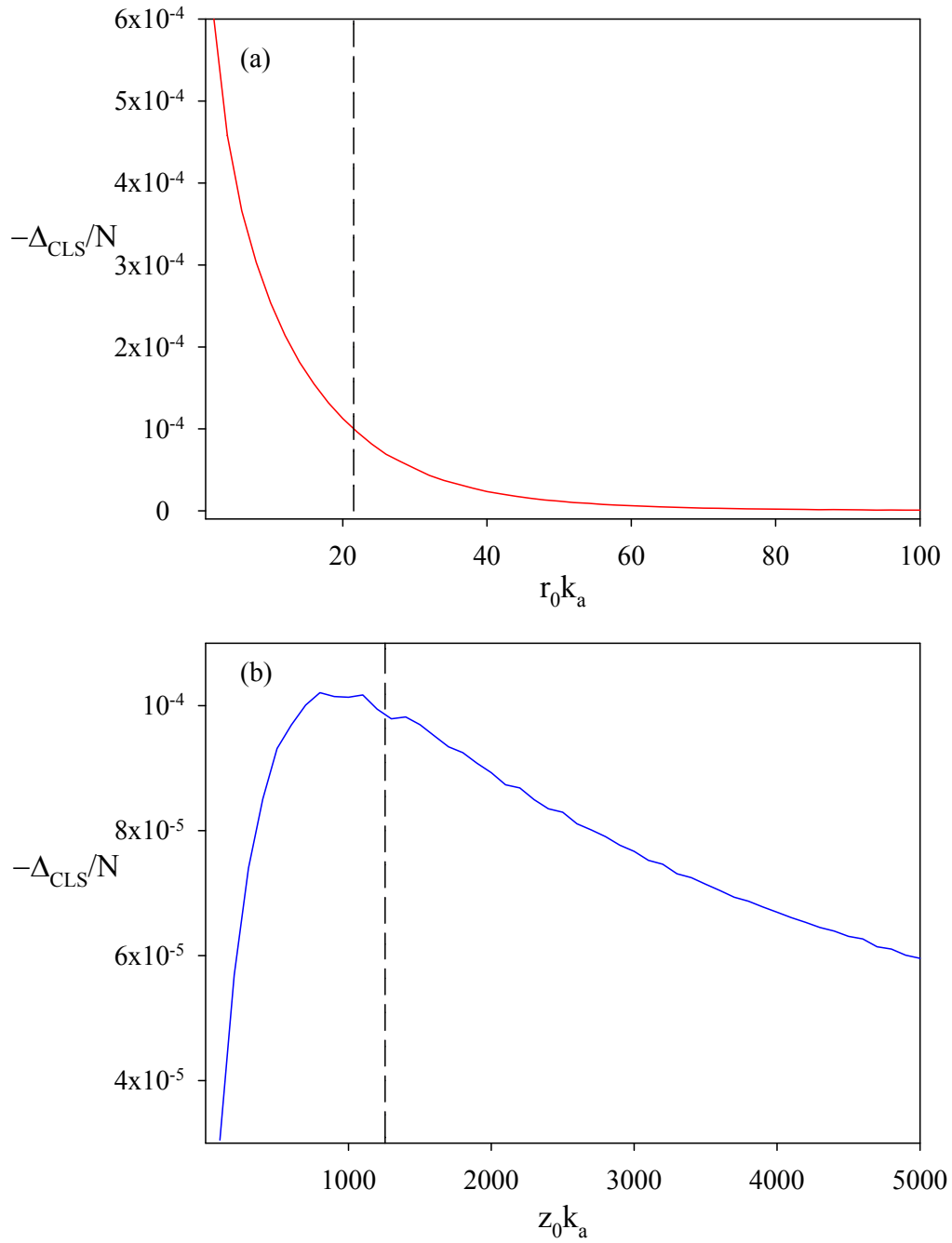
FIG. 62: Numerical evaluation of (61) for the cooperative Lamb shift showing the sample size dependence for (a) fixed z_0 and varying r_0 and (b) fixed r_0 and varying z_0. In each case the black dashed line indicates the experimental value for r_0 and z_0.

6.3 DISCUSSION

The observed emission rate and spectral dependence of the scattered light are in good agreement with the expectations from microscopic scattering theory. One would be encouraged to say that the existence of cooperative effects in extended samples is quite evident and that the realm of quantum optics has become that much richer. However, in interpretation of the microscopic theory it was assumed that only the "interesting" quantum nature of the process would be observed, but at some level the microscopic description and that predicted by classical optics must overlap. This brings the question [5, 6, 123]: how much of the extended sample response can be explained by classical optics?[2] Certainly if a majority of the observed effects identified as cooperative in microscopic theory can be just as well be explained by classical optics, which makes no attempt in labeling enhanced decay rates and frequency shifts, it might suggest that the microscopic results are misinterpreted. This will be the topic of discussion for this section and will produce some sobering realizations about what is really meant by *cooperative* and *collective*.

6.3.1 CLASSICAL OPTICS IN THE TIME DOMAIN

To analyze the temporal response of the atomic ensemble, classically, requires solving the time-dependent Maxwell-Bloch equations. Contrary to what was done in Ch. 4, we will seek solutions in one dimension for simplicity without losing context for the discussion. The one dimensional problem comes down to solving (70) and the Maxwell wave equation for the electric field,

$$\left(\frac{\partial^2}{\partial z^2} - \frac{1}{c^2}\frac{\partial^2}{\partial t^2}\right) E = \mu_0 \frac{\partial^2 P}{\partial t^2}. \tag{128}$$

Invoking the slowly varying envelope approximation and introducing the *Bloch variables* [124] U and V such that $\tilde{\rho}_{eg} = \frac{1}{2}(U - iV)$, the Maxwell-Bloch equations become

$$\frac{\partial}{\partial t}\begin{pmatrix} W \\ U \\ V \end{pmatrix} = \begin{pmatrix} -\Gamma & -\mathrm{Im}\,(\Omega) & -\mathrm{Re}\,(\Omega) \\ \mathrm{Im}\,(\Omega) & -\Gamma/2 & \Delta \\ \mathrm{Re}\,(\Omega) & -\Delta & -\Gamma/2 \end{pmatrix}\begin{pmatrix} W \\ U \\ V \end{pmatrix} + \begin{pmatrix} -\Gamma \\ 0 \\ 0 \end{pmatrix} \tag{129}$$

$$\left(\frac{\partial}{\partial z} + \frac{1}{c}\frac{\partial}{\partial t}\right)\Omega = \frac{\kappa\Gamma}{2}(U - iV). \tag{130}$$

---

[2]Classical optics in this sense refers to solving the Maxwell-Bloch equations for an extended atomic sample. While the Bloch equations were derived quantum mechanically, a corresponding set of equations could have been obtained assuming the atom was a damped harmonic oscillator driven by an external force. From this point of view the system is purely classical.

Equations (129) and (130) can be solved numerically a few different ways. In Appendix E we give an overview of the method we use to solve them. Pictured in Fig. 63 is the scattered intensity for an elongated one dimensional sample with length L close to what we have in experiment. The sample is excited with a low intensity pulse ($s_0 = 0.01$) and has a duration of $0.5\Gamma^{-1}$. Similar to the microscopic simulations and experimental data, the scattered field is characterized by a fast decay at the end. For increasingly larger optically deep samples ($b_0 = \kappa L$), the trailing oscillations appear. It can actually be shown [119, 32] that the functional form for the free-decay contains a $J_0(\sqrt{2b_0\Gamma t})$ term which agrees with the oscillatory behavior.

It may seem surprising, coming from the perspective of microscopic cooperative effects, that such a simple model of light scattering can produce the complex behavior observed in experiment. Certainty there are differences, such as the fact that the increased decay takes effect at much lower optical depths than in experiment ($b_0 \sim 50 - 100$), but the model is only in one dimension and a full three dimensional analysis is necessary for determining the real difference in the microscopic and classical theories. The term free-induction decay is normally used to describe the results when the classical approach is taken and numerous experiments have been performed that examine it in cold atoms [118, 119, 120, 121, 121]. The argument for the fast decays from this perspective is that it is due to the transient response of the susceptibility when subject to a driving pulse (see Appendix D). This is much like in linear systems theory where a filter network changes the input by some transfer function $H(\omega)$ (see Fig. 64). In the experiments mentioned above, the probing beam is well within the sample of cold atoms such that a one-dimensional system can be assumed. Also, the transmitted intensity is measured, not the scattered intensity. Cases like ours where the entire sample is excited by a plane wave and only the scattered intensity in the forward direction is measured have not been well studied for the temporal evolution.

6.3.2 CLASSICAL OPTICS IN THE SPECTRAL DOMAIN

We continue the comparison with the classical response by once again looking for the solution to the Maxwell-Bloch equations but in the steady state regime. Here, for a two level atom, the bandwidth of excitation pulse will no longer make a contribution to the spectral response and the detuning dependence of the process can be extracted. We use the same technique from Chapter 4, but with the beam directed down the long axis of the FORT. Contrary to the previous section, the exact three dimensional response can be simulated which is important as off-axis scattering modes come into play.
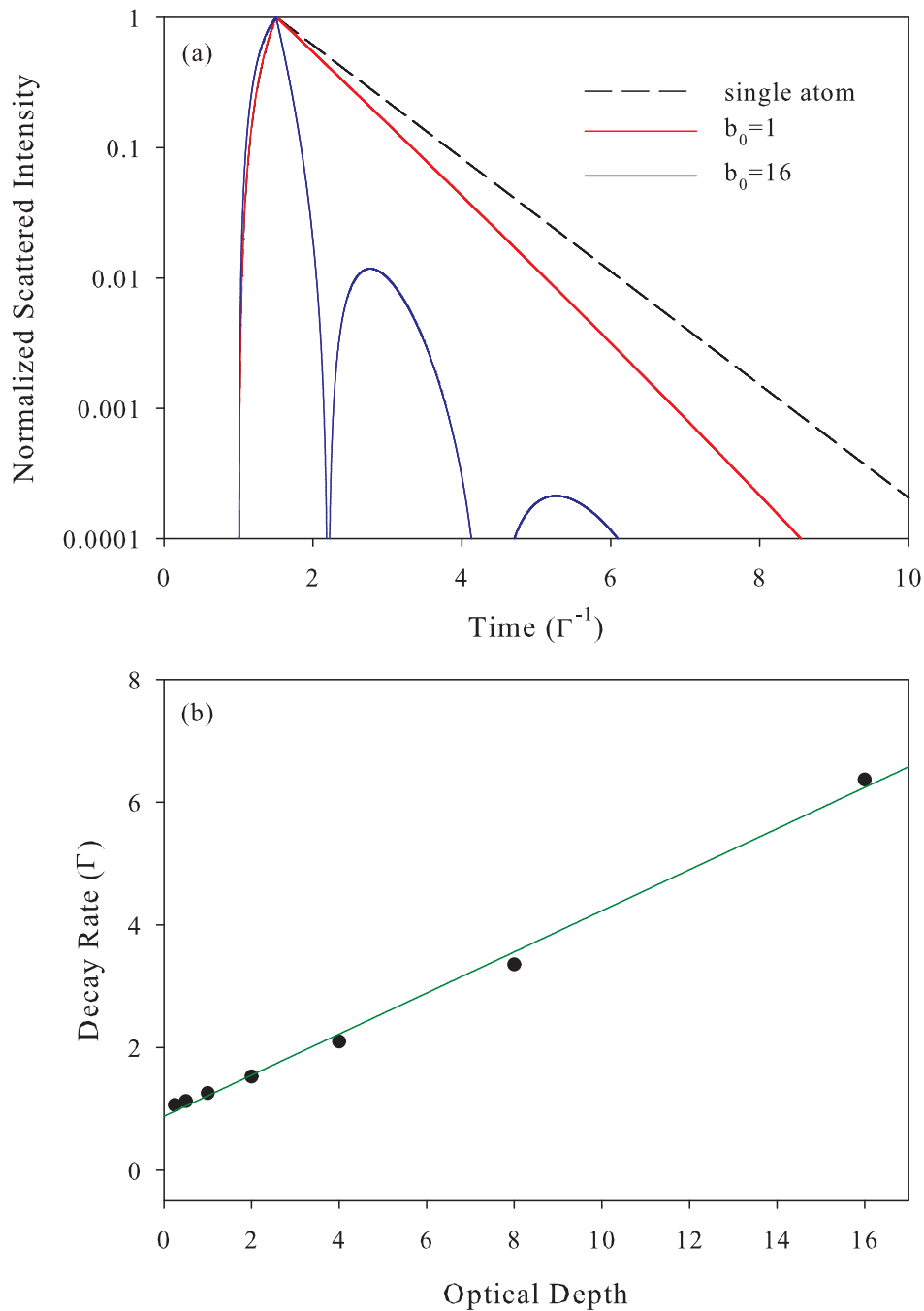
FIG. 63: (a) Temporal response for a single atom, a sample with $b_0 = 1$, and a sample with $b_0 = 16$. The response is faster for an increasing optical depth (approximately single exponentially) and develops an oscillatory behavior as in experiment and the microscopic model. (b) The extracted decay rate for several optical depths. The decay rate increase is nearly linear with some deviation due to the non-exponential behavior for higher optical depth samples. Since we are not changing the length of the sample, the peak optical depth and number of atoms are directly proportional to each other.

FIG. 64: Demonstration of the linear response of a filter network. The sample can be thought of as a filter with response function $H(\omega)$. In the diagram, $X(\omega)$ is synonymous with the incident field and $Y(\omega)$ with the transmitted field.

Fig. 65 shows the total absorbed light one would expect for a bi-Gaussian sample as is probed in the experiment. Here the light is collected a distance of $\sim 2000\lambda$ (1.6 mm) away from the sample which is approximately in the far field limit. The absorption is small as the incident beam is much larger than the radial cross section of the sample and most of the light passes around it. In addition, the amount of light that passes around a rectangular area is pictured. This is similar to what we have in experiment where we occlude the main portion of the incident field. From the figure it can be seen that the response is quite different than the total transmitted intensity and more light on the red side of resonance passes around the block than the blue. The transmission around the beam block appears similar to what is measured in the experiment and what is predicted as the scattered intensity from the microscopic theory.

The root of the observed transmission curves from the simulation can be explained from the beam trajectories through the sample. Fig. 66 gives an example of the process showing what happens to light as it propagates for red and blue detunings. The sample in this case has the same dimensions as in experiment with $N = 17,500$. For red detunings, like we observed in the microscopic lensing experiments [125], the light is refracted into the sample leading to a longer path length and thus more absorption. For blue detunings, the light is refracted away from the center of the sample. In the far field this lensing effect causes what red detuned light is transmitted to diverge at a greater angle giving more transmission around the beam block. The transverse profile of the transmitted field is shown in Fig. 67 and the presence of the sample causes diffractive rings to appear. These diffractive rings cause there to be an angular dependence to the spectral profile meaning a different collection angle results in a different detuning dependent curve (see [126] for a discussion of this effect from a microscopic point of view).

We are now left with a conflict of interpretations as to what are the origins of the observed effects in the experiment. We should at this point give a definition for the meaning
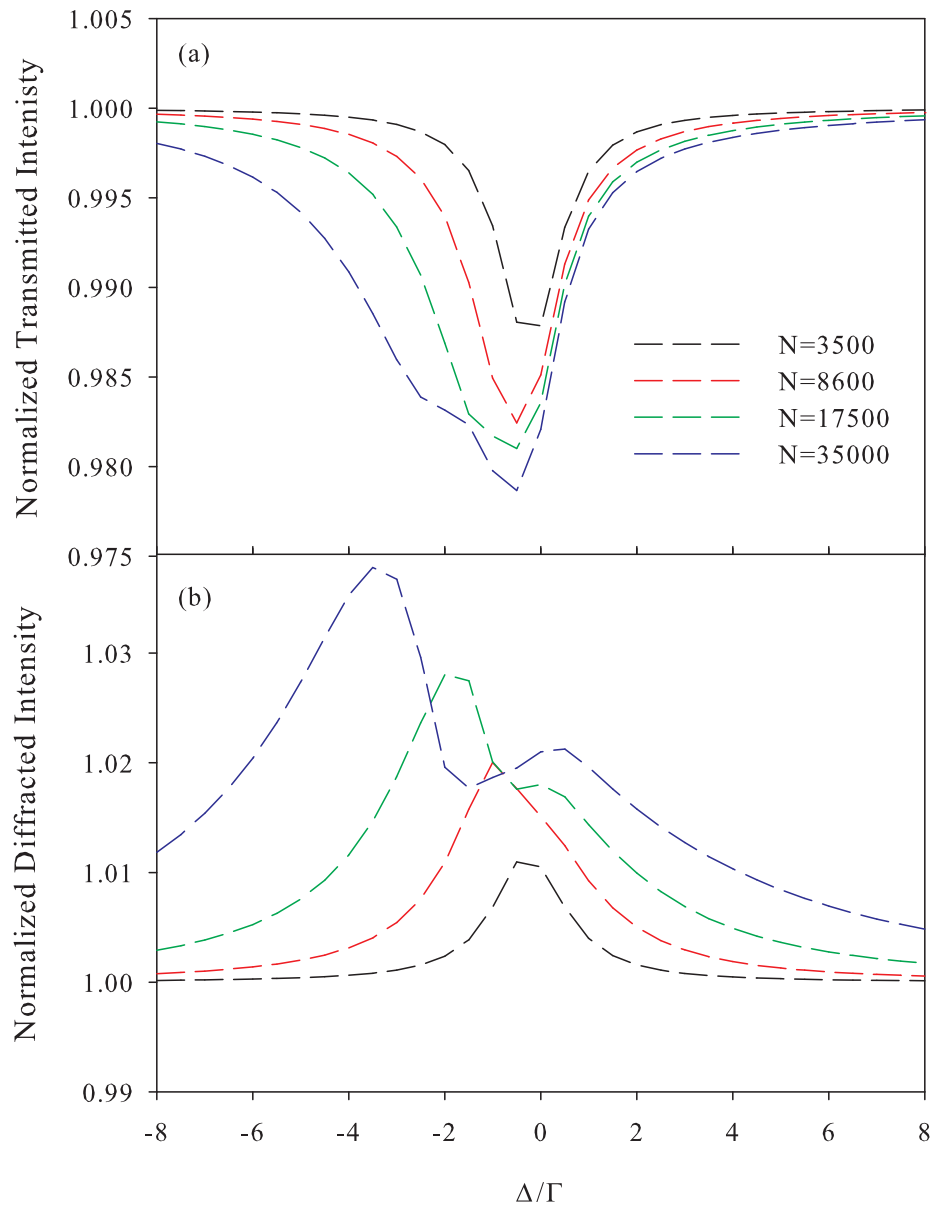
FIG. 65: (a) The total transmitted laser intensity at a distance of 2000λ from the sample. The intensities have been normalized to the probe intensity at the point of observation. (b) The transmitted intensity around a beam block 80λ wide and a very large height (similar to experiment). The intensities have also been normalized to the probe intensity that gets around the block with no sample present.
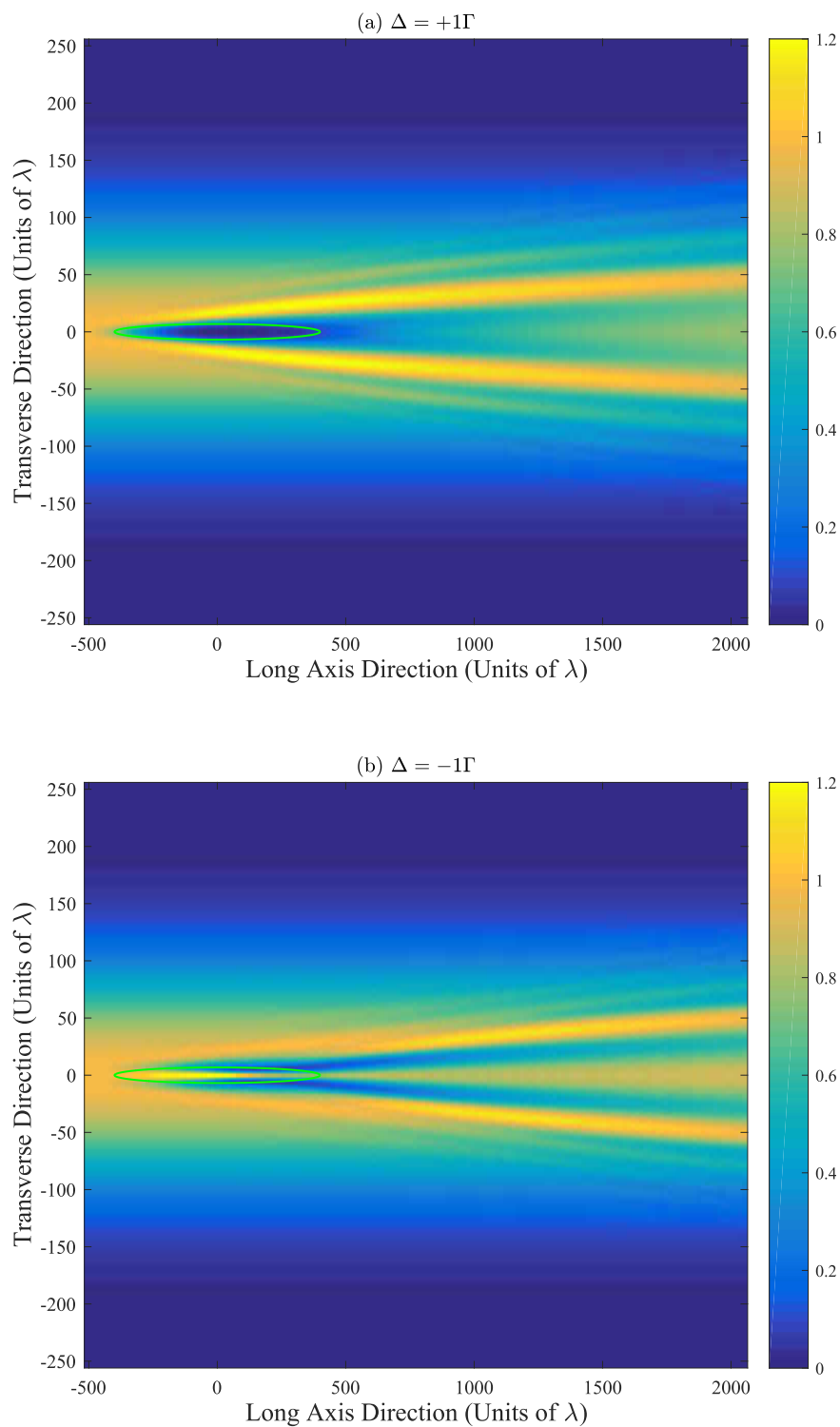
FIG. 66: Propagation of the probe beam through the long axis of the FORT using the split-step algorithm for (a) $\Delta = +1\Gamma$ and (b) $\Delta = -1\Gamma$. The green ellipse indicates the location of the sample. The intensity is normalized to the peak intensity of the incident beam.
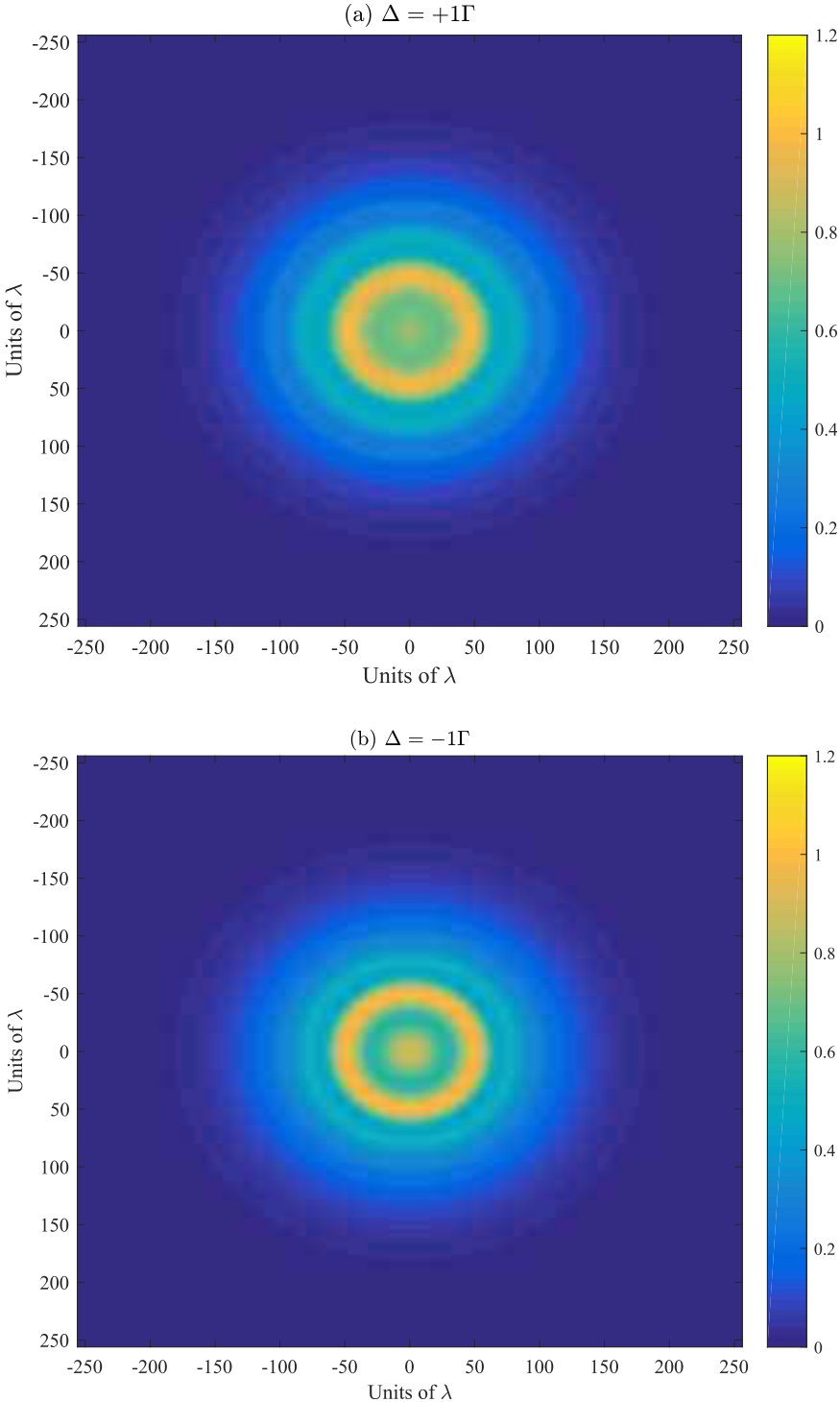
FIG. 67: Normalized transmitted beam profile at $z = 2000\lambda$ for (a) $\Delta = +1\Gamma$ and (b) $\Delta = -1\Gamma$. Diffraction rings are clearly visible.

of collective and cooperative. We define collective as the observation of effects from many atoms, different than what is expected from a single atom. These effects are not because the atoms are having one-on-one interactions but because of the overall effect of the scattered intensity from many radiators in the far-field. We will define cooperative as one-on-one interactions that lead to deviations from the single atom response. The definitions mean that on the one hand the data can be interpreted as the interesting effects of cooperativity which result in enhanced, directional spontaneous emission and a shift of the resonance line for the atomic sample. Or, on the other hand, interpreted as the role of classical optics and how the intricate form of the atomic susceptibility due to sample geometry can give rise to complex, collective behavior which may be mistaken for other physical phenomena. A pessimistic approach to the problem would be to say that all behavior concerned with low light excitation of atomic media is a mundane consequence of classical optics. Yet, it is still very interesting that non-single atom responses can be predicted and given a descriptive form from a microscopic theory as opposed to running "black-box" classical simulations.

While the true cooperative nature of a collection of atoms may be best encased by subradiance and far off-axis superradiance [123], the ability to predict and control a generic sample's emission properties in the forward direction could lay the groundwork for interesting future studies such as microscopic optical element devices. Perhaps a better approach for handling the problem in the future is to look into the statistics of the emitted light and, for example, make second order correlation function measurements ($g^{(2)}(\tau)$) [42]. There, along with other broadening mechanisms such as Doppler motion, radiation trapping, and magnetic field contributions [127], effects from cooperativity, if they do exist, should show up in the functional form of $g^{(2)}$. Similar steps have been taken in the past to analyze the phenomena of Anderson localization of light [128] by statistical measurements, which has also seen its fair share of controversy in making time-domain measurements [15, 129].

CHAPTER 7

CONCLUSIONS

We have presented measurements of forward scattered light from a highly extended, cold atomic sample of ^{87}Rb in the time and spectral domain. The measurements are consistent with the study of single-photon superradiance and the cooperative Lamb shift. The time domain measurements were characterized by a fast decay that depended approximately linearly on the number of atoms and on the particular shape of the sample. The spectral domain measurements showed a large shift to the red side of resonance with an increased width that also depended on the number of atoms and the geometry of the sample. While the results were well explained by the theory of microscopic scattering and the timed-Dicke state formalism, classical optics also proved able to replicate the observed data. The durability of classical optics brings into light the interesting parallel between a quantum optical approach of the process and a semi-classical based approach. Further work is needed, theoretically and experimentally, to fully answer the true nature of this light scattering process [5, 6, 123].

The realization of the experiment required extensive use of precision timing equipment and the method of mode-mismatching to detect the forward scattered light. Fast pulses were generated with rise and fall times well below the single atom decay with a LiNbO$_3$ intensity switch that was controlled with homebuilt circuitry. By using time correlated single photon counting we were able to detect the superradiant decay from the atoms with timing resolution limited by the electron transit time jitter of the PMT. We incorporated a pulse cycle protocol to increase the duty cycle of the experiment which involved quickly turning on and off the dipole trapping beam. For the spectral domain measurements, we made one long probe excitation and recorded it with a CCD camera.

Along the way we explained the physics of atom trapping for creating MOTs and FORTs. The MOT, created by laser radiation pressure and magnetic fields, was used to load the FORT which provided us with the necessary sample geometry for the experiment. The FORT, unlike the MOT, was created by a dipole trapping force that had a very low scattering rate (0.5 s^{-1} for our trap parameters). Calculations were given for the expected light shift in the FORT that have been confirmed by other theoretical and experimental investigations. Use of the light shift and the technique of parametric resonance allowed us to know the specific sample characteristics very well.

We also described experiments that investigated microscopic lensing effects from laser propagation through the small radius of the elongated atom trap. The results, which were initially assumed to be shifts of the resonance line due to density effects, were found to be explained by a beam propagation simulation. The beam propagation simulation, what was called the "split-step method", allowed to very accurately predict how the beam was affected by the presence of the sample. We provided a simple model of a thin lens that matched agreeably with the simulation and gave a focal length on the order of a few hundred microns.

For the future it would be interesting to study the superradiant and cooperative Lamb shift effects in different geometries. It should be possible to find specific shapes for which there is no cooperative Lamb shift which may be advantageous for precision measurements and quantum sensors. Additional studies of superradiance and subradiance that incorporate Doppler motion and other inhomogenous broadening mechanisms are also warranted [29]. Involving controlled inhomogenous broadening may provide a very robust way of transporting a large portion of the atom population into subradiant states and hence creating quantum memories. It would also be interesting to pursue measurements that examine the statistics of the emitted light, such as $g^{(2)}$, which could help clarify if cooperative line broadening mechanisms are actually present.

BIBLIOGRAPHY

[1] Griffin, P. F. *Laser Cooling and Loading of Rb into A Large Period, Quasi-Electrostatic, Optical Lattice.* PhD thesis, Durham, (2005).

[2] Pritchard, M. J. *Manipulation of ultracold atoms using magnetic and optical fields Manipulation of ultracold atoms using magnetic and optical fields.* PhD thesis, Durham, (2006).

[3] Anderson, P. W. *Science* **177**, 393 (1972).

[4] Jackson, J. D. *Classical Electrodynamics, Third Edition.* Wiley, (1999).

[5] Javanainen, J., Ruostekoski, J., Li, Y., and Yoo, S. M. *Phys. Rev. Lett.* **112**, 113603 (2014).

[6] Javanainen, J. and Ruostekoski, J. *Opt. Express* **24**, 254318 (2014).

[7] Kaiser, R. *J. Mod. Opt.* **56**, 2082 (2009).

[8] Labeyrie, G., Delande, D., Müller, C. A., Miniatura, C., and Kaiser, R. *Opt. Commun.* **243**, 157 (2004).

[9] Sigwarth, O., Labeyrie, G., Delande, D., and Miniatura, C. *Phys. Rev. A* **88**, 033827 (2013).

[10] Baudouin, Q., Mercadier, N., Guarrera, V., Guerin, W., and Kaiser, R. *Nat. Phys.* **9**, 357 (2013).

[11] Pellegrino, J., Bourgain, R., Jennewein, S., Sortais, Y. R. P., Browaeys, A., Jenkins, S. D., and Ruostekoski, J. *Phys. Rev. Lett.* **113**, 133602 (2014).

[12] Sokolov, I. M., Kupriyanov, D. V., and Havey, M. D. *J. Exp. Theor. Phys.* **112**, 246 (2011).

[13] Keaveney, J., Sargsyan, A., Krohn, U., Hughes, I. G., Sarkisyan, D., and Adams, C. S. *Phys. Rev. Lett.* **108**, 173601 (2012).

[14] Labeyrie, G., de Tomasi, F., Bernard, J.-C., Müller, C., Miniatura, C., and Kaiser, R. *Phys. Rev. Lett.* **83**, 5266 (1999).

[15] Sperling, T., Bührer, W., Aegerter, C. M., and Maret, G. *Nat. Photonics* **7**, 48 (2012).

[16] Skipetrov, S. E. and Sokolov, I. M. *Phys. Rev. Lett.* **112**, 023905 (2014).

[17] Skipetrov, S. E. and Sokolov, I. M. *Phys. Rev. Lett.* **114**, 053902 (2015).

[18] Kuzmich, A., Bowen, W. P., Boozer, A. D., Boca, A., Chou, C. W., Duan, L.-M., and Kimble, H. J. *Nature* **423**, 731 (2003).

[19] Sparkes, B. M., Bernu, J., Hosseini, M., Geng, J., Glorieux, Q., Altin, P. A., Lam, P. K., Robins, N. P., and Buchler, B. C. *J. Phys. Conf. Ser* **467**, 012009 (2013).

[20] Scully, M. O. *Phys. Rev. Lett.* **115**, 243602 (2015).

[21] Sokolov, I. M. and Kupriyanov, D. V. *Phys. Rep.* **Preprint**, 1–70 (2016).

[22] Dicke, R. H. *Phys. Rev.* **93**, 99 (1954).

[23] Rehler, N. and Eberly, J. *Phys. Rev. A* **3**, 1735 (1971).

[24] Crubellier, A., Liberman, S., and Pillet, P. *Phys. Rev. Lett.* **41**, 1237 (1978).

[25] Skribanowitz, N., Herman, I. P., MacGillivray, J. C., and Feld, M. S. *Phys. Rev. Lett.* **30**, 309 (1973).

[26] M. Gross, C. Fabre, P. Pillet and Haroche, S. *Phys. Rev. Lett.* **36**, 1035 (1976).

[27] Gross, M. and Haroche, S. *Phys. Rep.* **93**, 301 (1982).

[28] Guerin, W., Araújo, M. O., and Kaiser, R. *Phys. Rev. Lett.* **116**, 083601 (2016).

[29] Bienaimé, T., Piovella, N., and Kaiser, R. *Phys. Rev. Lett.* **108**, 123602 (2012).

[30] Scully, M. O., Fry, E. S., Ooi, C. H. R., and Wódkiewicz, K. *Phys. Rev. Lett.* **96**, 010501 (2006).

[31] Svidzinsky, A. A., Chang, J. T., and Scully, M. O. *Phys. Rev. Lett.* **100**, 160504 (2008).

[32] Svidzinsky, A. A. and Scully, M. O. *Opt. Commun.* **282**, 2894 (2009).

[33] Bienaimé, T., Petruzzo, M., Bigerni, D., Piovella, N., and Kaiser, R. *J. Mod. Opt.* **58**, 1942 (2011).

[34] Bienaimé, T., Bachelard, R., Piovella, N., and Kaiser, R. *Fortschritte der Phys.* **61**, 377 (2013).

[35] Araújo, M. O., Kresic, I., Kaiser, R., and Guerin, W. *Phys. Rev. Lett.* **116**, 073002 (2016).

[36] Roof, S. J., Kemp, K. J., Havey, M. D., and Sokolov, I. M. *Phys. Rev. Lett.* **117**, 073003 (2016).

[37] de Oliveira, R. A., Mendes, M. S., Martins, W. S., Saldanha, P. L., Tabosa, J. W. R., and Felinto, D. *Phys. Rev. A* **90**, 023848 (2014).

[38] Bromley, S. L., Zhu, B., Bishof, M., Zhang, X., Bothwell, T., Schachenmayer, J., and Nicholson, T. L. *Nat. Commun.* **7**, 11039 (2016).

[39] Kitching, J., Knappe, S., and Donley, E. a. *IEEE Sens. J.* **11**, 1749 (2011).

[40] Nicholson, T. L., Campbell, S. L., Hutson, R. B., Marti, G. E., Bloom, B. J., McNally, R. L., Zhang, W., Barrett, M. D., Safronova, M. S., Strouse, G. F., Tew, W. L., and Ye, J. *Nat. Commun.* **6**, 6896 (2015).

[41] Bloom, B. J., Nicholson, T. L., Williams, J. R., Campbell, S. L., Bishof, M., Zhang, X., Zhang, W., Bromley, S. L., and Ye, J. *Nature* **506**, 71 (2014).

[42] Loudon, R. *The Quantum Theory of Light, 3rd Edition.* Oxford University Press, (2000).

[43] Scully, M. O. and Zubairy, M. S. *Quantum Optics.* Cambridge University Press, (1997).

[44] Woolley, R. G. *Proc. R. Soc. Lond.* **321**, 557 (1971).

[45] Power, E. A. and Zienau, S. *Philos. Trans. R. Soc. A Math. Phys. Eng. Sci.* **251**, 427 (1959).

[46] C. Cohen-Tannoudji, J. D.-R. and Grynberg, G. *Photons and Atoms.* Wiley, (1989).

[47] C. Cohen-Tannoudji, J. D.-R. and Grynberg, G. *Atom-Photon Interactions.* Wiley, (1992).

[48] Javanainen, J., Ruostekoski, J., Vestergaard, B., and Francis, M. R. *Phys. Rev. A* **59**, 649 (1999).

[49] Svidzinsky, A. A., Zhang, X., and Scully, M. O. *Phys. Rev. A - At. Mol. Opt. Phys.* **92**, 013801 (2015).

[50] Friedberg, R. and Manassah, J. T. *Phys. Lett. Sect. A Gen. At. Solid State Phys.* **372**, 2514 (2008).

[51] Scully, M. O. *Phys. Rev. Lett.* **102**, 143601 (2009).

[52] Scully, M. O. and Svidzinsky, A. A. *Science* **328**, 1239 (2010).

[53] Weisskopf, V. F. and Wigner, E. *Physik* **63**, 54–73 (1930).

[54] Blum, K. *Density Matrix Theory and Applications*. Plenum, (1981).

[55] Sutherland, R. T. and Robicheaux, F. *Phys. Rev. A* **93**, 023407 (2016).

[56] Ruostekoski, J. and Javanainen, J. *Phys. Rev. A* **55**, 513 (1997).

[57] Griffiths, D. J. *Introduction to Electrodynamics*. Prentice-Hall, (1999).

[58] Xiong, J., Colice, M., Schlottau, F., Wagner, K., and Fornberg, B. *Opt. Quantum Electron.* **40**, 447 (2008).

[59] Friedberg, R., Hartmann, S. R., and Manassah, J. T. *Phys. Rep.* **7**, 101 (1973).

[60] Courteille, P. W., Bux, S., Lucioni, E., Lauber, K., Bienaimé, T., Kaiser, R., and Piovella, N. *Eur. Phys. J. D* **58**, 69 (2010).

[61] Friedberg, R. and Manassah, J. T. *Phys. Rev. A - At. Mol. Opt. Phys.* **81**, 063822 (2010).

[62] Scully, M. O. and Svidzinsky, A. A. *Phys. Lett. Sect. A Gen. At. Solid State Phys.* **373**, 1283 (2009).

[63] Sete, E. A., Svidzinsky, A. A., Eleuch, H., Yang, Z., Nevels, R. D., and Scully, M. O. *J. Mod. Opt.* **57**, 1311 (2010).

[64] Raab, E. L., Prentiss, M., Cable, A., Chu, S., and Pritchard, D. E. *Phys. Rev. Lett.* **59**, 2631 (1987).

[65] Raizen, M. G., Budker, D., Rochester, S. M., Narevicius, J., and Narevicius, E. *Opt. Lett.* **39**, 4502 (2014).

[66] Boyd, R. *Nonlinear Optics.* Academic, (2003).

[67] Metcalf, H. M. and van der Straten, P. *Laser Cooling and Trapping.* Springer, (1999).

[68] Foot, C. J. *Atomic Physics.* Oxford University Press, (2005).

[69] Chu, S., Hollberg, L., Bjorkholm, J. E., Cable, A., and Ashkin, A. *Phys. Rev. Lett.* **55**, 48 (1985).

[70] Dalibard, J. and Cohen-Tannoudji, C. *J. Opt. Soc. Am. B* **6**, 2023 (1989).

[71] Lett, P. D., Watts, R. N., Westbrook, C. I., Phillips, W. D., Gould, P. L., and Metcalf, H. J. *Phys. Rev. Lett.* **61**, 169 (1988).

[72] Preston, D. W. *Am. J. Phys.* **64**, 1432 (1996).

[73] https://www.saesgetters.com/sites/default/files/AMD%20Brochure_0.pdf. Accessed: 2016-08-09.

[74] Chen, Y.-C., Liao, Y.-A., Hsu, L., and Yu, I. *Phys. Rev. A* **64**, 031401(R) (2001).

[75] Gibble, K. E., Kasapi, S., and Chu, S. *Opt. Lett.* **17**, 526 (1992).

[76] Steck, D. A. *available online http//steck.us/alkalidata (revision 2.1.4, 23 December 2010)* (2010).

[77] V. B. Berestetskii, E. M. L. and Pitaevskii, L. P. *Quantum Electrodynamics.* Elsevier, (1982).

[78] J. D. Miller, R. A. C. and Heinzen, D. J. *Physical Review A* **47**, R4567 (1993).

[79] Arnold, K. J. and Barrett, M. D. *Opt. Commun.* **284**, 3288 (2011).

[80] Grimm, R., Weidemüller, M., and Ovchinnikov, Y. *Adv. At. Mol. Opt. Phys.* **42**, 95 (2000).

[81] Schmieder, R. W. *Am. J. Phys.* **40**, 297 (1972).

[82] Safronova, M. S., Johnson, W. R., and Derevianko, A. *Phys. Rev. A* **60**, 4476 (1999).

[83] Safronova, M. S., Williams, C. J., and Clark, C. W. *Phys. Rev. A* **69**, 022509 (2004).

[84] Safronova, M. S., Arora, B., and Clark, C. W. *Phys. Rev. A - At. Mol. Opt. Phys.* **73**, 022505 (2006).

[85] Arora, B., Safronova, M. S., and Clark, C. W. *Phys. Rev. A - At. Mol. Opt. Phys.* **76**, 052509 (2007).

[86] Mitroy, J., Safronova, M. S., and Clark, C. W. *J. Phys. B* **43**, 202001 (2010).

[87] Chen, Y. J., Gonçalves, L. F., and Raithel, G. *Phys. Rev. A - At. Mol. Opt. Phys.* **92**, 060501(R) (2015).

[88] Verdeyen, J. *Laser Electronics*. Prentice Hall, (1995).

[89] Ludlow, A. D., Boyd, M. M., Ye, J., Peik, E., and Schmidt, P. O. *Rev. Mod. Phys.* **87**, 637 (2015).

[90] H. Katori, T. I. and Kuwata-Gonokami, M. *Journal of the Physical Society of Japan* **68**, 2479 (1999).

[91] McKeever, J., Buck, J. R., Boozer, a. D., Kuzmich, A., Nägerl, H. C., Stamper-Kurn, D. M., and Kimble, H. J. *Phys. Rev. Lett.* **90**, 133602 (2003).

[92] Griffin, P. F., Weatherill, K. J., MacLeod, S. G., Potvliege, R. M., and Adams, C. S. *New J. Phys.* **8**, 11 (2006).

[93] Kuppens, S. J. M., Corwin, K. L., Miller, K. W., Chupp, T. E., and Wieman, C. E. *Phys. Rev. A* **62**, 013406 (2000).

[94] Balik, S., Win, A. L., Havey, M. D., Sokolov, I. M., and Kupriyanov, D. V. *Phys. Rev. A* **87**, 053817 (2013).

[95] Olson, A. J., Niffenegger, R. J., and Chen, Y. P. *Phys. Rev. A - At. Mol. Opt. Phys.* **87**, 053613 (2013).

[96] Ketterle, W. and Druten, N. J. V. *Advances in Atomic, Molecular, and Optical Physics* **37**, 181–236 (1996).

[97] Anderson, M. H., Ensher, J. R., Matthews, M. R., Wieman, C. E., and Cornell, E. A. *Science* **269**, 198 (1995).

[98] Bittanti, S. and Colaneri, P. *Periodic Systems*. Springer, (2009).

[99] Pain, H. J. *The Physics of Vibrations and Waves, 6th Edition.* Wiley, (2005).

[100] Sheik-Bahae, M. *Quantum Electron. IEEE* **26**, 760 (1990).

[101] Stryland, E. W. V. and Sheik-Bahae, M. *Charact. Tech. Tabul. Org. Nonlinear Mater.* , 655 (1998).

[102] Wang, Y. and Saffman, M. *Opt. Commun.* **241**, 513 (2004).

[103] Labeyrie, G. and Bortolozzo, U. *Opt. Lett.* **36**, 2158 (2011).

[104] Kemp, K., Roof, S. J., Havey, M. D., Sokolov, I. M., and Kupriyanov, D. V. *arXiv:1410.2497 [physics.atom-ph]* (2014).

[105] Wang, Y. *Nonlinear self-focusing in cold cesium.* PhD thesis, Wisconsin, (2005).

[106] Newell, A. C. and Moloney, J. V. *Nonlinear Optics.* Addison-Wesley, (1992).

[107] J. H. McCellan, R. W. S. and Yoder, M. A. *DSP First A Multimedia Approach.* Pearson, (1997).

[108] Labeyrie, G., Ackemann, T., Klappauf, B., Pesch, M., Lippi, G., and Kaiser, R. **483**, 473 (2003).

[109] O'Connor, D. V. and Phillips, D. *Time-correlated Single Photon Counting.* Academic Press, (1984).

[110] http://www.photonics.ixblue.com/files/files/pdf/LiNb03_BiasControl_%26_Driving. pdf. Accessed: 2015-07-24.

[111] Simsarian, J., Orozco, L. A., Sprouse, G., and Zhao, W. *Phys. Rev. A* **57**, 2448 (1998).

[112] Padmabandu, G. G., Oh, C., and Fry, E. S. **17**(3), 169 (1992).

[113] Bienaimé, T., Bux, S., Lucioni, E., Courteille, P. W., Piovella, N., and Kaiser, R. *Phys. Rev. Lett.* **104**, 183602 (2010).

[114] Jennewein, S., Besbes, M., Schilder, N. J., Jenkins, S. D., Sauvan, C., Ruostekoski, J., Greffet, J. J., Sortais, Y. R. P., and Browaeys, A. *Phys. Rev. Lett.* **116**, 233601 (2016).

[115] Balik, S. *Light Scattering in an Ultracold High-denisty Atomic Sample.* PhD thesis, Old Dominion, (2008).

[116] Scholten, R. E. *Rev. Sci. Instrum.* **78**, 3077 (2007).

[117] Svidzinsky, A. A., Chang, J. T., Lipkin, H., and Scully, M. O. *J. Mod. Opt.* **55**, 3369 (2008).

[118] Toyoda, K., Takahashi, Y., Ishikawa, K., and Yabuzaki, T. *Phys. Rev. A* **56**, 1564 (1997).

[119] Chen, J. F., Wang, S., Wei, D., Loy, M. M. T., Wong, G. K. L., and Du, S. *Phys. Rev. A - At. Mol. Opt. Phys.* **81**, 033844 (2010).

[120] Chalony, M., Pierrat, R., Delande, D., and Wilkowski, D. *Phys. Rev. A - At. Mol. Opt. Phys.* **84**, 011401(R) (2011).

[121] Kwong, C. C., Yang, T., Pramod, M. S., Pandey, K., Delande, D., Pierrat, R., and Wilkowski, D. *Phys. Rev. Lett.* **113**, 223601 (2014).

[122] Kwong, C. C., Yang, T., Delande, D., Pierrat, R., and Wilkowski, D. *Phys. Rev. Lett.* **115**, 223601 (2015).

[123] Guerin, W., Rouabah, M. T., and Kaiser, R. *arXiv:1605.02439[physics.atom-ph]* (2016).

[124] Allen, L. and Eberly, J. H. *Optical Resonance and Two-level Atoms.* Dover, (1987).

[125] Roof, S. J., Kemp, K., Havey, M. D., Sokolov, I. M., and Kupriyanov, D. V. *Opt. Lett.* **40**, 1137 (2015).

[126] Zhu, B., Cooper, J., Ye, J., and Rey, A. M. *Phys. Rev. A* **94**, 023612 (2016).

[127] Walker, T. G., Bali, S., Hoffmann, D., and Sima, J. *Phys. Rev. A* **53**, 3469 (1996).

[128] Müller, C. A. and Delande, D. *Ultracold Gases Quantum Inf. Lect. Notes Les Houches Summer Sch. Singapore Vol. 91, July 2009* (2011).

[129] Scheffold, F. and Wiersma, D. *Nat. Photonics* **7**, 934 (2013).

[130] Mazets, I. E. and Kurizki, G. *J. Phys. B At. Mol. Opt. Phys.* **40**, F105 (2007).

APPENDIX A

DERIVATION OF THE SHAPE FACTOR FOR THE

COOPERATIVE DECAY

The equation for the cooperative decay rate (62) can be expressed as,

$$\Gamma_N = \frac{\Gamma}{N} \left[\sum_{j,m} \frac{\sin(k_a r_{jm})}{k_a r_{jm}} e^{-i\mathbf{k}_0 \cdot \mathbf{r}_{jm}} \delta_{jm} + \sum_{j,m \neq j} \frac{\sin(k_a r_{jm})}{k_a r_{jm}} e^{-i\mathbf{k}_0 \cdot \mathbf{r}_{jm}} \right]. \tag{131}$$

The first term sums exactly to the total number of atoms N and the second term can be taken to the continuous limit,

$$N(N-1) \int d\mathbf{r} \int d\mathbf{r}' \frac{\sin(k_a |\mathbf{r} - \mathbf{r}'|)}{k_a |\mathbf{r} - \mathbf{r}'|} e^{-i\mathbf{k}_0 \cdot (\mathbf{r} - \mathbf{r}')} \rho(\mathbf{r}) \rho(\mathbf{r}') \tag{132}$$

where

$$\rho(\mathbf{r}) = \frac{1}{(2\pi)^{3/2} r_0^2 z_0^2} e^{-(x^2 + y^2)/2r_0^2} e^{-z^2/2z_0^2} \tag{133}$$

is the normalized density distribution of the sample. Making the change of variables $\mathbf{s} = \mathbf{r} - \mathbf{r}'$ and $\boldsymbol{\tau} = \mathbf{r} + \mathbf{r}'$, the spatially dependent integral becomes,

$$\frac{1}{8} \int d\mathbf{s} \int d\boldsymbol{\tau} \frac{\sin(k_a s)}{k_a s} e^{-i\mathbf{k}_0 \cdot \mathbf{s}} e^{-(s_x^2 + \tau_x^2)/4r_0^2} e^{-(s_y^2 + \tau_y^2)/4r_0^2} e^{-(s_z^2 + \tau_z^2)/4z_0^2} \tag{134}$$

where the 1/8 comes from the evaluation of the Jacobian from the coordinate transformation. The integrals over $\boldsymbol{\tau}$ can be carried out so that (134) becomes,

$$\pi^{3/2} r_0^2 z_0^2 \int d\mathbf{s} \frac{\sin(k_a s)}{k_a s} e^{-i\mathbf{k}_0 \cdot \mathbf{s}} e^{-(s_x^2 + s_y^2)/4r_0^2} e^{-s_z^2/4z_0^2}. \tag{135}$$

We can write the $\frac{\sin(k_a s)}{k_a s}$ term as

$$\frac{\sin(k_a s)}{k_a s} = \frac{1}{4\pi} \int_0^{2\pi} d\phi \int_{-1}^1 d(\cos\theta) e^{i\mathbf{k}_a \cdot \mathbf{s}} \tag{136}$$

taking $\mathbf{k}_a = k_a \hat{\mathbf{n}}$, where $\hat{\mathbf{n}}$ is a unit vector pointing radially outwards [130, 61]. The spatial integrals I_s can now be carried out,

$$\begin{aligned} I_s &= \int_{-\infty}^\infty ds_x e^{-s_x^2/4r_0^2 + iq_x s_x} \int_{-\infty}^\infty ds_y e^{-s_y^2/4r_0^2 + iq_y s_y} \int_{-\infty}^\infty ds_z e^{-s_z^2/4z_0^2 + iq_z s_z} \\ &= 8\pi^{3/2} r_0^2 z_0 e^{-(q_x^2 + q_y^2)r_0^2} e^{-q_z^2 z_0^2}, \end{aligned} \tag{137}$$

where $q_x = k_a \sin\theta \cos\phi$, $q_y = k_a \sin\theta \sin\phi$, and $q_z = k_a \cos\theta - k_0$. Γ_N is now,

$$\Gamma_N = \Gamma + \frac{(N-1)\Gamma}{2} \int_{-1}^{1} d\xi e^{-r_0^2 k_a^2 (1-\xi^2)} e^{-z_0^2 (k_a \xi - k_0)^2}, \tag{138}$$

where the ϕ integral has been evaluated and $\xi = \cos\theta$ for shorthand. Introducing the parameters $\sigma = r_0 k_0$ and $\eta = z_0/r_0$, and making the approximation that $k_0/k_a \simeq 1$, the integral over ξ is

$$I_\xi = \exp\left[\frac{\sigma^2}{\eta^2 - 1}\right] \int_{-1}^{1} d\xi \exp\left[-\sigma^2(\eta^2 - 1)\left(\xi - \frac{\eta^2}{\eta^2 - 1}\right)^2\right]. \tag{139}$$

Changing variables to $u = \sigma\sqrt{\eta^2 - 1}\xi - \sigma\eta^2/\sqrt{\eta^2 - 1}$, (139) becomes

$$I_\xi = \frac{\exp\left[\frac{\sigma^2}{\eta^2 - 1}\right]}{\sigma\sqrt{\eta^2 - 1}} \int_{-\frac{\sigma(2\eta^2 - 1)}{\sqrt{\eta^2 - 1}}}^{\frac{-\sigma}{\sqrt{\eta^2 - 1}}} du e^{-u^2}. \tag{140}$$

Using the definition of the error function,

$$\text{erf}(x) = \frac{2}{\sqrt{\pi}} \int_0^x dt e^{-t^2}, \tag{141}$$

(139) reduces to,

$$I_\xi = \frac{\sqrt{\pi}}{2\sigma\sqrt{\eta^2 - 1}} \exp\left[\frac{\sigma^2}{\eta^2 - 1}\right] \left\{\text{erf}\left[\frac{\sigma}{\sqrt{\eta^2 - 1}}(2\eta^2 - 1)\right] - \text{erf}\left[\frac{\sigma}{\sqrt{\eta^2 - 1}}\right]\right\}. \tag{142}$$

Substituting (139) into (138) gives the final expression,

$$\Gamma_N = \Gamma + \alpha(N-1)\Gamma,$$
$$\alpha = \frac{\sqrt{\pi}}{4\sigma\sqrt{\eta^2 - 1}} \exp\left[\frac{\sigma^2}{\eta^2 - 1}\right] \left\{\text{erf}\left[\frac{\sigma}{\sqrt{\eta^2 - 1}}(2\eta^2 - 1)\right] - \text{erf}\left[\frac{\sigma}{\sqrt{\eta^2 - 1}}\right]\right\}. \tag{143}$$
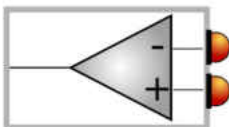
Fermi's Golden Rule can also give this result if the timed-Dicke state (58) is made the initial state, coupling to subradiant modes are neglected [117], and the sum over final states is over all possible emission directions $\mathbf{k}$.

APPENDIX B

NOMENCLATURE FOR OPTICAL ELEMENTS AND OTHER DEVICES

The optical elements are based on schematic drawings by Alexander Franzen (http://www. gwoptics.org/ComponentLibrary/) and have been partially modified for use in this thesis.

	780 nm laser		acousto-optic modulator
	780 nm laser beam		non-polarizing beam splitter
	Faraday isolator		differential photodetector
	$\lambda/2$ waveplate		fiber launching mount and lens
	polarizing beam splitter		polarization preserving fiber
	positive focal length lens		single-mode fiber
	mirror		Rubidium vapor cell
	atom fluorescence		shutter
	negative focal length lens		photodetector

LiNbO$_3$ switch

linear polarizer

1064 nm laser

1064 nm laser beam

attenuator

$\lambda/4$ waveplate

interference filter
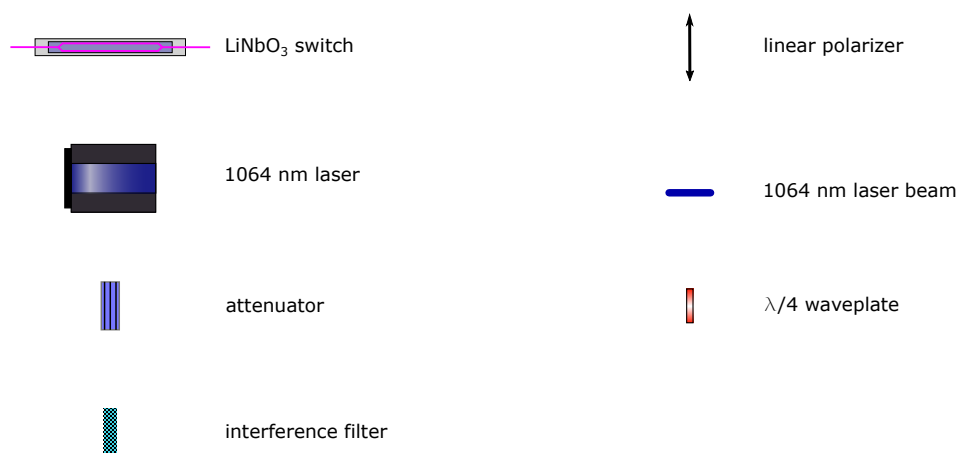
APPENDIX C

ARDUINO CODE FOR DC BIAS LOCKING CIRCUIT

```
int outputPlus=6;
int outputMinus=5;
int setValue=100; //has to be given some value intially
float ieta=.05;
int level=0;
int starter=0;
int inputPin=8;
int TTL=9;
void setup() {
        Serial.begin(9600);
        pinMode(outputPlus,OUTPUT);
        pinMode(outputMinus,OUTPUT);
        pinMode(inputPin,INPUT);
        pinMode(TTL,INPUT);
        digitalWrite(outputPlus,LOW);
        digitalWrite(outputMinus,LOW);
}
void loop() {
        if(digitalRead(inputPin)==1 && digitalRead(TTL)==0){
                int previousValue;
                while(error(currentValue(A0))>ieta){
                        previousValue=currentValue(A0);
                        //Add positive voltage//
                        if(starter==0){
                                positiveAdd();
                                if(error(currentValue(A0))>error(previousValue)){
                                        level=level-1;
                                        starter=1;
                                }
                        }
                        //Subtract positive voltage//
                        if(starter==1){
                                if(level==0){
                                        digitalWrite(outputPlus,LOW);
                                        starter=2;
                                }
                                else{
                                        positiveSubtract();
                                        if(error(currentValue(A0))>error(previousValue)){
                                                level=level+1;
                                                starter=0;
                                        }
                                }
                        }
                        //Add negative voltage//
                        if(starter==2){
                                negativeAdd();
                                if(error(currentValue(A0))>error(previousValue)){
                                        level=level-1;
                                        starter=3;
                                }
                        }
                        //Subtract negative voltage//
                        if(starter==3){
                                if(level==0){
                                        digitalWrite(outputMinus,LOW);
                                        starter=0;
                                }
                                else{
```

```
                                    negativeSubtract();

                                    if(error(currentValue(A0))>error(previousValue)){
                                            level=level+1;
                                            starter=2;
                                    }
                            }
                    }
                    //Check and see if switch was opened
                    if(digitalRead(inputPin)==0){
                            break;
                    }
                }
        }
        else if(digitalRead(inputPin)==1 && digitalRead(TTL)==1){
                level=level;
                starter=starter;
        }
        else if(digitalRead(inputPin)==0){
                digitalWrite(outputPlus,LOW);
                digitalWrite(outputMinus,LOW);
                level=0;
                starter=0;
                Serial.println("The_switch_is_not_closed");
                setValue=currentValue(A0);
                Serial.println(setValue);
        }
        else{
                level=level;
                starter=starter;
        }
}
int currentValue(int x){
        int i;
        int val=0;
        int valMean;
        for(i=0;i<10;i++){
                val=val+analogRead(x);
        }
        valMean=val/10;
        return valMean;
}
float error(int x){

        float er;
        er=(float)abs(setValue-x)/setValue;
        return er;
}
void positiveAdd(){
        level=level+1;
        analogWrite(outputPlus,level);
        delay(200);
}
void positiveSubtract(){
        level=level-1;
        analogWrite(outputPlus,level);
        delay(200);
}
void negativeAdd(){
        level=level+1;
        analogWrite(outputMinus,level);
        delay(200);
}
void negativeSubtract(){
        level=level-1;
        analogWrite(outputMinus,level);
        delay(200);
}
```

APPENDIX D

NUMERICAL SOLUTION TO THE TIME DEPENDENT

MAXWELL-BLOCH EQUATIONS

Here we will present the techniques used to solve the Maxwell-Bloch equations in the time domain. Making the change of variables $z' = z$ and $t' = t - z/c$, the MBEs (129) and (130) can be written as

$$
\frac{\partial}{\partial t'} \begin{pmatrix} W \\ U \\ V \end{pmatrix} = \begin{pmatrix} -\Gamma & -\mathrm{Im}\,(\Omega) & -\mathrm{Re}\,(\Omega) \\ \mathrm{Im}\,(\Omega) & -\Gamma/2 & \Delta \\ \mathrm{Re}\,(\Omega) & -\Delta & -\Gamma/2 \end{pmatrix} \begin{pmatrix} W \\ U \\ V \end{pmatrix} + \begin{pmatrix} -\Gamma \\ 0 \\ 0 \end{pmatrix} \tag{144}
$$

$$
\frac{\partial \Omega}{\partial z'} = \frac{i\kappa\Gamma}{2} \left(U - iV \right). \tag{145}
$$

The absorption coefficient κ for a simple two-level atom as considered here is

$$
\kappa = \frac{2d_{eg}^2 k_a}{\hbar\epsilon_0\Gamma} \tag{146}
$$

(see section 4.2). The numerical solution follows [58, 118] by the slicing the one dimensional sample into very thin slabs with thickness δz and solving for the time evolution of the Bloch variables in the mth slab at $t' = (n+1)\delta t$ using the electric field and Bloch variables at $t' = n\delta t$ in the mth slab. The electric field in the $(m+1)^{th}$ slab at $t' = (n+1)\delta t$ can be solved using the electric field and Bloch variables at $t' = (n+1)\delta t$ from the mth slab. A schematic of the algorithm is shown in Fig. 68. To estimate the derivative in (144) we use 4th-order Runge-Kutta just like in section 2.4 where now

$$
A \equiv \begin{pmatrix} -\Gamma & -\mathrm{Im}\,(\Omega) & -\mathrm{Re}\,(\Omega) \\ \mathrm{Im}\,(\Omega) & -\Gamma/2 & \Delta \\ \mathrm{Re}\,(\Omega) & -\Delta & -\Gamma/2 \end{pmatrix} \tag{147}
$$

and

$$
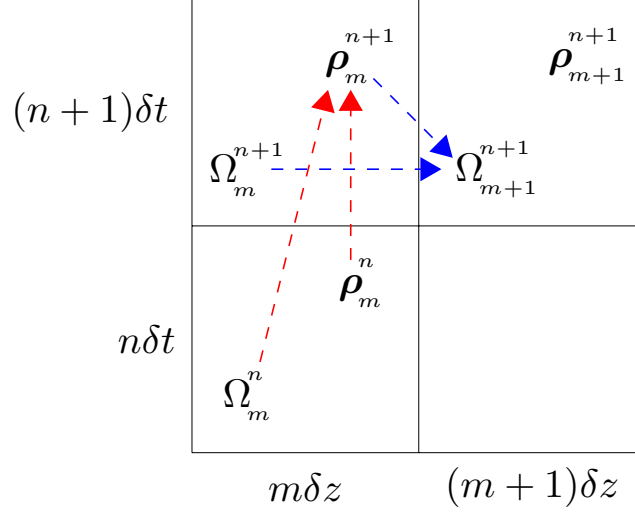b \equiv \begin{pmatrix} -\Gamma \\ 0 \\ 0 \end{pmatrix} \tag{148}
$$

FIG. 68: Schematic of the algorithm used to solve the MBEs. The arrows indicate which variables are used to solve for the next step of variables in either space or time. The symbol $\boldsymbol{\rho}$ is used to indicate the Bloch variables.

The derivative in (145) can be estimated with the simple trapezoidal rule,

$$\Omega_{m+1}^n = \Omega_m^n + \frac{\delta z}{2} \frac{i\kappa\Gamma}{2} \left(U_m^n - iV_m^n\right) \tag{149}$$

The process is started by setting (W, U, V) for $t = 0$ and $\forall z$ equal to $(-1, 0, 0)$; meaning the atoms start in their ground state. For the electric field, $\Omega(0, t)$ is the programmed input pulse which is usually taken as a square pulse. The variables are propagated along the z axis for each value of t' until the two-dimensional grid has been completely filled. The transmitted field is taken as the value of the electric at the position $z = L$ and the scattered field can be calculated by noting that $E_t = E_0 + E_s$. Stability for the step sizes δz and δt is checked by ensuring the inner product $\boldsymbol{\rho} \cdot \boldsymbol{\rho}$ is conserved throughout the process and that the solution converges for decreasing values of the step size. Typical step sizes are chosen as $\frac{1}{1000}L - \frac{1}{100}L$ and $\frac{1}{1000}\Gamma^{-1} - \frac{1}{100}\Gamma^{-1}$ for δz and δt, respectively.

An additional method is possible by solving the optical bloch equations in the frequency domain [119]. To do so, we resort back to the former notation for $\tilde{\rho}_{eg}$ and use the definition

$$f(t) = \frac{1}{2\pi} \int_{-\infty}^{\infty} d\omega f(\omega) e^{-i\omega t} \tag{150}$$

for the Fourier transform. The frequency domain equivalent of (70) in the low light excitation

limit is then

$$\tilde{\rho}_{eg}(\omega) = -\frac{1}{2}\frac{\Omega(\omega)}{\omega + \Delta + i\Gamma/2} \tag{151}$$

Substituting (151) into (145) gives,

$$\frac{\partial \Omega}{\partial z} = \frac{ik_0}{2}\chi(\omega)\Omega(\omega) \tag{152}$$

where

$$\chi(\omega) = -\frac{\kappa}{k_0}\frac{\Gamma/2}{\omega + \Delta + i\Gamma/2} \tag{153}$$

is the frequency dependent complex susceptibility [119]. Integrating (152) over the length of the sample gives

$$\Omega(L) = \Omega(0)e^{i\frac{k_0}{2}\chi(\omega)L}, \tag{154}$$

which is the transmitted field Ω_T and $\Omega(0)$ is the incident field Ω_0. Since the transmitted field must be a superposition of the incident field and the scattered field, Ω_s, from the sample [122], Ω_s can be written as

$$\Omega_s(\omega) = \Omega_0(\omega)\left[e^{i\frac{k_0}{2}\chi(\omega)L} - 1\right]. \tag{155}$$

Transforming back to the time domain gives the temporal response of the scattered field from the sample. In this formalism, the sample is essentially a linear response filter and the resultant fast decays are a by-product of the transient response of the susceptibility.

VITA

Stetson Roof

Department of Physics

Old Dominion University

Norfolk, VA 23529

EDUCATION

Ph. D. Physics, *Forward light scattering in an extended cold atomic sample*, Old Dominion University, Norfolk, VA, August 2016. **Advisor**: Mark D. Havey

M.S. Physics, Old Dominion University, Norfolk, VA, 2012.

B.S. Engineering Physics, Murray State University, Murray, KY, 2010.

PUBLICATIONS

Observation of single-photon superradiance and the cooperative Lamb shift in an extended sample of cold atoms, S. J. Roof, Kasie Kemp, M.D. Havey, and I.M. Sokolov, Phys. Rev. Lett. **117**, 073003 (2016).

Emergent Collectivity in Light Scattering from Cold Atoms, Kasie Kemp, S.J. Roof, M.D. Havey, I.M. Sokolov, D.V. Kupriyanov, In preparation.

Microscopic lensing by a dense, cold atomic sample, Stetson Roof, Kasie Kemp, Mark D. Havey, I. M. Sokolov, D. V. Kupriyanov, Opt. Lett. **40**, 1137 (2015).

Optical Manipulation of Light Scattering in Cold Atomic Rubidium, Olave, R. G., Win, A. L., Kemp, K., Roof, S. J., Balik, S., Havey, M. D., Sokolov, I. M., and Kupriyanov, D. V, "From Atomic to Mesoscale: The Role of Quantum Coherence in Systems of Various Complexities," Edited by Malinovskaya Svetlana et al, World Scientific Publishing Co, pp.39-59, 2015.

Typeset using LaTeX.